Universität Bonn

Physikalisches Institut

Measurement of the top quark pair production cross section with the ATLAS detector at LHC in pp collisions at $\sqrt{s} = 7$ TeV in dilepton final states

Tatevik Abajyan

The production cross section of top quark pairs in proton-proton collisions at center-of-mass energy of 7 TeV recorded with the ATLAS detector at the CERN Large Hadron Collider is measured. The goal of the analysis is to provide a benchmark test of perturbative QCD and the Standard Model by measuring the $t\bar{t}$ production cross section in data and compare the measurement with theoretical predictions. Within the Standard Model, a top quark almost exclusively decays to a W-boson and a b-quark. Using a data sample of 35 pb^{-1}, candidate events are selected in the dilepton topology (where both W-bosons from $t\bar{t}$ decay leptonically) with large missing transverse energy and at least two jets. The branching ratio of this process is 6.5%. The theoretical expectation for $t\bar{t}$ production cross section in proton-proton collisions at center-of-mass energy of 7 TeV is 165^{+11}_{-16} pb. Backgrounds from $Z/\gamma^* \to \ell\ell$ and mis-identified leptons are estimated from data. Results include detailed studies of systematic uncertainties. A $t\bar{t}$ production cross section $181 \pm 22(\text{stat.}) \pm 14(\text{syst.}) \,^{+8}_{-7}(\text{lumi.})$ pb is measured for an assumed top quark mass of 172.5 GeV.

Physikalisches Institut der
Universität Bonn
Nußallee 12
D-53115 Bonn

BONN-IR-2012-02
März 2012
ISSN-0172-8741

Universität Bonn

Physikalisches Institut

Measurement of the top quark pair production cross section with the ATLAS detector at LHC in pp collisions at $\sqrt{s} = 7$ TeV in dilepton final states

Tatevik Abajyan

Dieser Forschungsbericht wurde als Dissertation von der Mathematisch-Naturwissenschaftlichen Fakultät der Universität Bonn angenommen und ist auf der ULB Bonn `http://hss.ulb.uni-bonn.de/diss_online` elektronisch publiziert.

1. Gutachter:	Dr. Markus Cristinziani
2. Gutachter:	Prof. Norbert Wermes
Angenommen am:	13.02.2012
Tag der Promotion:	23.03.2012

Acknowledgements

With the deepest gratitude I wish to thank my supervisor Dr. Markus Cristinziani for his consistent support and patience throughout the past three years. He inspired me both as a scholar and a person and provided an opportunity for me to engage in a scientific research that I believed in.

I would like to acknowledge and express my gratitude to Prof. Norbert Wermes for his support and for agreeing to be the second reviewer of my thesis as well as the other committee members Prof. Herbert Dreiner and Prof. Klaus Greve for their time and input.

A heartfelt gratitude goes to my colleagues from our group and from the "ATLAS top working group" for help, discussions and friendliness, especially Kirika Uchida, Duc Bao Ta, Yasuyuki Okumura, Gia Khoriauli, Gizo Nanava, Agnieszka Leyko, Sara Ghasemi, Ralph Schäfer and Kaven Yau.

I deeply appreciate the help of the people who have supported me with recommendation letters and advises when I was applying for the PhD position. This include Prof. Hans Specht, Dr. Ruben Shahoyan and Dr. Hrant Gulkanyan.

I would like to thank my parents, who did everything possible to have educated children. Sorry for the long distance between us and lonely days without me. I hope I live up to your expectations. Also thanks to my grandparents and all relatives, especially to my brother. His high motivation and successes in physics had a strong impression on me.

And deep thanks to my dear husband. Most importantly, I would not have met him without the chance to relocate to Germany and enroll in this PhD program. Thank you for your understanding and support when it was difficult for me and when I needed you so much.

Contents

1 Introduction **1**

2 Theory **3**
2.1 Standard model of particle physics . . . 3
2.2 Top quark physics . . . 7

3 The LHC and the ATLAS experiment **21**
3.1 Large Hadron Collider . . . 21
3.2 The ATLAS detector . . . 22
3.3 Trigger and data acquisition . . . 28

4 Data and Monte-Carlo simulation **31**
4.1 Luminosity . . . 31
4.2 2010 ATLAS data . . . 32
4.3 Monte-Carlo simulation . . . 33

5 Reconstruction, identification and selection of objects **39**
5.1 Electrons . . . 39
5.2 Muons . . . 45
5.3 Jets . . . 51
5.4 Missing transverse energy . . . 55

6 Cut optimisation and event selection **57**
6.1 Cut optimisation . . . 57
6.2 Event selection . . . 60

7 Background determination **69**
7.1 Data-driven backgrounds . . . 69
7.2 Other MC simulated background . . . 78

8 Cut and count analysis **81**
8.1 Counting method . . . 81
8.2 Control regions . . . 81
8.3 Signal region and event yields . . . 82

9 Systematic uncertainties **91**
9.1 Luminosity . . . 92

9.2 Systematics on data-driven backgrounds . . . 94
9.3 Theoretical cross section . . . 94
9.4 Jets . . . 94
9.5 Missing transverse energy . . . 95
9.6 Leptons . . . 95
9.7 $t\bar{t}$ production modelling . . . 96

10 Results **105**

11 Cross-checks with other analyses **111**

12 Conclusion **115**

A Useful information **117**

Bibliography **119**

List of Figures **133**

List of Tables **137**

Chapter 1

Introduction

Particle physics aims at describing the structure of matter.
It explains many things, but not everything so far, and I like it because it is beautiful.

The widely accepted modern view of the origin and history of the Universe is based on the Big Bang hypothesis. According to this hypothesis, our Universe was born about 13.7 ± 0.1 billion years ago.

From 300,000 to 400,000 years after the Big Bang, the Universe was finally cold enough such that stable atoms could form. To get information of what existed before we have to find traces of the expansion in time back to the very beginning. With this, we want to explain the innermost structure of matter by discovering what the fundamental constituents of matter are, and which forces interact amongst them. To answer these questions, we build high energy accelerators, a kind of super-microscope, since high energy investigates small structures.

The achievement that human beings managed to reach so far is to go down to $10^{-18} - 10^{-19}$m and find out that the matter particles are leptons and quarks. There are six leptons and six quarks, and we needed more than 100 years (since the discovery of the electron in 1897) to build this picture, one-by-one experimentally observing them. The theory that describes interactions between elementary particles is called the Standard Model. There is one important piece missing within this model which is the so-called Higgs boson. It is not experimentally observed yet, but it is a very important part of this model, since its existence would give answers to the question of what is the origin of mass of the elementary particles.

Within the Standard Model the leptons and quarks are grouped into three generations and the interactions between them are mediated by gauge bosons. The Standard Model in more details will be discussed in the next chapter. This thesis is about one of the six quarks, so-called top quark. The top quark is the heaviest elementary particle. It is as massive as a gold atom, nonetheless it is an elementary particle with the size of less than 10^{-18} m . It was found in 1995 at the Tevatron proton-antiproton collider at a center-of-mass energy ($\sqrt{s}$) of $\sim$2 TeV. The top quark production cross section measurement, which is the subject of the work presented in this dissertation, provides a benchmark test of perturbative QCD and the Standard Model, and plays an important role in the searches for new physics. Moreover, top quark pair production is an important background in searches for the Higgs boson and physics beyond the Standard Model.

The top pair ($t\bar{t}$) production cross section ($\sigma_{t\bar{t}}$) requires a good understanding of the reconstruction and identification efficiencies, as well as a careful evaluation of the background processes that mimic the signal. It can be measured either using an event counting method or by fitting a discriminant variable that separates signal and background. In this work, the cross section is evaluated by a counting method, determined from the observed number of top candidates, estimated background, $t\bar{t}$ acceptance, and integrated luminosity. The theoretical expectation for $t\bar{t}$ production cross section in pp collisions at $\sqrt{s} = 7$ TeV is 165^{+11}_{-16}pb for a top quark mass of 172.5 GeV.

The analysis is performed using data samples with an integrated luminosity of 35 pb^{-1} collected at pp collisions recorded by the ATLAS detector at $\sqrt{s} = 7$ TeV in 2010. The result is documented in a publication submitted to Phys. Lett. B [1].

The thesis is organised as follows. Chapter 2 gives a brief introduction to the Standard Model of particle physics and the physics of top quarks. Chapter 3 describes the LHC accelerator and the ATLAS experiment. In Chapter 4 some details about data and Monte-Carlo samples used for this analysis are presented. Chapter 5 describes reconstruction, identification and selection of objects. Cut optimisation, event selection criteria and background determination are presented in Chapter 6 and Chapter 7, respectively. The counting method with observed and expected yields are discussed in Chapter 8. Chapter 9 describes relevant systematic uncertainties from different sources that are assigned to the measurement. The final results are presented in Chapter 10 where the cross section measurements in different sub-channels are combined with a likelihood method. The results are compared with other analyses in Chapter 11 and discussed in Chapter 12.

Bonn, January 2012

Chapter 2

Theory

2.1 Standard model of particle physics

The Standard Model (SM) [2, 3] provides a theoretical framework which describes phenomena of elementary particles and their fundamental interactions. Elementary particles are the point-like constituents of matter with no known substructure down to the present limits of $10^{-18}-10^{-19}$m. These are of two types, the basic building blocks of matter themselves known as matter constituents, called "fermions", and the intermediate interaction particles, called "bosons".

The first ones are particles with spin $\frac{1}{2}$ and classified in leptons and quarks. In the SM there are twelve elementary fermions, six quarks and six leptons, each arranged into three generations. The three generations have identical properties except for mass. The quarks, up (u), charm (c), and top (t), have electric charge $+\frac{2}{3}$ while the other three quarks, down (d), strange (s), and bottom (b), have electric charge $-\frac{1}{3}$. The neutrinos, ν_e, ν_μ, and ν_τ are the electric-charge-neutral leptons and partners to the electron (e), muon (μ), and tau (τ) "flavor" leptons, respectively. The e, μ, and τ all carry electric charge -1. Leptons and quarks have their anti-particles with the same mass and spin, but opposite signs of some characteristics of the interaction (charges, such as electric and color charge, baryon and lepton quantum numbers).

Bosons are particles with integer spin which mediate interaction between fermions. The diversity of Nature is governed and organized by four forces - carriers of the strong, electromagnetic, weak, and gravitational interactions. In the SM the first three fundamental interactions are described to be mediated by the gauge bosons with spin 1. There are 8 gluons (g) for the strong interactions, $W^{\pm}$- and Z-bosons for the weak interaction and the photon (γ) for the electromagnetic interaction. The strengths of these interactions are characterized by coupling constants with these approximate relative strengths $\alpha_s : \alpha_{em} : \alpha_{weak} \approx \frac{1}{10} : \frac{1}{100} : \frac{1}{10000}$. While the gluon and photon are massless, the W- and Z-bosons are massive and have been measured to be $m_W = 80.4$ GeV and $m_Z = 91.2$ GeV [4]. Gravitation is not successfully formulated in terms of a quantum field theory, therefore it is not part of SM yet. An overview of elementary particles as well as some of their properties is given in Table 2.1.

The six quarks possess an additional quantum number, called color (for antiquarks, anticolor). The color has three components, which are traditionally denoted by red, green, and blue. Each quark can be in any of these three color states. Quarks are interacting

Generation	Particle	Mass	Charge	Flavor	Strong	Weak	El.mag.
Leptons							
I	ν_e (1953)	< 2.2 eV	0	$L_e = 1$	-	✓	-
	e (1897)	0.511 MeV	-1				✓
II	ν_μ (1962)	< 0.17 eV	0	$L_\mu = 1$	-	✓	-
	μ (1936)	106 MeV	-1				✓
III	ν_τ (2000)	< 18.2 MeV	0	$L_\tau = 1$	-	✓	-
	τ (1975)	1777 MeV	-1				✓
Quarks							
I	u (1968)	1.7–3.1 MeV	$+\frac{2}{3}$	-	✓	✓	✓
	d (1968)	4.1–5.7 MeV	$-\frac{1}{3}$	-			
II	c (1974)	1.29 GeV	$+\frac{2}{3}$	C $= 1$	✓	✓	✓
	s (1968)	100 MeV	$-\frac{1}{3}$	S $= -1$			
III	t (1995)	173.2 GeV	$+\frac{2}{3}$	T $= 1$	✓	✓	✓
	b (1977)	4.2 GeV	$-\frac{1}{3}$	B $= -1$			
Bosons							
	g (1979)	0	0		✓	-	-
	$W^\pm$ (1983)	80.4 GeV	± 1		-	✓	-
	Z^0 (1983)	91.2 GeV	0		-	✓	-
	γ (1900)	$< 10^{-18}$ eV	0		-	-	✓

Table 2.1 Overview of elementary particles in the SM with some of their properties and corresponding interactions to which they participate. Leptons and quarks are arranged in three generations. Bosons are the interaction mediating particles for three fundamental forces (gravitation is not included). In parentheses the years of discoveries are given. For gluon the theoretical value is given (a mass as large as a few MeV may not be precluded) [4].

with each other by means of gluons which also carry color. The theory which describes the interaction of quarks and gluons is called Quantum Chromodynamics (QCD). Gluons have no mass and they do not carry electric charge, isospin or any flavor number. At first glance, the gluons seem to be very similar to photons, which carry the electromagnetic interaction between the electrically charged particles and one could think about similarity of QCD and Quantum Electrodynamics (QED), the quantum theory of the electromagnetic interactions. Indeed, at small distances between quarks their interaction can be described by the Coulomb–like potential, with a very small interaction constant, similarly to the interaction between the electrically charged particles in QED. This situation is called "ultraviolet", or "asymptotic freedom" of QCD. However, at large distances the behavior of the color interaction potential differs drastically from the electric one. The electric interaction potential continues to follow the $1/r$ law (where r is the distance

between the electric charges), while the color interaction potential changes its behavior and grows linearly with the distance between quarks and antiquarks. This peculiar behavior of the chromoelectric forces at large distances is due to the selfinteraction of gluons. This is the origin of the difference between QCD and QED since the photons do not interact with each other.

The linear increase of the chromoelectric interactions potential at large distances leads to the so-called confinement of quarks and gluons, which means that neither quarks nor gluons can exist as free states and they are necessarily confined to colorless hadrons. The hadrons can be divided in two groups – baryons and mesons. All baryons (for instance, neutron or proton) are fermions, i.e. they have half-unit value of spin. The mesons (pion, kaon, etc.) are bosons, i.e. particles with integer spin. In terms of QCD they are classified as follows: mesons are composed of one quark and one antiquark and baryons are constructed of three quarks.

From a theoretical point of view the SM is a quantum field theory based on the gauge symmetry

$$\mathrm{SU(3)_C} \times \mathrm{SU(2)_L} \times \mathrm{U(1)_Y}\,. \tag{2.1}$$

This gauge group includes the symmetry group of the strong interactions, $\mathrm{SU(3)_C}$, and the symmetry group of the electroweak interactions, $\mathrm{SU(2)_L} \times \mathrm{U(1)_Y}$. The group symmetry of the electromagnetic interactions, $\mathrm{U(1)_{em}}$, appears in the SM as a subgroup of $\mathrm{SU(2)_L} \times \mathrm{U(1)_Y}$ and it is in this sense that the weak and electromagnetic interactions are said to be unified [3]. $\mathrm{U(1)_Y}$ is the only Abelian (commutative) gauge group in the SM. The other two groups describe the interaction via non-Abelian gauge theory and the selfinteraction of gluons, W- and Z-bosons are genuine of a non-abelian theory.

$\mathrm{SU(3)_C}$ is generated by color transformations, where C refers to colors and 3 is the "dimension" of the group. $\mathrm{SU(2)_L}$ and $\mathrm{U(1)_Y}$ are weak isospin and hypercharge symmetries, respectively.

The $\mathrm{SU(2)_L}$ weak isospin group acts on left-handed fermions. The left-handed fermions transform as doublets under $\mathrm{SU(2)_L}$ whereas the right-handed fermions transform as singlets, since right-handed neutrinos do not couple to any of the fundamental forces. The left-handed and right-handed fields are defined by means of the chirality operator γ_5 as:

$$\psi_L = \frac{1-\gamma_5}{2}\psi, \quad \psi_R = \frac{1+\gamma_5}{2}\psi \tag{2.2}$$

Following from here, the particle content in each family can be given as:

$$
\begin{array}{lll}
 & \text{leptons} & \text{quarks} \\
1^{st}\text{family}: & \begin{pmatrix} \nu_e \\ e^- \end{pmatrix}_{\mathrm{L}}, e^-_{\mathrm{R}} & \begin{pmatrix} u \\ d' \end{pmatrix}_{\mathrm{L}}, u_{\mathrm{R}}, d_{\mathrm{R}} \\
2^{nd}\text{family}: & \begin{pmatrix} \nu_\mu \\ \mu^- \end{pmatrix}_{\mathrm{L}}, \mu^-_{\mathrm{R}} & \begin{pmatrix} c \\ s' \end{pmatrix}_{\mathrm{L}}, c_{\mathrm{R}}, s_{\mathrm{R}} \\
3^{rd}\text{family}: & \begin{pmatrix} \nu_\tau \\ \tau^- \end{pmatrix}_{\mathrm{L}}, \tau^-_{\mathrm{R}} & \begin{pmatrix} t \\ b' \end{pmatrix}_{\mathrm{L}}, t_{\mathrm{R}}, b_{\mathrm{R}}
\end{array}
$$

In the doublets, neutrinos and the up-type quarks (u, c, t) have the weak isospin $\mathrm{T}_3 = +\frac{1}{2}$, while the charged leptons and down-type quarks (d, s, b) carry the weak isospin $\mathrm{T}_3 = -\frac{1}{2}$. The weak hypercharge Y is then defined via electric charge and weak isospin to be $\mathrm{Y} = 2\mathrm{Q} - 2\mathrm{T}_3$. Consequently, members within a doublet carry the same hypercharge: $\mathrm{Y} = -1$ for leptons and $\mathrm{Y} = \frac{1}{3}$ for quarks.

The primes on the lower components of the quark doublets signal that the weak eigenstates are mixtures of the mass eigenstates:

$$
\begin{pmatrix} d' \\ s' \\ b' \end{pmatrix} = V_{\mathrm{CKM}} \begin{pmatrix} d \\ s \\ b \end{pmatrix} \tag{2.3}
$$

where

$$
V_{\mathrm{CKM}} = \begin{pmatrix} V_{ud} & V_{us} & V_{ub} \\ V_{cd} & V_{cs} & V_{cb} \\ V_{td} & V_{ts} & V_{tb} \end{pmatrix} = \begin{pmatrix} 0.97428 & 0.2253 & 0.00347 \\ 0.2252 & 0.97345 & 0.0410 \\ 0.00862 & 0.0403 & 0.999152 \end{pmatrix} \tag{2.4}
$$

The 3×3 unitary Cabibbo–Kobayashi–Maskawa (CKM) matrix expresses the quark mixing [5, 4].

The scalar sector of the SM is not experimentally confirmed yet. The fact that the weak gauge W- and Z-bosons are massive particles indicates that $\mathrm{SU(2)_L} \times \mathrm{U(1)_Y}$ is not a symmetry of the vacuum. In contrast, the photon being massless reflects that $\mathrm{U(1)_{em}}$ is a good symmetry of the vacuum. Therefore, the spontaneous symmetry breaking pattern in the SM must be:

$$
\mathrm{SU(3)_C} \times \mathrm{SU(2)_L} \times \mathrm{U(1)_Y} \longrightarrow \mathrm{SU(3)_C} \times \mathrm{U(1)_{em}}\,. \tag{2.5}
$$

The above pattern is implemented in the SM by means of the so-called Higgs mechanism which provides the proper masses to the W and Z gauge bosons and to the fermions, and leaves as a consequence the prediction of a new particle: the Higgs boson. It must be scalar and electrically neutral. This particle has not been seen in experiments so far.

2.2 Top quark physics

In recent years there have been several reviews of top quark physics which can be found in [6, 7, 8, 9, 10, 11, 12, 13]. Here a brief overview of top quark physics is summarised.

The top quark is the weak-isospin partner to the b-quark, which together constitute the third generation of quarks. The existence of three quark generations was postulated as early as 1973 by Kobayashi and Maskawa since mixing among three generations (and no fewer) could provide a mechanism for CP violation [14]. The b-quark was discovered in 1977 [15] and the search for its weak-isospin partner began in earnest.

From the theoretical point of view the existence of a weak isospin partner of the b-quark was anticipated for two main reasons: First it provides a natural way to suppress the experimentally not observed flavor-changing neutral current. The argument on which the Glashow-Iliopoulos-Maiani (GIM) mechanism [16] is based applies just as well for three as for two quark doublets. The second reason is concerned with the desire to obtain a renormalizable gauge theory of weak interactions. The SM of electroweak interactions can be proven to be renormalisable under the condition that the sum of the weak hypercharges of all left-handed fermions is zero.

The general proof that gauge theories can be renormalized, however, can only be applied if the particular gauge theory is anomaly free. This requires a delicate cancellation between different diagrams, relations which can easily be upset by "anomalies" due to fermion loops. The couplings in such diagrams are related to the number of existing leptons and quarks within a family. The couplings cancell out if the theory has the same number of lepton and quark doublets.

The first direct measurements of top quark production, decay, mass and other properties have been done by the CDF [17] and DO [18] experiments in $p\bar{p}$ collisions at the Fermilab Tevatron collider. First studies were performed during Run I, at $\sqrt{s} = 1.8$ TeV, which was completed in 1996. The measurements have been repeated in higher precision in Run II, which started in 2001 at $\sqrt{s} = 1.96$ TeV.

2.2.1 Motivation for top quark physics

A massive top quark has several properties which make it quite interesting as a probe of known strong and electroweak physics, as well as a sensitive window to potential new physics. Perturbative QCD calculations of top pair production can be carried out with significant precision. Electroweak production of single top quarks gives direct sensitivity to the CKM matrix element $|V_{tb}|$. The value of the top quark mass places an important constraint on the mass of the Higgs boson. It has been speculated that the resulting top quark Yukawa coupling, $y_t \approx 1$, could point to new dynamics beyond the SM. The extremely short predicted lifetime of the top quark of $\sim 5 \times 10^{-25}$ s is an order of magnitude smaller than hadronization timescales and this permits a glimpse of the properties of a bare quark. The decay modes of the top quark may harbor evidence of new physics if alternative models are correct. Measuring the charge of the top quark is important to establish that the top quark is as expected. A direct determination of the $|V_{tb}|$ matrix element probes for potential new physics [9].

2.2.2 Top quark pair production

In hadron collisions, like the $p\bar{p}$ or pp collisions, top quarks can be produced singly or in pairs. The pair production occurs via the strong interaction. In leading order the $t\bar{t}$ production in the gluon fusion and quark anti-quark annihilation processes are shown in Figure 2.6.

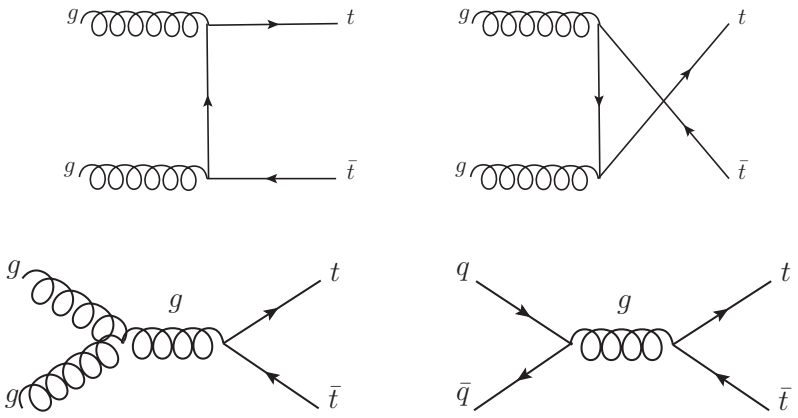

Figure 2.1 Leading-order Feynman diagrams for $t\bar{t}$-pair production via gluon fusion processes and the quark-antiquark annihilation process.

The relative contribution of these diagrams depend on the parton distribution functions (PDF). The PDFs describe the momentum distribution of the quarks and gluons that constitute the protons. Each parton i carries a different momentum fraction x_i in the hadron A and its momentum is given by $p_i = x_i p_A$. The cross sections are calculated as a convolution of PDF's $f_{i/A}(x_i, \mu^2)$ and $f_{j/B}(x_j, \mu^2)$ for the colliding hadrons (A, B) and the factorized hard parton-parton cross section $\hat{\sigma}_{ij}$:

$$\sigma^{AB\to t\bar{t}+X}(s,m_t) = \sum_{i,j=q,\bar{q},g} \int \mathrm{d}x_i \mathrm{d}x_j \, f_{i/A}(x_i,\mu^2) f_{j/B}(x_j,\mu^2) \, \hat{\sigma}^{ij\to t\bar{t}}(\hat{s},m_t^2,\alpha_s(\mu^2),\mu^2) \,. \quad (2.6)$$

The variable $\hat{s}$ denotes the square of the center-of-mass energy of the colliding partons: $\hat{s} = (p_i + p_j)^2 = (x_i p_A + x_j p_B)^2$. The sum runs over all pairs of partons (i, j) contributing to the process. The PDF $f_{i/A}(x_i, \mu^2)$ describes the probability density for finding a parton i inside the hadron A carrying a momentum fraction x_i. The PDFs and $\hat{\sigma}_{ij}$ have a residual dependence on the factorization and renormalization scale μ due to uncalculated higher orders. The scale at which $f_{i/A}$ and $f_{j/B}$ PDFs are evaluated is the factorization scale. The scale at which α_s is evaluated is the renormalization scale, and accounts for divergences coming from loop diagrams. Since both scales are to some extent arbitrary parameters they are chosen to be equal and in the case of top quark production, one typically evaluates the cross sections at $\mu = m_t$. The changes when varying μ between $m_t/2$ and $2m_t$ are usually quoted as an indicative theoretical uncertainty [8].

The PDFs are determined from fits to deep-inelastic-scattering (DIS) cross section measurements performed by a variety of experiments. The fits to the DIS data are performed by a number of different collaborations and are made available as software packages. Common choices are the MRST [19] and CTEQ [20, 21] PDF fits.

The total cross section of top quark pair production has a significant dependence on the top quark mass as shown in Figure 2.2 and on the center-of-mass energy of the colliding hadrons. QCD predictions for hard-scattering cross sections at the Tevatron and the LHC are shown in Figure 2.3. The calculations are done for $p\bar{p}$ and pp, respectively, and therefore the lines are not continuous.

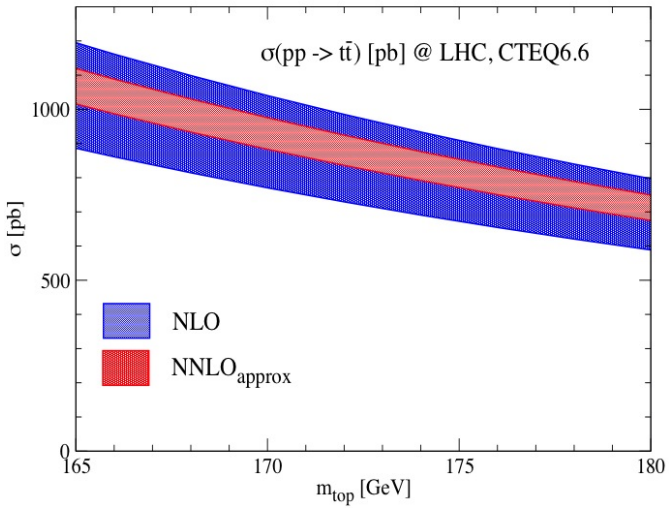

Figure 2.2 $t\bar{t}$ production cross sections as a function of top mass at NLO (blue band) and NNLO (red band) at the LHC [22].

The theoretical prediction for the production rates at the Tevatron and LHC for different center-of-mass energies[1] for a top quark mass of 172.5 GeV and based on CTEQ6.6 are [22]:

$$\begin{aligned} \sigma(p\bar{p} \to t\bar{t}) &= 7.34^{+0.23}_{-0.38} \text{ pb @ Tevatron}\,, \\ \sigma(pp \to t\bar{t}) &= 165^{+11}_{-16} \text{ pb @ LHC 7 TeV}\,, \\ \sigma(pp \to t\bar{t}) &= 874^{+14}_{-33} \text{ pb @ LHC 14 TeV}\,. \end{aligned} \tag{2.7}$$

The increase in rate in LHC can be understood from the structure of the proton. The proton is composed of three valence quarks (two up quarks and one down quark) bound together by gluons. The probability of finding a gluon with fraction x of the proton momentum grows extremely rapidly with decreasing x. At threshold for the $t\bar{t}$ production at Tevatron, each of the two initial partons must carry a large fraction $x = 0.2$

[1] Details are provided in the following chapters.

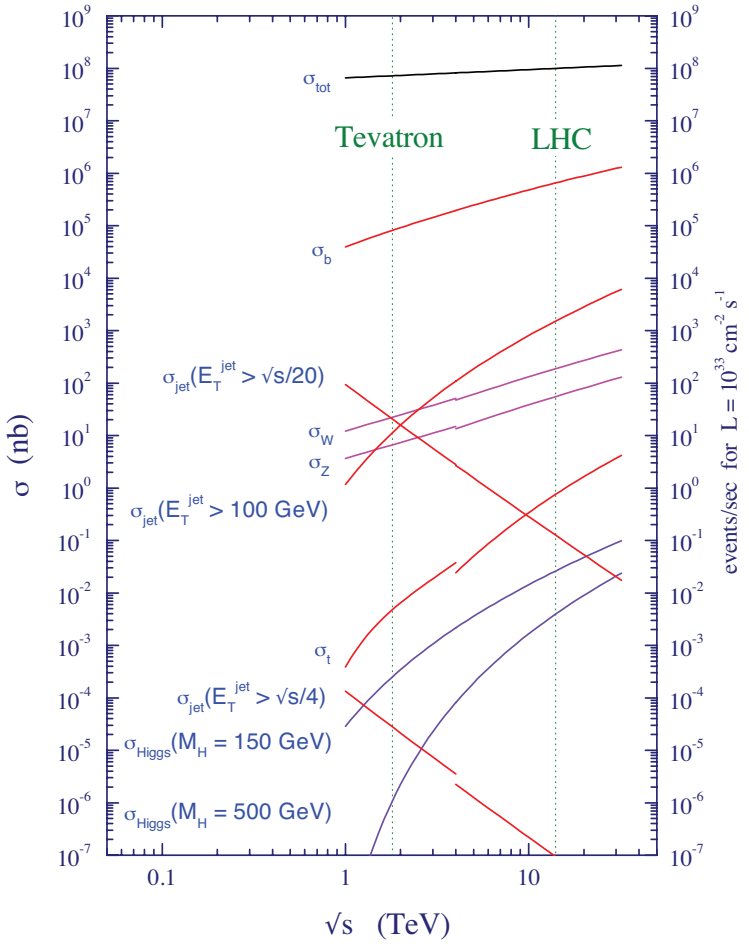

Figure 2.3 Production cross sections for several processes as a function of the center-of-mass energy. The expected cross sections are calculated for $p\bar{p}$ and pp collisions for the Tevatron and LHC energy ranges, respectively, therefore the lines are not continuous [23].

of the proton momentum, so $t\bar{t}$ production is mostly (80-90%) from collisions between valence quarks. At the LHC, the initial partons only need a small fraction $x = 0.02$ of the proton momentum, so $t\bar{t}$ production is mostly (80-90%) from collisions between gluons [7]. Figure 2.4 shows an overview of the CTEQ6.5 parton distribution functions for quarks and gluons, where the gluon PDF increases quickly as the momentum fraction $x \to 0$.

As we have mentioned in the discussion above the top quark production cross section experimentally was measured at Tevaton by the CDF and D0 collaborations. In 2010 first rough measurement was done at LHC by the ATLAS and CMS collaborations using 2.9 pb^{-1} [24] and 3.1 pb^{-1} [25] data collected from 7 TeV pp collisions, respectively. Figure 2.5 shows the measured cross sections as a function of the center-of-mass energy for both colliders. The measurements agree with each other and with theoretical expectations. ATLAS measured the cross section to be $145 \pm 31\,(\text{stat})\ ^{+42}_{-27}\,(\text{syst})$ pb, combing the single-lepton and dilepton channels (discussed later in this chapter), where the mea-

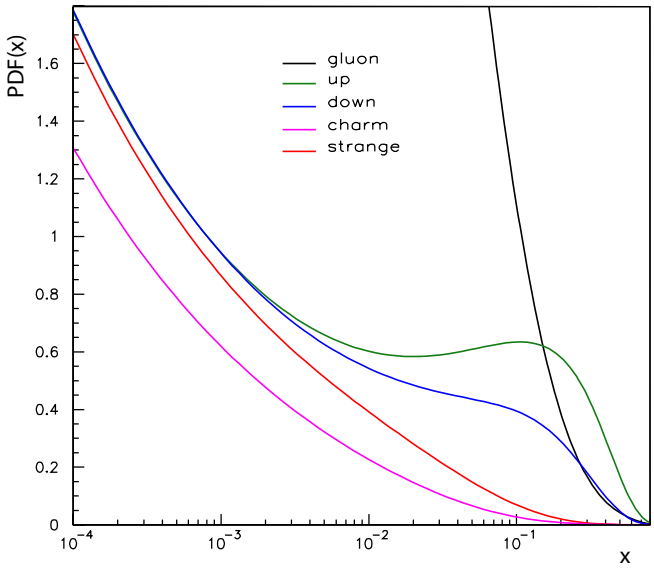

Figure 2.4 PDFs of some of the quarks and gluons inside the proton, using CTEQ6.5 parameterization.

surement is statistically limited. The measurement with 35 pb^{-1} in the dilepton channel is the subject of this dissertation.

2.2.3 Top quark pair decay

Due to its very short life time only the top quark decay products can be measured by the detectors. In the SM two-body decays of the top quark which are possible to lowest order in the gauge couplings are $t \to bW$, $t \to sW$, and $t \to dW$. Their rates are proportional to the squares of the CKM matrix elements $|V_{tq}|^2$, $q = b$, s, d, respectively. The total decay width Γ_t of the top quark is given by the sum of the widths of these three decay modes. The analysis of data from weak decays of hadrons yields $0.9990 < |V_{tb}| < 0.9992$ at 95% C.L., using the unitarity of the CKM matrix [4]. The unitarity relation $|V_{tb}|^2 + |V_{ts}|^2 + |V_{td}|^2 = 1$ implies that the total decay rate is completely dominated by $t \to bW$, therefore $t \to sW$ and $t \to dW$ are not considered in the following discussion.

$$\text{Br}\,(t \to bW) = 0.998, \qquad \text{Br}\,(t \to sW) \simeq 1.9 \times 10^{-3}, \qquad \text{Br}\,(t \to dW) \simeq 10^{-4}\,, \quad (2.8)$$

In the SM, including first order QCD corrections and neglecting terms of order m_b^2/m_t^2, α_s^2 and $(\alpha_s^2/\pi)\, m_W^2/m_t^2$, the top quark total width is [6, 30]:

$$\Gamma_t = \frac{G_F m_t^3}{8\pi\sqrt{2}} |V_{tb}|^2 \left(1 - \frac{m_W^2}{m_t^2}\right)^2 \left(1 + 2\frac{m_W^2}{m_t^2}\right) \left[1 - \frac{2\alpha_s}{3\pi}\left(\frac{2\pi^2}{3} - \frac{5}{2}\right)\right], \quad (2.9)$$

where m_W and m_t are W-boson and top quark masses, respectively, and G_F is the Fermi constant ($G_F = 1.167 \times 10^{-5}$ GeV^{-2}). The width taken at the world average value

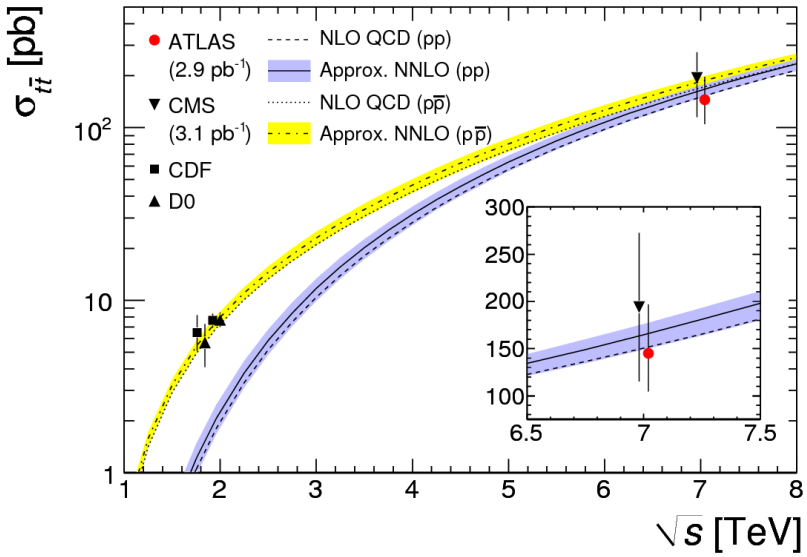

Figure 2.5 Top quark pair-production cross-section at hadron colliders as measured by CDF [26, 27] and D0 [28, 29] at Tevatron, CMS and ATLAS. The theoretical predictions for pp and $p\bar{p}$ collisions include the scale and PDF uncertainties, obtained using the HATHOR tool with the CTEQ6.6 PDFs and assume a top-quark mass of 172.5 GeV [24].

of $m_t = 173.2$ GeV is $\Gamma_t = 1.74$ GeV (using $\alpha_s = 0.118$) and increases with the top mass. With its correspondingly short lifetime of $\approx 5 \times 10^{-25}$ s which is smaller than the characteristic time of the hadron formation $\tau_{\text{had}} \approx 3 \times 10^{-24}$, the top quark is expected to decay before top-flavored hadrons states can form.

As top quark decays almost exclusively to a W-boson and a b-quark, for $t\bar{t}$ events the final state is determined by the decay of the two W-bosons from t and $\bar{t}$, since b-quarks hadronise into B-hadrons. In Figure 2.6 the Feynman diagrams of t- and $\bar{t}$- quark decays are drawn.

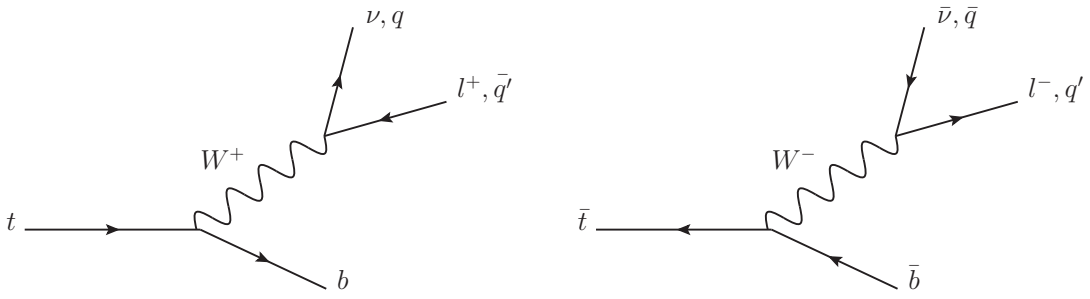

Figure 2.6 Decay of top and anti-top quarks.

W-bosons decay into a pair of quarks, or into a lepton and a neutrino. A W-boson hadronically decays into $u\bar{d}$ and $c\bar{s}$ pairs and each have three color degrees of freedom.

The final states with $c\bar{d}$ and $u\bar{s}$ are Cabibbo-suppressed. As a result, there are six hadronic final sates for W-boson decay. Furthermore, there are three additional final states from leptonically decaying W-bosons, which decay into an electron, a muon or a tau lepton with corresponding flavored neutrinos. Both decay modes together, there are nine possible W-boson final states which are summarized in Table 2.2.

Mother	Decay mode	Fraction	PDG value [4]
	$e^{\pm}\nu_e$	$1/9$	10.75 ± 0.13
	$\mu^{\pm}\nu_\mu$	$1/9$	10.57 ± 0.15
	$\tau^{\pm}\nu_\tau$	$1/9$	11.25 ± 0.20
	$l^{\pm}\nu_l$	$3 \times 1/9 = 1/3$	10.80 ± 0.09
	$q\bar{q}$	$6 \times 1/9 = 2/3$	67.60 ± 0.27

Table 2.2 W-boson decay modes.

Thus for $t\bar{t}$ events the experimental final state can be divided into thee classes depending on the decay modes of two W-bosons:

$$\begin{array}{lllllll} \text{dilepton} & t\bar{t} \to W^+ b & W^- \bar{b} \to l^+ \nu_l b & l^- \bar{\nu}_l \bar{b} & & & (10.3\%) \\ \text{single-lepton} & t\bar{t} \to W^+ b & W^- \bar{b} \to q \bar{q}' b & l^- \bar{\nu}_l \bar{b} & + & l^+ \nu_l b \quad q \bar{q}' \bar{b} & (43.5\%) \\ \text{all hadronic} & t\bar{t} \to W^+ b & W^- \bar{b} \to q \bar{q}' b & q'' \bar{q}''' \bar{b} & & & (46.2\%) \end{array}$$

The three decay modes of $t\bar{t}$ events are characterized as follows:

- **Dilepton channel**: In this channel both W-bosons decay leptonically and thus events consist of two oppositely charged leptons, two b-quarks and large missing transverse energy due to the presence of two neutrinos in the final state that leave the detector without interactions. This is the cleanest channel from the background contamination point of view. There are not many processes with two high transverse momentum leptons in the final state and significant missing transverse momentum. However, the presence of two neutrinos make the full reconstruction of the final state impossible and the branching ratio of the process is relatively small compared with other channels. It is only 10.3% in total which is sliced more finely into three channels with two like-flavor leptons, each with a 1.2% branching fractions (ee, $\mu\mu$, $\tau\tau$) and three channels with two unlike-flavor leptons, each with 2.4% branching fraction ($e\mu$, $e\tau$, $\mu\tau$). Experimentally only two leptons, electron and muon, out of three can be directly observed. Due to the short life time and high mass, only the decay products of the tau lepton can be observed. In case if tau lepton decays into an electron or a muon the process is considered as dilepton. This results in 6.5% branching ratio for the experimentally observable dilepton channel which is used for the analysis presented in this work.

- **Single-lepton channel**: Here one W-boson decays into leptons and the other decays into quarks. The final state is characterized by one lepton, two b-quarks, two light quarks from the hadronic W decay and relatively large missing transverse

energy. Compared to the dilepton channel the branching ratio of this channel is quite high, however at the same time the signal to background ratio is not so high as for the dilepton channel. In spite of the presence of one high transverse momentum lepton the processes as QCD or W-boson production contribute to this channel.

- **All hadronic**: In this channel both W-bosons decay hadronically. The channel is characterized by the presence of two high-p_T b-quarks and four light quarks in the final state. This is the only channel where all final state constituents are available to be observed by the detector and the branching ratio is the highest in this channel, but the lack of any high-p_T lepton in the final state makes it difficult to suppress the contribution from background processes such as QCD multi-jet production.

2.2.4 Single top quark

In contrast to $t\bar{t}$ pair production which is mediated via strong interactions, top quarks can also be produced singly via the weak interaction. There are three different channels for single top quark production, s-channel, t-channel, and Wt-channel. The Feynman diagrams of these processes are sketched in Figure 2.7.

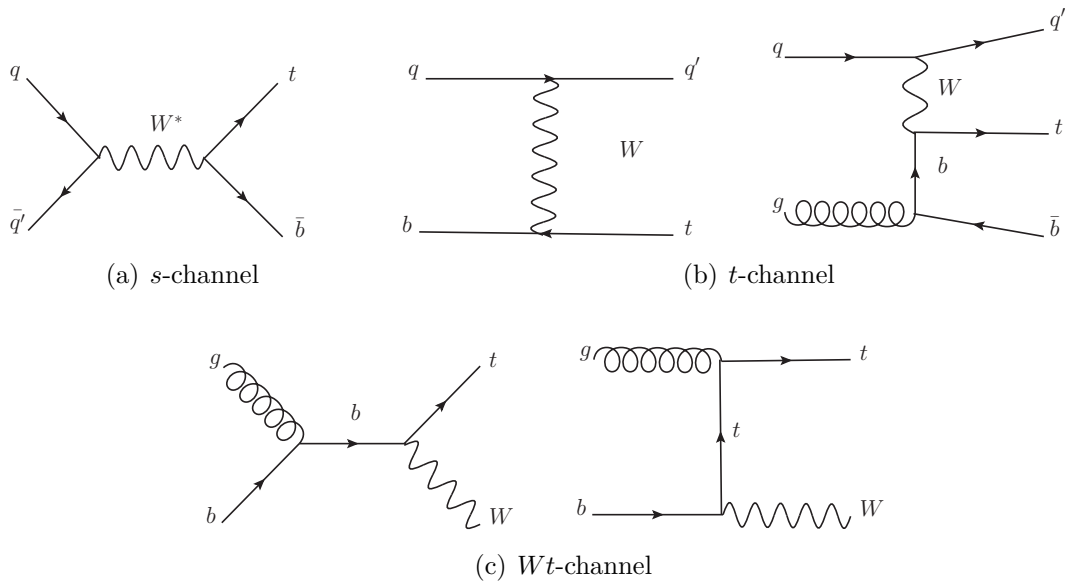

Figure 2.7 Examples of Feynman diagrams for single top production.

The s-channel is characterized by an additional b-quark accompanying the top quark, the t-channel by a forward light quark, and the Wt-channel by the decay products of the W-boson in addition to those of the top quark. Due to the incoming b-quark and gluon, the t-channel and Wt-channel rates are especially sensitive to the corresponding PDFs, which are known with less precision than the PDFs for the valence quarks of the proton. The measured cross sections will therefore provide further constraints on the b-quark and gluon PDFs.

The single top quark cross-section is proportional to $|V_{tb}|^2$. The CDF and D0 experiments have used this relation to convert their cross section measurements to determinations of the CKM element combining the s- and t-channels. The combination of both measurements (expectations) yields a cross section for single top quark production of $2.76^{+0.58}_{-0.47}$ pb (2.9 - 3.5 pb) [31] assuming a top quark mass of 170 GeV in modelling the signal efficiencies. To extract the CKM matrix element it is assumed that $|V_{tb}|$ is much larger than $|V_{td}|$ and $|V_{ts}|$ and no assumption about the unitarity of the CKM matrix is made. With these assumptions the analyses performed to determine the cross section can remain unchanged for the determination of $|V_{tb}|$. Attributing the full deviations of the experimental result from the SM prediction to the value of $|V_{tb}|$ the combined CDF and D0 single top quark production yields:

$$|V_{tb}| = 0.88 \pm 0.07 \qquad |V_{tb}| > 0.77 \qquad 95\%\text{C.L.}\,. \tag{2.10}$$

The searches of single top quark are successfully ongoing at LHC. The expected cross sections for the different channels at $\sqrt{s} = 7$ TeV are listed in Table 2.3.

Channel	Cross section
t-channel	64.6 ± 2.9
Wt-channel	15.7 ± 1.3
s-channel	4.6 ± 0.3

Table 2.3 Expected single top quark production cross sections in different channels at a center-of-mass energy of 7 TeV [32, 33, 34].

The ATLAS experiment presented results for the three different channels using 0.70 fb^{-1} data. For the t-channel there are two analysis performed, using a neural network the measured cross section is $\sigma_t = 107^{+37}_{-31}$ and using cut based approach $\sigma_t = 90^{+32}_{-22}$ [35]. For the Wt-channel the observed limit on production is: $\sigma\left(pp \to Wt + X\right) < 39$ pb at 95% C.L. [36]. For the s-channel the observed limit on production is: $\sigma\left(pp \to t\bar{b} + X\right) <$ 26.5 pb at 95% C.L. [37]. In 36 pb^{-1} of data, CMS uses a boosted decision tree and kinematic observables to separate signal from background, and combines the two measurements to find $\sigma_t = 83.6 \pm 30.0$ pb for the t-channel [38]. For the Wt-channel, using 2.1 fb^{-1} data, CMS measured value of the cross section and 68% C.L. interval is 22^{+9}_{-7} pb [39].

2.2.5 Top quark mass

The top quark mass, m_t, is a free parameter in the SM and must be determined experimentally. A precise determination of m_t is important since quantum loops including top quarks induce large corrections to theory predictions for many precision electroweak observables, including the mass of the Higgs boson.

All electroweak quantities (mass, width and couplings of the W- and the Z-boson) depend in the SM only on five parameters. At leading order this dependence is reduced

to only three parameters, two gauge couplings and the Higgs-field vacuum expectation value. The three best-measured electroweak quantities can be used to determine these three parameters: The electromagnetic coupling constant α, measured in low-energy experiments, the Fermi constant, G_F determined from the μ lifetime, and the mass of the Z-boson, measured in e^+e^- annihilation at LEP and SLC. By defining the electroweak mixing angle θ_W through $\sin^2\theta_W \equiv 1 - m_W^2/m_Z^2$, the W-boson mass can be expressed as:

$$m_W^2 = \frac{\pi\alpha/\sqrt{2}G_\mathrm{F}}{\sin^2\theta_\mathrm{W}\cdot(1-\Delta r)}\,, \tag{2.11}$$

where Δr contains all the one-loop corrections. Contributions to Δr originate from the top quark by the one-loop diagrams shown in Figure 2.8, which contribute to the W and Z masses via:

$$(\Delta r)_\mathrm{top} \simeq -\frac{3\,G_\mathrm{F}}{8\sqrt{2}\pi^2\tan^2\theta_\mathrm{W}} m_t^2\,. \tag{2.12}$$

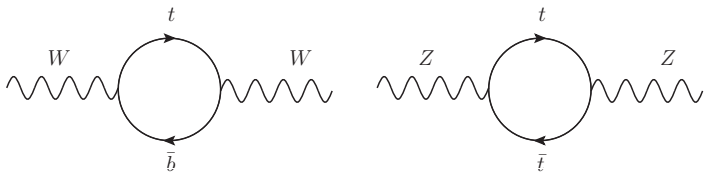

Figure 2.8 Virtual top quark loops contributing to the W- and Z-boson masses.

Also the Higgs boson contributes to Δr via the one-loop diagrams, shown in Figure 2.9.

$$(\Delta r)_\mathrm{Higgs} \backsimeq \frac{3\,G_\mathrm{F}M_W^2}{8\sqrt{2}\pi^2}\left(\ln\frac{m_H^2}{{M_Z}^2} - \frac{5}{6}\right)\,. \tag{2.13}$$

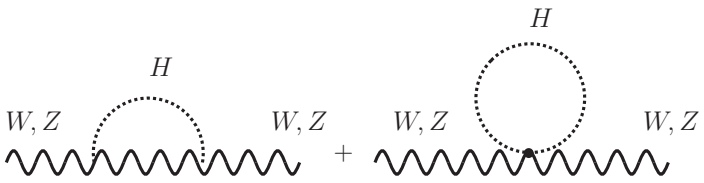

Figure 2.9 Virtual Higgs boson loops contributing to the W- and Z-boson masses.

The top quark mass has been experimentally measured by the CDF and D0 collaborations with 0.5% accuracy. The measured top mass is:

$$m_t = 173.2 \pm 0.9\ \mathrm{GeV}\,. \tag{2.14}$$

The Figure 2.10 shows the most recent combination results of measurements from the CDF and D0 collaborations [40]. The top quark mass is also measured at LHC by the AT-

LAS and CMS collaborations and results in a mass of 175.9±0.9(stat)±2.7(syst) GeV [41] and 173.4 ± 1.9(stat) ± 2.7(syst) GeV [42], respectively.

Improvements in the precision of the measurement of the top quark or the W-boson mass translate into better indirect limits on the Higgs boson mass. Figure 2.11 shows the 68% C.L. contour in the (m_t, m_W) plane from the global electroweak fit. It shows the direct and indirect determination of m_t and m_W . Also displayed are the isolines of SM Higgs boson mass between the lower limit of 114 GeV and the theoretical upper limit of 1000 GeV. As can be seen from the figure, the direct and indirect measurements are in good agreement, showing that the SM is not obviously wrong.

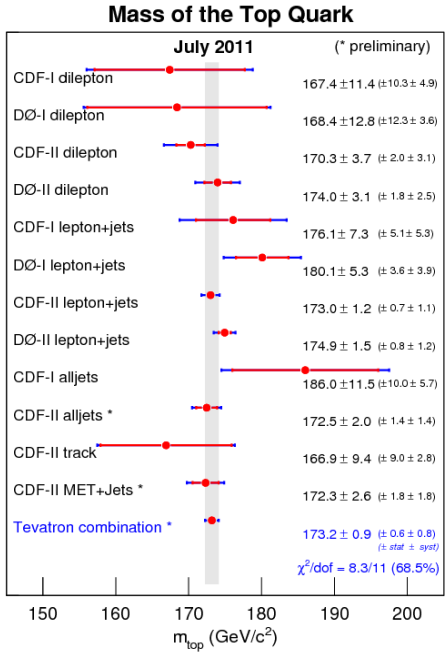

Figure 2.10 Summary of the input measurements and resulting Tevatron average mass of the top quark [40].

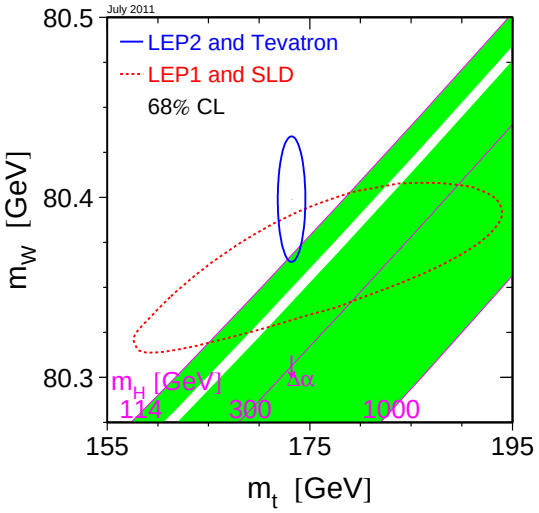

Figure 2.11 Lines of constant Higgs mass on a plot of m_W vs. m_t. The dotted ellipse is the 68% C.L. direct measurement of m_W and m_t. The solid ellipse is the 68% C.L. indirect measurement from precision electroweak data [8].

2.2.6 Other properties of the top quark

Spin correlations

Due to the fact that the life time of the top quark is shorter than the hadronization time scale properties such as the spin correlation in the $t\bar{t}$ system are transferred to the decay

products and can be measured directly via their angular distributions. A measurement of the spin correlation would test the predictions of QCD such as whether the decay of the top quark occurs before its spin is flipped by the strong interaction. The apparent spin correlation may differ from that expected in the SM if, for example, the top quark decays into a scalar charged Higgs boson and a b-quark ($t \to H^+ b$). In addition, many other beyond the SM scenarios predict different production and decay dynamics of the top quark, which could be detected by measuring the spin correlation.

The measurements performed at Tevatron as well as at LHC so far are in agreement with the SM prediction [43].

Charge

The top quark charge measurement is based on reconstructing the charges of the top quark decay products. An exotic charge value of $4e/3$ is in principle not excluded and would decay as $t^* \to bW^-$. To measure the top quark charge one needs to determine the charge of both the W-boson and the b-quark. While the charge of the W-boson can be determined through its leptonic decay, the b-quark charge is not directly measurable, as the b-quark hadronization process results in a jet of hadronic particles (b-jet). It is possible however to establish a correlation between the charge of the b-quark and a weighted sum of the electric charges of the particles belonging to the b-jet. Semileptonic B-hadron decays can also be used.

The possibility that an exotic quark with charge of $-4e/3$ is produced instead of a SM top quark was excluded by the D0 Collaboration at the 92% C.L., by the CDF experiment at the 95% C.L. and by ATLAS experiment the exotic scenario is excluded at more than 5σ [44].

Charge forward backward asymmetry

At leading order in perturbative QCD, $t\bar{t}$ production is predicted to be symmetric under charge conjugation. At next-to-leading order, the processes $q\bar{q} \to t\bar{t}g$ and $qg \to t\bar{t}q$ exhibit a small asymmetry, due to interference between initial and final state gluon emission. The $q\bar{q} \to t\bar{t}$ process also possesses an asymmetry due to the interference between the Born and box diagrams. It is predicted that the top quark will be emitted preferentially in the direction of the incoming quark and the antitop in the direction of the antiquark. Several processes beyond the SM can alter this asymmetry, either with abnormal vector or axial vector couplings or via interference with the SM.

Recent measurements by the CDF and D0 collaborations in $p\bar{p}$ collisions at the Tevatron show a $2-3\sigma$ excess over the SM expectations. However, at LHC ATLAS [45] and CMS [46] achieve preliminary results which are compatible with the SM prediction, showing no evidence for an enhancement from physics beyond the SM.

W-boson helicity

The Wtb-vertex is defined by the electroweak interaction and has a $(V-A)$-structure where V and A are the vector and axial vector contributions to the vertex. As the W-

bosons are produced as real particles in top decays, their polarisation can be longitudinal, left-handed or right-handed. The fractions of events with a particular polarisation, F_0, F_L and F_R, respectively, are referred to as helicity fractions and are predicted in NNLO QCD calculations to be $F_0 = 0.687 \pm 0.005$, $F_L = 0.311 \pm 0.005$, $F_R = 0.0017 \pm 0.0001$ [47]. These fractions can be extracted from measurements of the angular distribution of the decay products of the top quark. Depending on the W-boson helicity (-, 0, +) the charged lepton in the W-boson decay prefers to align with the b-quark direction, stay orthogonal or escape in the opposite direction.

All previous measurements of the helicity fractions, performed by the CDF and D0 collaborations at the Tevatron, and the ATLAS collaboration at the LHC, are in agreement with SM predictions [48].

Flavor changing neutral currents

According to the SM, flavor changing neutral currents (FCNC) are forbidden at tree level and are much smaller than the dominant decay mode at one loop level. Several SM extensions predict higher branching fractions for the top quark FCNC decays. Examples of such extensions are the quark-singlet model, the two-Higgs doublet model with or without flavor-conservation, the minimal supersymmetric model, SUSY with R-parity violation, the Topcolour-assisted Technicolour model or models with warped extra dimensions.

The present experimental limits on the branching fractions of the FCNC top quark decay channels were established by experiments at LEP, HERA, Tevatron and LHC. No evidence for such a signal was found. ATLAS observed a limit at 95% C.L. on the $(t \to qZ)$ FCNC top quark decay branching fraction was set at $\mathrm{BR}(t \to qZ) < 1.1\%$, assuming $\mathrm{BR}(t \to bW) + \mathrm{BR}(t \to qZ) = 1$. The observed limit is compatible with the expected sensitivity, assuming that the SM describes correctly the data, $\mathrm{BR}(t \to qZ) < 1.3\%$ [49].

Chapter 3

The LHC and the ATLAS experiment

3.1 Large Hadron Collider

The Large Hadron Collider (LHC) is a superconducting circular collider at CERN (European Organization for Nuclear Research). The LHC [50, 51] is installed into the existing LEP (Large Electron Positron) collider tunnel which is a 27 km long tunnel and about 100 m beneath the Swiss/French border at Geneva. It is designed to collide proton-proton (pp) and ion-ion (AA) pairs. For pp collisions the machine is designed to run at a center-of-mass energy of 14 TeV with highest luminosity of 10^{34} cm^{-2}s^{-1}.

The LHC collider contains 1232 dipole magnets, which provide a magnetic dipole field of 8.33 T and keep particles in their orbits, and 392 quadruple magnets for focusing the beams. The operating temperature of the magnets is 1.9 K, cooled by super-fluid helium. The proton beam is separated into bunches and each bunch contains $\sim 10^{11}$ protons. Bunches have a spacing of 25 ns which corresponds to a collision frequency of 40 MHz. There are 2808 bunches per beam at the designed luminosity.

Before entering the LHC main ring, protons are accelerated up to 450 GeV by several pre-accelerators, which form the injector chain. Protons are created by an ion source which injects them into a radio-frequency (RF) cavity which accelerates them to 750 keV. After this, they are injected into the Linear Accelerator (LINAC) which brings their energy to 50 MeV. Next, protons are transmitted to the Proton Synchrotron Booster (Booster) which increases the energy up to 1.4 GeV and sends then to the Proton Synchrotron (PS). Protons leave the PS with 25 GeV energy and go to the Super Proton Synchrotron (SPS) where their energy reaches 450 GeV. Afterwards, beams are directed to the LHC tunnel, where two separate proton beams circulating in opposite directions accelerate particles to the maximum value. Figure 3.1 shows an overview of the LHC accelerator complex.

There are four multi-purpose experiments at LHC: ALICE, ATLAS, CMS, and LHCb, and two small special-purpose experiments: LHCf and TOTEM. ATLAS and CMS are designed for precision measurements of SM processes and potential discoveries of Higgs boson, supersymmetry or exotic signatures. ALICE is designed to study the physics of strongly interacting matter and the quark-gluon plasma formation in heavy ion (Pb-Pb) collisions at 5.5 TeV. LHCb is investigating b-quark physics and CP-violation. TOTEM aims at measuring the pp elastic and total cross section at the LHC. LHCf measures neutral particles emitted in the very forward region in LHC collisions, which is motivated

by the need to calibrate hadron interaction models used in the simulation of air showers induced by ultra-high energy cosmic rays.

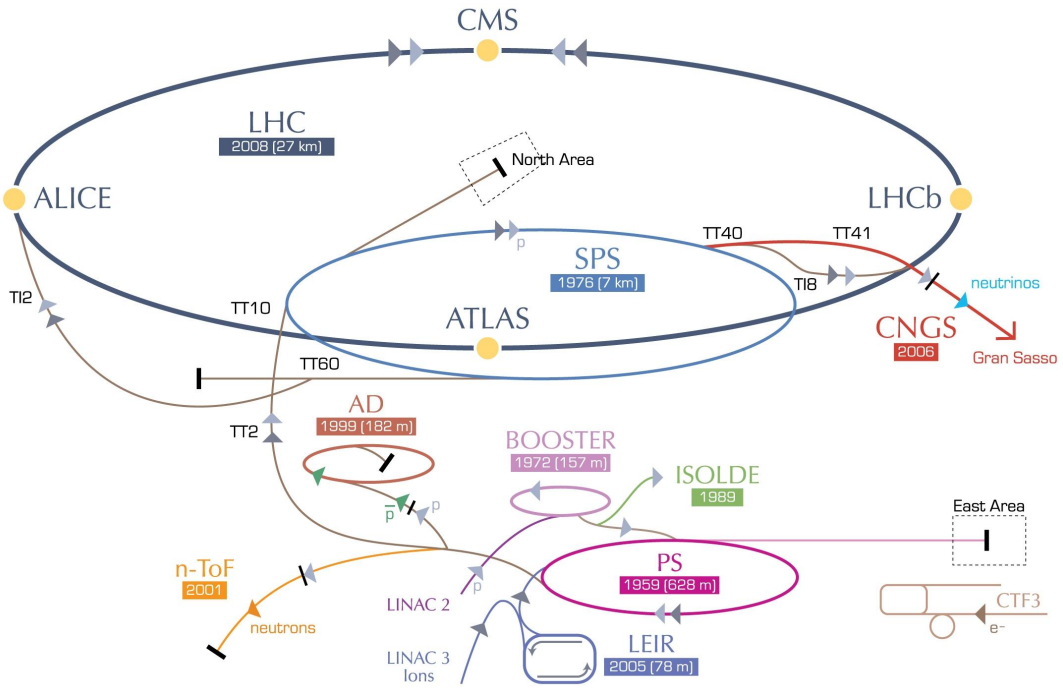

Figure 3.1 CERN accelerator complex [52].

The LHC had first beams injected in September 2008. However during the commissioning an accident occurred, due to faulty electrical connection between two of the accelerator magnets, resulting in a large helium leak into the tunnel. After one year the LHC provided first collisions in November 2009 with a center-of-mass energy of 900 GeV. In 2010 the LHC was successfully running, accelerating protons up to 3.5 TeV, resulting in a center-of-mass energy of 7 TeV. The LHC became the world's highest energy hadron collider. Details of the 2010 run are provided in Section 4.2. In 2011 the LHC team has largely surpassed its operational objectives, steadily increasing the luminosity up to 3.7×10^{33} cm^{-2}s^{-1} and delivering more than 5 fb^{-1} data to the ATLAS and CMS experiments. Five times more than planned. LHC will continue to run until the end of 2012, possibly at a higher collision energy and, after that, it will go into a long shutdown to upgrade detectors. It is planned to have beams back to LHC in the middle of 2014 with energy and luminosity close to the designed values.

3.2 The ATLAS detector

The ATLAS (A Toroidal LHC ApparatuS) detector is a multi-purpose particle detector [53, 54, 55] 25 m high, 44 m long and weighting 7000 tons. It is built around one of the interaction points of the LHC and composed out of three main subdetectors: the

inner detector (ID), the calorimeter and the muon spectrometer (MS). The detector is divided into a barrel part and the two endcaps. The barrel is constructed from cylindrical layers around the beam axis while endcaps are perpendicular to the beam axis. The barrel and two endcaps cover almost the full solid angle around the interaction point, which is defined as the origin of the coordinate system. The beam direction defines the z-axis and the $x-y$ plane is transverse to the beam direction. The positive x-axis is defined as pointing from the interaction point to the center of the LHC ring and the positive y-axis is defined as pointing upwards. The azimuthal angle ϕ is measured around the beam axis, and the polar angle θ is the angle from the beam axis. The pseudorapidity is defined as $\eta = -\ln\tan(\theta/2)$ and the rapidity as $y = 1/2[(E+p_z)/(E-p_z)]$ (used for massive objects such as jets). Distance between physics objects is usually measured in the $\eta-\phi$ space as $\Delta R = \sqrt{(\Delta\eta)^2+(\Delta\phi)^2}$ [55] .

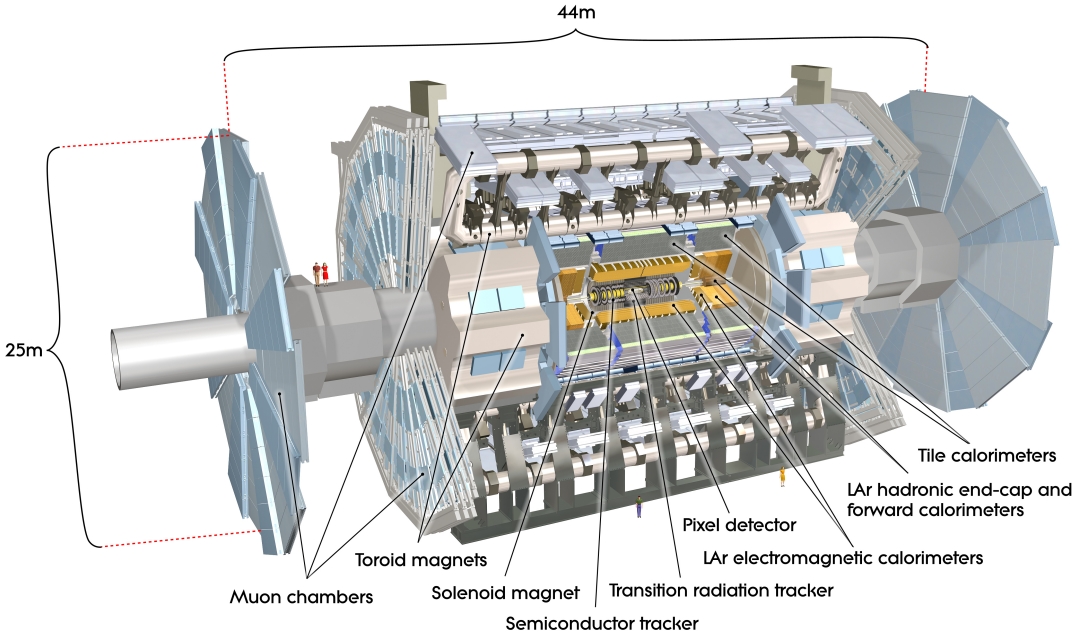

Figure 3.2 A cut-away view of the ATLAS detector.

3.2.1 Inner detector

The ID is the closest detector to the beam pipe, placed inside a solenoid magnetic field of 2T and measures the momenta of charged particles. It has a cylindrical shape with 5.5 m length and 1.15 m radius and contains from three subdetectors: the pixel detector, the semiconductor tracker (SCT) and the transition radiation tracker (TRT). The layout of the ID is illustrated in Figure 3.3 [56, 57].

The ATLAS pixel detector is the innermost tracking detector, which allows for very good transverse impact parameter resolution and 3D-vertexing capability. It consists of

three cylindrical barrel layers with radial range between 5 cm and 12 cm and two endcaps with three discs on each side of the barrel with radial range between 9 cm and 15 cm. With this configuration the pixel detector offers three hits for each track and covers the pseudorapidity range up to $|\eta| < 2.5$. It is built from 1744 identical pixel modules. The nominal pixel size is 50×400 µm^2 (about 90% of the pixels) and is dictated by the readout pitch of the front-end electronics. The size of the remaining pixels is 50×600 µm^2 (long pixels) in the regions at the front-end chips on a module. There are 47232 pixels on each sensor, but for reasons of space there are four ganged pixels in each column of the front-end chip, thus leading to a total of 46080 readout channels [55]. In total the pixel detector has 80.4 million readout channels. The radius of the innermost layer is 50.5 mm and is called *b*-layer. It is an important part of the detector used for identification and reconstruction of secondary vertices in the heavy flavor decay, for example particles containing a *b*-quark or for *b*-tagging of jets [58]. Due to its proximity to the beam line the lifetime of this layer is expected to be approximately 3 years at the designed luminosity of 10^{34} cm^{-2}s^{-1}.

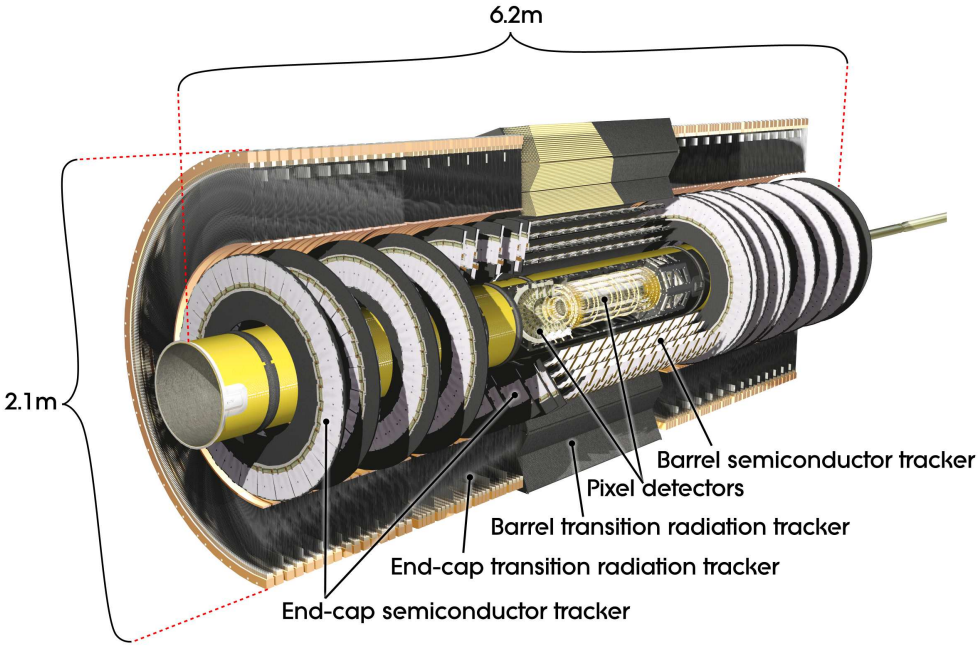

Figure 3.3 A cut-away view of the ATLAS inner detector.

The SCT has quite similar functionality to the pixel detector, but is much larger in surface area than the pixel detector, which allows to measure tracks over longer distance. It consists of four cylindrical barrel layers with radial range between 30 cm and 51 cm and two endcaps with nine discs on each side of the barrel with radial range between 28 cm and 56 cm. There are 4088 modules made of four silicon microstrip sensors glued back to back with 40 mrad stereo angle. The strip pitch is about 80 µm with an intrinsic resolution of 17×580 µm.

The outermost subdetector of the ID is the TRT made of 4 mm diameter straw tubes. It provides typically 30 hits per track within $|\eta| < 2.0$. The TRT provides $R-\phi$ information, for which it has an intrinsic accuracy of 130 µm per straw. In the barrel region, the straws are parallel to the beam axis and are 144 cm long, with their wires divided into two halves, approximately at $\eta = 0$. In the endcap region, the 37 cm long straws are arranged radially in wheels. The total number of TRT readout channels is approximately 351000 [55].

3.2.2 Calorimeters

The purpose of calorimeters is to measure the energy of charged and neutral particles with energy up to few TeV with high resolution and linearity. The calorimeter system consists of an electromagnetic (EM) calorimeter and hadronic calorimeters. Calorimeters cover the range of $|\eta| < 4.9$ which is very important for the precise measurement of missing transverse energy. Figure 3.4 shows an overview of the ATLAS calorimeters. Calorimeters must provide good containment for electromagnetic and hadronic showers, and must also limit punch-through into the muon system [55].

The EM is a lead Liquid Argon (LAr) detector with accordion-shaped geometry, providing complete ϕ symmetry without azimuthal cracks. It is divided into a barrel part and two endcap (EMEC) components each housed in their own cryostat. The barrel calorimeter consists of two identical half-barrels and covers the region of $|\eta| < 1.475$. Between the two barrel components there is a small gap (4 mm) at $z = 0$. Each endcap calorimeter is mechanically divided into two wheels which cover the regions $1.375 < |\eta| < 2.5$ and $2.5 < |\eta| < 3.2$, respectively. The total thickness of the EM calorimeter is greater than 22 radiation lengths in the barrel and 24 radiation lengths in the endcaps. The EM calorimeter is highly segmented with a 3-fold granularity in depth and $\eta \times \phi$ granularity of 0.0003×0.1, 0.025×0.025, and 0.05×0.025, respectively in the front, middle and back compartment [59, 60].

The hadronic calorimeter consists of three parts: tile barrel, endcap (HEC) and forward calorimeters (FCal). The tile barrel is placed behind the EM calorimeter and is using steel as the absorber and scintillator as the active medium. It consists of three parts: the central barrel and two extended barrels, covering a range of $|\eta| < 1.7$. The thickness of the tile calorimetry is designed to be at least nine interaction lengths [61]. The HEC and FCal are Liquid Argon Calorimeters and cover the ranges $1.5 < |\eta| < 3.2$ and $3.1 < |\eta| < 4.9$, respectively. HEC shares the same cryostat with the EMEC and FCal in both endcap regions. The HEC and FCal calorimeter thickness is about 10 interaction lengths.

The transition region or gap between the barrel and end-cap calorimeters is filled with cables and services for the inner detector as well as power supplies and services for the barrel liquid-argon calorimeter. Therefore, the η-region between 1.37 and 1.52 corresponds to the difficult transition region between the barrel and end-cap cryostats, where the energy resolution degrades significantly despite the presence of scintillators in the crack between the barrel and end-cap cryostats to correct for the energy lost in the barrel cryostat flange [55].

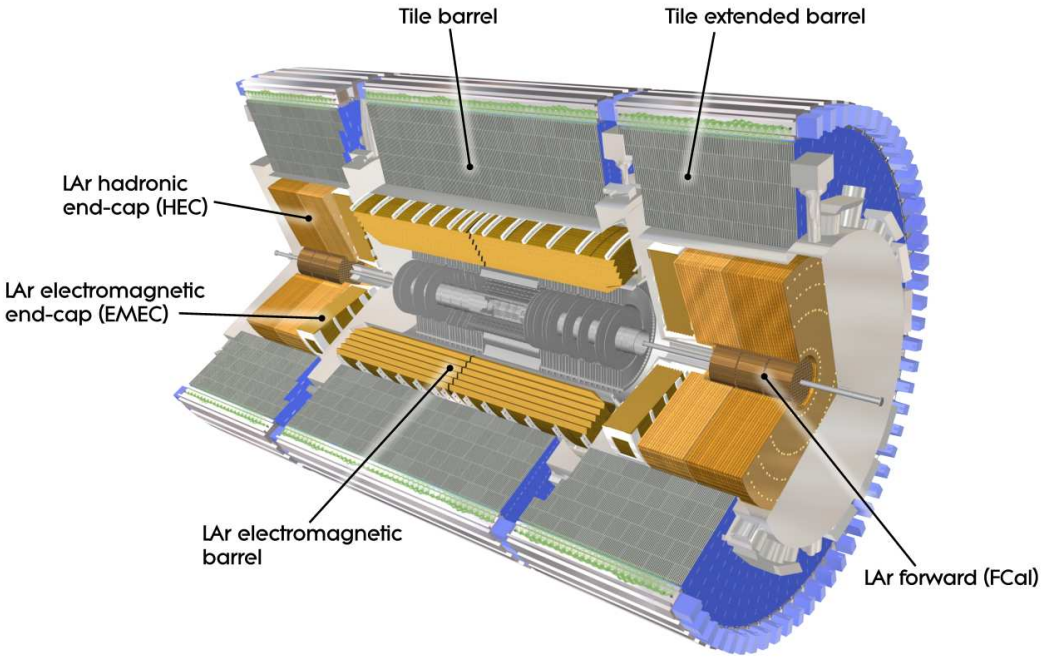

Figure 3.4 A cut-away view of the ATLAS calorimeter.

3.2.3 The muon spectrometer

The layout of the muon spectrometer (MS) together with the toroid magnet system is shown in Figure 3.5. The MS is the largest and outermost subdetector of ATLAS and measures muon momenta within the $|\eta| < 2.7$ region. The MS consists of two types of precision measurement chambers: Monitored Drift Tubes (MDT) and Cathode-Strip Chambers (CSC), and two types of trigger chambers: Resistive Plate Chambers (RPC) and Thin Gap Chambers (TGC).

The toroid magnets consists of a barrel and two endcaps parts, each consist of eight coils placed symmetrically around the beam axis as shown in Figure 3.6. The end-cap toroid coil system is rotated by 22.5 ° with respect to the barrel toroid coil system in order to provide radial overlap and to optimise the bending power at the interface between the two coil systems.

The performance in terms of bending power is characterised by the field integral $\int B_T dl$, where B_T is the field component normal to the muon direction and the integral is computed along an infinite momentum muon trajectory, between the innermost and outermost muon chamber planes. The barrel toroid provides 1.5 to 5.5 Tm bending power in the pseudorapidity range $|\eta| < 1.4$, and the end-cap toroids approximately 1 to 7.5 Tm in the region $1.6 < |\eta| < 2.7$ [55]. The region $1.4 < |\eta| < 1.6$ is covered by a combination of barrel and endcap magnetic fields.

The precision momentum measurement MDT chambers cover the pseudorapidity range of $|\eta| < 2.7$ and consist of three to eight layers of drift tubes, operated at pressures of 3 bar, and achieve an average resolution of 80 µm per tube, or about 35 µm per chamber.

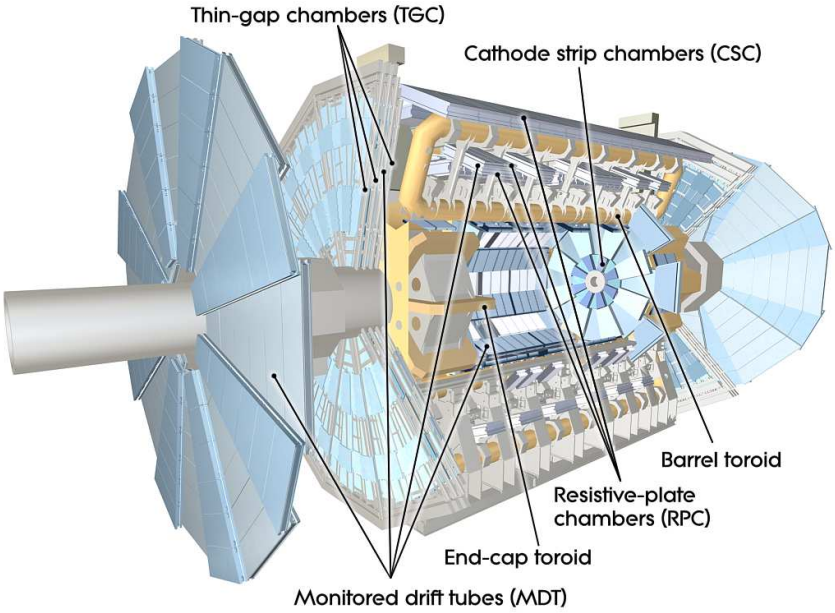

Figure 3.5 A cut-away view of the ATLAS muon system.

In the forward region, ($2 < |\eta| < 2.7$), CSC are used due to their higher rate capability and time resolution. They are multiwire proportional chambers with cathode planes segmented into strips in orthogonal directions. Two trigger chambers RPC and TGC, are covering barrel ($|\eta| < 1.05$) and endcap ($1.05 < |\eta| < 2.4$) regions, respectively. The RPCs are gaseous parallel electrode-plate detectors and TGCs are multi-wire proportional chambers. The main parameters of the MS subsystems are summarized in Table 3.1. The MS trigger chambers provide bunch crossing identification, well defined p_T thresholds and measure the muon coordinate in the direction orthogonal to that determined by the precision tracking chambers [62].

Type	Function	$\delta z/\delta R$	$\delta\phi$	Coverage	Chambers	Channels
MDT	tracking	35 µm (z)	-	$0.0 < \|\eta\| < 2.7$	1150	354k
CSC	tracking	40 µm (R)	5 mm	$2.0 < \|\eta\| < 2.7$	32	30.7k
RPC	trigger	10 mm (z)	10 mm	$0.0 < \|\eta\| < 1.0$	544	373k
TGC	trigger	2-6 mm (R)	3-7 mm	$1.0 < \|\eta\| < 2.4$	3588	318k

Table 3.1 Parameters of the four sub-systems of the muon detector. The quoted spatial resolution (columns 3, 4) does not include chamber-alignment uncertainties.

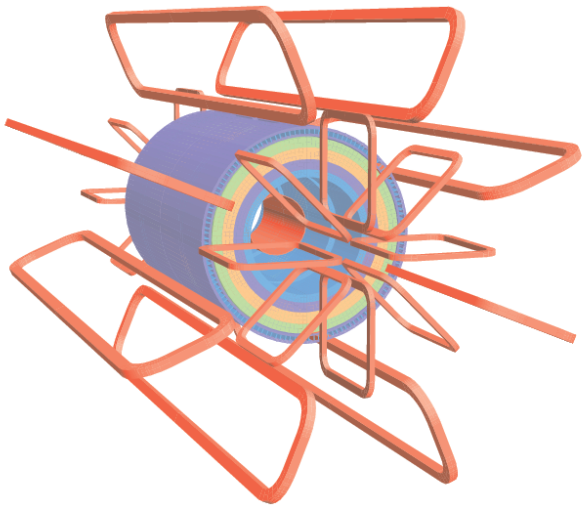

Figure 3.6 The ATLAS toroid magnet system layout.

3.3 Trigger and data acquisition

At the LHC design luminosity 10^{34} cm^{-2} s^{-1} with 25 ns bunch spacing the crossing rate is 40 MHz. The data writing to storage however is limited to 200 Hz. This means that only 0.0005% of the total events can be saved. The trigger task of selecting and saving interesting physics processes for future offline analysis is thus quite challenging.

The trigger system has three distinct levels: Level-1 (L1), Level-2 (L2), and the event filter level (EF). Each trigger level refines the decisions made at the previous level and, where necessary, applies additional selection criteria. The L2 and EF together form the High-Level Trigger (HLT). The L1 trigger is implemented using custom-made electronics, while the HLT is almost entirely based on commercially available computers and networking hardware [55]. A block diagram of the trigger and data acquisition systems is shown in Figure 3.7.

The L1 trigger searches for signatures from muons, electrons/photons, jets and τ-leptons decaying into hadrons. It also selects events with large missing transverse energy and large total transverse energy. The L1 trigger uses reduced-granularity information from a subset of detectors: the RPC, TGC and calorimeter subsystems. It rejects the main part of low-energy events, reducing the rate to 75 kHz and makes a decision within 2.5 µs after the bunch-crossing. Results from the L1 trigger are processed by the Central Trigger Processor (CTP), which implements a trigger "menu" made of trigger items corresponding to different thresholds and signatures. Events passing the L1 trigger selection are transferred to the next stages where all detector channels are read out to the Read Out Drivers (RODs) and then into Read Out Buffers (ROBs). The L1 trigger uses only the multiplicity of the triggered objects, the position information of the objects are not used. In each event, the L1 trigger also defines one or more Regions-of-Interest (RoI's), i.e. the geographical coordinates in η and ϕ, of those regions where its selection process has identified interesting features. This information is subsequently used by the HLT [55].

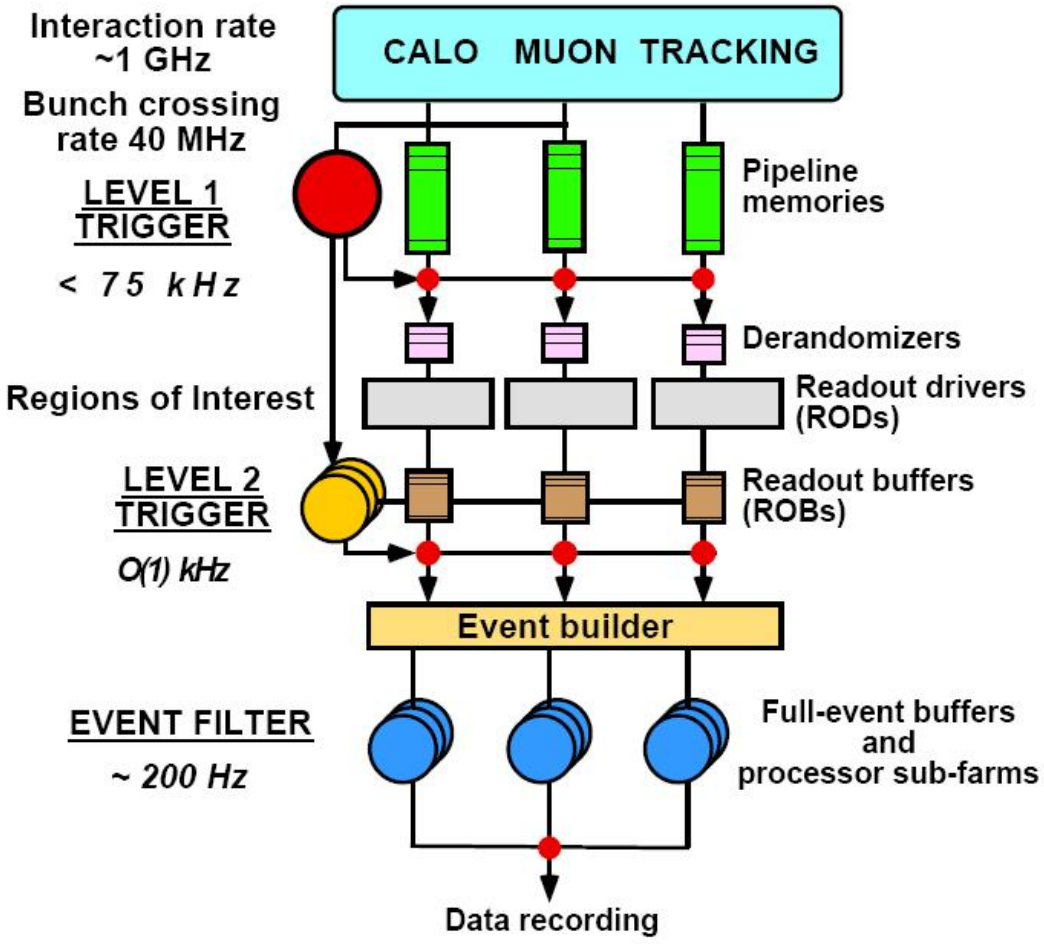

Figure 3.7 ATLAS trigger and data acquisition system.

The L2 trigger uses RoI information on coordinates, energy, and type of signatures to limit the amount of data which must be transferred from the detector readout. The L2 trigger reduces the event rate to below 3.5 kHz, with an average event processing time of approximately 40 ms. The information is stored in the ROBs until the L2 processing finishes. If the event is not rejected by the L2 trigger the events goes to the next trigger level, i.e. EF where the event building process starts.

The EF uses offline analysis procedures and completes the event building procedure. It reduces the event rate to approximately 200 Hz, with an average event processing time of order four seconds. The HLT algorithms use the full granularity and precision of calorimeter and muon chamber data, as well as the data from the inner detector, to refine the trigger selections.

The EF, in addition to the selection, classifies the selected events according to the ATLAS physics streams. The same event can be stored in more than one streams, if several stream requirements are satisfied. The physics data streams are classified as electrons, muons, jets, photons, missing transverse energy, τ-leptons and b-physics. For this analysis data from the electron and muon trigger streams are used.

Chapter 4

Data and Monte-Carlo simulation

4.1 Luminosity

The precise measurement of the luminosity ($\mathcal{L}$) is extremely important for the cross section measurement. At present, ATLAS relies on event counting methods for the determination of the absolute luminosity [63]. Luminosity is defined as:

$$\mathcal{L} = \frac{\mu n_b f_r}{\sigma_{\text{in}}} = \frac{\mu^{\text{vis}} n_b f_r}{\varepsilon \sigma_{\text{in}}} = \frac{\mu^{\text{vis}} n_b f_r}{\sigma_{\text{vis}}}, \tag{4.1}$$

where μ is the number of inelastic proton-proton (pp) collisions per bunch crossing, n_b is the number of bunch pairs colliding at the interaction point, f_r is the revolution frequency (11245.5 Hz) and σ_{in} is the total inelastic pp collision cross section. $\mu^{\text{vis}} \equiv \varepsilon\mu$ is the measured average number of events per bunch crossing, where ε is the efficiency for one inelastic pp collision to satisfy the event selection criteria. The visible cross section $\sigma_{\text{vis}} \equiv \varepsilon\sigma_{\text{in}}$ is the calibration constant that relates the measurable quantity μ^{vis} to the $\mathcal{L}$.

ATLAS determines the relative and absolute luminosity using several detectors and multiple algorithms, each having different acceptances, systematic uncertainties and sensitivity to background, as described in detail in [63, 64]. Currently, ATLAS luminosity scale is calibrated using *van der Meer (vdM)* scans of the beam (also called beam parameter scans) [65], where the absolute luminosity can be inferred from the direct measurements of accelerator parameters:

$$\mathcal{L} = \frac{n_b f_r n_1 n_2}{2\pi \Sigma_x \Sigma_y}, \tag{4.2}$$

where n_1 and n_2 are the number of protons in the beams, Σ_x and Σ_y characterise the horizontal and vertical profiles of the colliding beams. In a *vdM* scan, the observed event rate is recorded while scanning the two beams across each other first in the horizontal (x), then in the vertical (y) direction. This measurement yields two bell-shaped curves, with the maximum rate at zero separation, from which one extracts the values of Σ_x and Σ_y. The luminosity at zero separation can then be computed using Equation 4.2, and σ_{vis} extracted from Equation 4.1 using the measured values of $\mathcal{L}$ and μ^{vis}.

The luminosity is measured and stored for small time intervals called luminosity blocks (`LB`), for which the integrated, dead-time and prescale-corrected luminosity can be determined [64]. The duration of one `LB` is typically from 1 to 2 minutes of data taking,

which depends from run conditions and operational issues. The duration is chosen such that the statistical uncertainty is smaller than the systematic uncertainty which is 100% correlated between the LBs.

The integrated luminosity $\mathcal{L}_{\text{int.}}$ is the luminosity integrated over time, i.e. over LBs. The delivered luminosity is the integrated luminosity over LBs at the interaction region and recorded luminosity is the integrated luminosity over LBs for bunch-crossings where the trigger chain was active.

4.2 2010 ATLAS data

From March 30th to October 31th of 2010, 48.1 pb^{-1} data was delivered and 45.0 pb^{-1} was recorded by ATLAS from pp collisions at $\sqrt{s} = 7$ TeV. The ratio of the recorded to delivered luminosity gives ATLAS data taking efficiency of 93.6% [66]. Figure 4.1 shows the delivered and recorded integrated luminosities as a function of time.

Over time LHC luminosity was rapidly increasing. The peak luminosity was 2.07×10^{32} cm^{-2}s^{-1} which was obtained with a LHC bunch structure of 348 collision bunches in 46 bunch trains, with bunch separation of 150 ns.

The systematic uncertainty of the luminosity measurement is estimated to be 3.4%, dominated by the uncertainty in the beam current product of 2.9%.

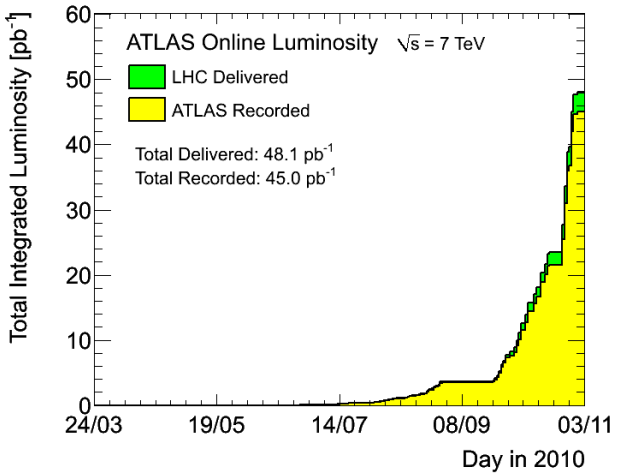

Figure 4.1 Cumulative luminosity versus day delivered to (green), and recorded by (yellow) ATLAS during stable beams and for pp collisions at $\sqrt{s} = 7$ TeV [66].

The data taking was separated into periods in which trigger conditions remained stable. The data taking periods are labeled A-I. Table 4.1 lists periods with run numbers and delivered luminosities for each period. Periods A-D and half of period E are not used for the analysis to simplify the trigger selection and because of the small amount of data.

Problems with detector hardware or the reconstruction software can lead to the reconstruction of unphysical objects [68]. In order to reject events with unphysical objects,

Period	Runs	$\mathcal{L}_{\text{int.}}$
A	152166-153200	0.4 nb^{-1}
B	153565-155160	9.0 nb^{-1}
C	155228-156682	9.5 nb^{-1}
D	158045-159224	0.3 pb^{-1}
E	160387-161948	1.1 pb^{-1}
F	162347-162882	2.0 pb^{-1}
G	165591-166383	9.1 pb^{-1}
H	166466-166964	9.3 pb^{-1}
I	167575-167844	23.0 pb^{-1}

Table 4.1 2010 data taking periods with corresponding run numbers and luminosities [67].

runs and their segments, i.e. LBs, are flagged with three colors as traffic lights depending on the performance of detectors, combined performance objects and triggers. These are so called Data Quality (DQ) flags which are used to create the Good Run Lists (GRL). GRL specify the list of good LBs for each run. The GRL used for this analysis contains 35.3 pb^{-1} filtered data (referred to as 35 pb^{-1} in the rest of this thesis) and includes events passing electron or muon trigger defined in the trigger menu [69].

4.3 Monte-Carlo simulation

The purpose of Monte-Carlo (MC) generators is the simulation of processes resulting from inelastic scattering processes, hard interactions, which we call events. Events in MC are generated according to the theoretical probability distributions. Simulated MC samples can be used to test theoretical models against the detector response, develop analysis strategy, estimate efficiencies, acceptance, resolution of the reconstructed objects, validate reconstruction algorithms, evaluate statistical and systematic uncertainties and so on.

The event simulation process is generally divided into two steps:

- Generation of the event by calculating the production process originating from an inelastic *pp* scattering and immediate decays into a final state of stable particles.
- Simulation of the detector geometry and digitisation of the energy deposited in the sensitive regions of the detector into voltages and currents for comparison to the readout of the detector.

Generation The generation starts with the calculation of the matrix element (ME) at the leading order (LO) of the strong coupling constant α_s, such as hard scattering that produces hard partons in inelastic *pp* scattering. LO matrix element generators are also called tree-level MC generators, which describe final states to lowest order in perturbation

theory, in other words virtual loops are not included in the matrix elements. This implies that all complications involving the regularisation of matrix elements are avoided, and the codes are based either on the direct computation of the relevant Feynman diagrams or on the solutions of the underlying classical field theory [70]. Tree-level matrix element generators can be used for generation of arbitrary or specific processes.

The initial partons are chosen by parton distribution functions (PDF) which parametrise the fraction of momentum carried by a parton in a hadron [20, 21, 71, 19]. The generation procedure itself does not include any form of hadronisation, thus the final states consist of bare quarks, leptons and bosons. Therefore, generators are interfaced to additional programs which are responsible for showering and hadronisation. Higher order effects are added using the parton shower (PS), which allows partons to split into pairs of other partons. The resulting partons are then grouped together or hadronised into color-singlet hadrons and resonances are decayed. Figure 4.2 illustrates the general structure of a hard hadronic scattering event simulated by MC generators.

The underlying structure of the event, beam remnants, multi-parton interactions, initial and final state radiations (ISR/FSR), and pile-up, are superimposed additionally. Beam remnants are the parts of hadrons which did not participate in the hard scattering process. Multi-parton interactions happen when more that two partons participate in a hard interaction. ISR/FSR are the emissions associated with incoming and outgoing particles, respectively. Lastly, due to the large number of particles per bunch, more than one collision can occur simultaneously. The presence of more than one interaction in the same bunch crossing is called pile-up. Pile-up includes also such effects as beam halo, beam gas, cavern background events detector responses to long-lived particles, as well as overlapping detector responses from interactions of neighboring bunch crossings, called out-of-time pile-up.

The generated events can be filtered so that only events with a certain property (*e.g.* leptonic decay or missing energy above a certain value) are kept. The generation is responsible for any prompt decay (*e.g.* t-quark, Z-, W-bosons) but stores all "stable" particles expected to propagate through a part of the detector.

The major part of the generators are designed for LO calculations. Among these are the AcerMC [73, 74] and Alpgen [75]. There are matrix element generators designed for next-to-leading order (NLO) calculations such as MC@NLO [76, 77] and Powheg [78]. For parton showering and hadronisation of single quarks and gluons Pythia [79, 80] and Herwig [81] and for multiple interactions Herwig by the interface to Jimmy [82, 83] can be used. There are many other generators available [84], but only those which are used for this analysis have been included in this discossion.

Simulation The detector response is simulated by transporting generated events through the detector using the simulation toolkit Geant4 [85]. It provides models for physics and infrastructure for particle propagation through a detector geometry. The energies deposited in the sensitive portions of the detector are recorded as "hits" containing the energy deposition, position, and time [86].

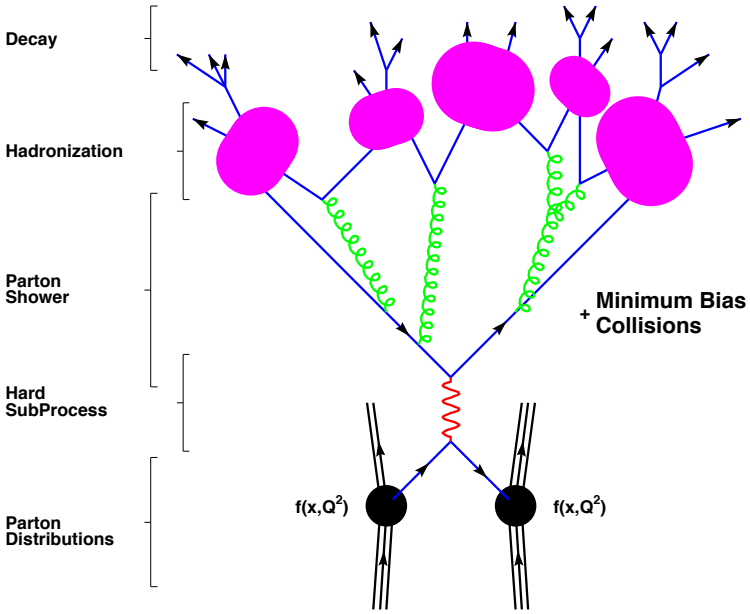

Figure 4.2 Hard hadronic scattering event in the MC generation [72, 70].

At the event generation and detector simulation stages the stored information is called "truth". And the origin of the objects, requiring an association between generated and reconstructed object, can be checked.

The digitization takes the hit output from simulated events; hard scattering signal, underlying event, pile-up, and converts it into detector responses. The information of each subdetector can be presented in either an object-based format or in a format identical to the output of the ATLAS data acquisition system, i.e. similar to the real detector output (raw data). Thus, both the simulated and real data from the detector can then be run through the same ATLAS trigger and reconstruction packages [86].

4.3.1 Monte-Carlo samples

The generation of $t\bar{t}$ signal and single top events uses the MC@NLO v3.41 MC program [76, 87, 77] with PDF set CTEQ6.6 [21] and assuming a top quark mass of 172.5 GeV. The $t\bar{t}$ cross section is normalised using the HATHOR [88] code to 164.57 pb at approximate next-to-next-to leading order (NNLO) in QCD. On the truth level the sample is filtered for single-lepton and dilepton decay final states, which means at least on of the W-bosons from top quark should decay to a neutrino and an electron, a muon or a tau. Single top quark production includes the t, Wt and s channels and the cross section is normalized to the MC@NLO predicted cross section using the "diagram removal scheme" [89] for the Wt process to remove overlaps with the $t\bar{t}$ final state.

Z+jets samples used for the analysis include also the full Drell-Yan contribution from the $\gamma^* \rightarrow ll$ process and take the Z/γ^* interference into account. The generation of

Parameter	ISR ↓ value	ISR ↑ value	Baseline	FSR ↓ value	FSR ↑ value
PARP(64)	4.0	0.25	1.0	1.0	1.0
PARP(67)	0.5	6.0	1.0	1.0	1.0
PARP(72) [GeV]	0.192	0.192	0.192	0.092	0.384
PARJ(82) [GeV]	1.0	1.0	1.0	2.0	0.5

Table 4.2 Parameter variations in PYTHIA used for ISR and FSR samples.

Z/γ^*+jets events uses the ALPGEN v2.13 MC, using the MLM matching scheme [75] and PDF set CTEQ6L1 [20]. The Z/γ^*+jets samples are normalized with an NLO/LO k-factor of 1.25. For these samples the phase space has been restricted to $10 < m_{ll} < 40$ GeV and $40 < m_{ll} < 2000$ GeV regions. Here, so called k-factors are used to scale the cross section from LO simulations to higher order.

Diboson WW ,WZ and ZZ events are modelled using the ALPGEN generator, normalized with appropriate k-factors of 1.26 (WW), 1.28 (WZ) and 1.30 (ZZ) to match the total cross section from NLO QCD predictions using calculations with the MCFM program [90]. Events are hadronised with HERWIG [81], using the JIMMY underlying event model [82, 83]. Both hadronisation programs are tuned to data using the ATLAS MC10 tune [91].

For evaluation of generator, parton shower and hadronisation systematic uncertainties of $t\bar{t}$ both PYTHIA and HERWIG are used to hadronise POWHEG samples, in order to assess the possible differences in acceptane. For ISR/FSR systematic uncertainty estimation nominal and varied samples are generated with ACERMC+PYTHIA. The ISR/FSR samples are produced with increased and decreased initial/final state radiation. The parameters varied to increase and decrease the ISR and FSR are given in Table 4.2. The variation of PARP(64) corresponds to a variation in $1/(\Lambda^{\mathrm{ISR}}_{\mathrm{QCD}})^2$, PARP(67) controls the maximum parton virtuality in space-like parton showers, PARP(72) is $\Lambda^{\mathrm{FSR}}_{\mathrm{QCD}}$ and PARJ(82) is the FSR infra-red cutoff [92]. The evaluation of systematic uncertainties related to MC is discussed in the Chapter 9.

The details of the MC samples are listed in Table 4.3-Table 4.6 [93]. A more detailed descriptions on the MC samples used for signal and background are given elsewhere [92].

ID	Description	ME+PS	σ [pb]	k-factor
105200	No a.h.d.	MC@NLO+ Herwig/Jimmy	80.11	1.12
105205	No a.h.d.	AcerMC+Pythia	58.23	1.53
105860	No a.h.d.	Powheg+Herwig	79.12	1.13
105861	No a.h.d.	Powheg+Pythia	79.12	1.13
117255	No a.h.d. ISR min	AcerMC+Pythia	58.23	1.53
117256	No a.h.d. ISR max	AcerMC+Pythia	58.23	1.53
117257	No a.h.d. FSR min	AcerMC+Pythia	58.23	1.53
117258	No a.h.d. FSR max	AcerMC+Pythia	58.23	1.53

Table 4.3 $t\bar{t}$ samples which do not include all hadronic decays (No a.h.d.). The 105200 sample is used for the nominal analysis, the others are used for systematic evaluation.

ID	Description	ME+PS	σ [pb]	k-factor
108340	tchan $\rightarrow e\nu$	MC@NLO +Herwig/Jimmy	7.12	1
108341	tchan $\rightarrow \mu\nu$	MC@NLO +Herwig/Jimmy	7.12	1
108342	tchan $\rightarrow \tau\nu$	MC@NLO +Herwig/Jimmy	7.10	1
108343	schan $\rightarrow e\nu$	MC@NLO +Herwig/Jimmy	0.47	1
108344	schan $\rightarrow \mu\nu$	MC@NLO +Herwig/Jimmy	0.47	1
108345	schan $\rightarrow \tau\nu$	MC@NLO +Herwig/Jimmy	0.47	1
108346	$Wt \rightarrow$ incl.	MC@NLO +Herwig/Jimmy	14.59	1

Table 4.4 Single top samples.

ID	Description	ME+PS	σ [pb]	k-factor
116250/107650	$Z(\to ee) + 0\text{p}$	Alpgen+Herwig	3055.2 / 668.3	1.25
116251/107651	$Z(\to ee) + 1\text{p}$	Alpgen+Herwig	84.9 / 134.4	1.25
116252/107652	$Z(\to ee) + 2\text{p}$	Alpgen+Herwig	41.4 / 40.5	1.25
116253/107653	$Z(\to ee) + 3\text{p}$	Alpgen+Herwig	8.4 / 11.2	1.25
116254/107654	$Z(\to ee) + 4\text{p}$	Alpgen+Herwig	1.9 / 2.9	1.25
116255/107655	$Z(\to ee) + 5\text{p}$	Alpgen+Herwig	0.5 / 0.8	1.25
116260/107660	$Z(\to \mu\mu) + 0\text{p}$	Alpgen+Herwig	3054.9 / 668.7	1.25
116261/107661	$Z(\to \mu\mu) + 1\text{p}$	Alpgen+Herwig	84.9 / 134.1	1.25
116262/107662	$Z(\to \mu\mu) + 2\text{p}$	Alpgen+Herwig	41.5 / 40.3	1.25
116263/107663	$Z(\to \mu\mu) + 3\text{p}$	Alpgen+Herwig	8.4 / 11.2	1.25
116264/107664	$Z(\to \mu\mu) + 4\text{p}$	Alpgen+Herwig	1.9 / 2.8	1.25
116265/107665	$Z(\to \mu\mu) + 5\text{p}$	Alpgen+Herwig	0.5 / 0.8	1.25
116270/107670	$Z(\to \tau\tau) + 0\text{p}$	Alpgen+Herwig	3055.1 / 668.4	1.25
116271/107671	$Z(\to \tau\tau) + 1\text{p}$	Alpgen+Herwig	84.9 / 134.8	1.25
116272/107672	$Z(\to \tau\tau) + 2\text{p}$	Alpgen+Herwig	41.5 / 40.4	1.25
116273/107673	$Z(\to \tau\tau) + 3\text{p}$	Alpgen+Herwig	8.4 / 11.3	1.25
116274/107674	$Z(\to \tau\tau) + 4\text{p}$	Alpgen+Herwig	1.9 / 2.8	1.25
116275/107675	$Z(\to \tau\tau) + 5\text{p}$	Alpgen+Herwig	0.5 / 0.8	1.25

Table 4.5 Z/γ^*+jets (Drell-Yan) samples with phase space cuts 10 GeV $< m_{ll} <$ 40 GeV(left) and $m_{ll} > 40$ GeV(right).

ID	Description	ME+PS	σ [pb]	k-factor
107100	$WW(\to l\nu l\nu) + 0\text{p}$	Alpgen+Herwig	2.10	1.26
107101	$WW(\to l\nu l\nu) + 1\text{p}$	Alpgen+Herwig	1.00	1.26
107102	$WW(\to l\nu l\nu) + 2\text{p}$	Alpgen+Herwig	0.45	1.26
107103	$WW(\to l\nu l\nu) + 3\text{p}$	Alpgen+Herwig	0.18	1.26
107104	$W(\to \text{incl.})Z(\to ll) + 0\text{p}$	Alpgen+Herwig	0.67	1.28
107102	$W(\to \text{incl.})Z(\to ll) + 1\text{p}$	Alpgen+Herwig	0.41	1.28
107106	$W(\to \text{incl.})Z(\to ll) + 2\text{p}$	Alpgen+Herwig	0.22	1.28
107107	$W(\to \text{incl.})Z(\to ll) + 3\text{p}$	Alpgen+Herwig	0.10	1.28
107108	$Z(\to \text{incl.})Z(\to ll) + 0\text{p}$	Alpgen+Herwig	0.51	1.30
107109	$Z(\to \text{incl.})Z(\to ll) + 1\text{p}$	Alpgen+Herwig	0.23	1.30
107110	$Z(\to \text{incl.})Z(\to ll) + 2\text{p}$	Alpgen+Herwig	0.09	1.30
107111	$Z(\to \text{incl.})Z(\to ll) + 3\text{p}$	Alpgen+Herwig	0.03	1.30

Table 4.6 Diboson samples.

Chapter 5

Reconstruction, identification and selection of objects

5.1 Electrons

5.1.1 Reconstruction of electrons

Electrons, being charged particles, leave tracks in the inner detector (ID) and produce showers in the electromagnetic (EM) calorimeter. Photons are neutral particles and do not leave tracks in the ID (as long as they do not convert in the material of the ID) and the EM showers induced by photons are very similar with the showers induced by electrons. In order to separate electrons from photons, electrons are reconstructed from ID tracks in association with EM calorimeter clusters.

There are three offline algorithms for electron reconstruction in ATLAS [94, 95, 96].

- `egammaBuilder` is the standard algorithm at ATLAS, designed for reconstruction of high-p_{T}, isolated electrons. This algorithm is also used for isolated photon reconstruction. It starts from the reconstruction of clusters with transverse energy above 2.5 GeV in the EM calorimeter, using a `sliding window` algorithm [97] among (longitudinal) towers of 3×5 cells of size 0.025×0.025 in $\eta \times \phi$ space, corresponding to the granularity of the calorimeter middle layer [98].

  A cluster is formed from a fixed size rectangular window and its position is choosen such so the amount of energy within the cluster is maximum. The size of the cluster is different for different particles. For instance electrons produce larger clusters than photons, since for electrons the sign-corrected $\Delta\phi$ window is larger on the side where the extrapolated track bends as it traverses the tracker magnetic field.

  The `egammaBuilder` algorithm matches a track to the cluster in the middle layer in a $\Delta\eta \times \Delta\phi$ window of 0.05×0.10. The electron candidates are obtained by matching EM clusters with energy E to tracks in the ID with momentum p, without applying any special requirement for E/p [94, 95]. For true isolated electrons with $E_T > 20$ GeV and $|\eta| < 2.5$ the selection efficiency is above 90%. Here, $E_T = E_{\mathrm{cluster}}/\cosh(\eta_{\mathrm{track}})$, which means E_T is constructed from the calorimeter cluster energy E_{cluster} and the direction of the electron track, η_{track}.

- `softeBuilder` is seeded from the ID tracks. This algorithm is optimised for low p_{T} electrons and selects good-quality tracks matching a relatively isolated deposition of energy in the EM calorimeters [95].

- The `egammaForwardBuilder` algorithm is dedicated for reconstruction of electrons in the forward region of the detector, i.e. $2.5 < |\eta| < 4.9$. Contrary to `egammaBuilder` and `softeBuilder` algorithms this algorithm does not require track matching because of the limited coverage of the ID ($|\eta| < 2.5$). It uses the information from the calorimeters and the topological clusters based on connecting neighboring cells.

In this analysis electron candidates reconstructed by `egammaBuilder` algorithm or by `egammaBuilder` and `softeBuilder` algorithms at the same time are used [99, 100].

5.1.2 Identification of electrons

The baseline electron identification in the central region ($|\eta| < 2.47$) relies on a cut-based selection using calorimeter, tracking and combined variables that provide good separation between signal electrons, background electrons (primarily from photon conversions and Dalitz decays) and jets faking electrons. The cuts can be applied independently. Three reference sets of cuts have been defined in ATLAS with increasing background rejection power: *loose*, *medium* and *tight* with an expected jet rejection of about 500, 5000 and 50000, respectively, as estimated from MC simulation [98].

For *loose* selection hadronic leakage variables and shower shape variables of the EM calorimeter middle layer are used. These variables efficently help to reject high energy jets with wide showers, since with respect to jets electrons and photons produce narrower showers and they deposit energy in the electromagnetic calorimeter, while jets deposit most part of thier energy in the hadronic calorimeter. The *loose* selection cuts provide excellent identification efficieny, but low background rejection. Variables from the EM calorimeter strip layer, track quality requirements and track-cluster matching are added at *medium* selection. The *medium* selection increases the jet rejection by a factor of 3-4 with respect to the *loose* selection, but at the same time it reduces the identification effciency by 10%. The *tight* selection adds E/p, particle identification using the TRT, and discrimination against photon conversions via a b-layer hit requirement and information about reconstructed conversion vertices [98]. Table 5.1 gives the list of all variables used in the *loose*, *medium* and *tight* selections. The cuts are optimised in 10 bins of cluster η (defined by calorimeter geometry, detector acceptances and regions of increasing material in the ID) and 11 bins of cluster E_T from 5 GeV to above 80 GeV [101, 98].

For data collected during 2010 we use the "ElectronTight_WithTrackMatch" definition [99] of electrons. It belongs to the *tight* classification in Table 5.1, including an additional requirement of matching between a track to the electron cluster.

Type	Description	Variable
Loose selection		
Acceptance of the detector	⋆ $\|\eta\| < 2.47$	
Hadronic leakage	⋆ Ratio of E_T in the first layer of the hadronic calorimeter to E_T of the EM cluster (used over the range $\|\eta\| < 0.8$ and $\|\eta\| > 1.37$) ⋆ Ratio of E_T in the hadronic calorimeter to E_T of the EM cluster (used over the range $\|\eta\| > 0.8$ and $\|\eta\| < 1.37$)	R_{had1} R_{had}
Second layer of EM calorimeter	⋆ Ratio in η of cell energies in 3×7 versus 7×7 cells ⋆ Lateral width of the shower	R_η w_{η_2}
Medium selection (includes loose)		
First layer of EM calorimeter	⋆ Total shower width ⋆ Ratio of the energy difference associated with the largest and second largest energy deposit over the sum of these energies	w_{stot} E_{ratio}
Track quality	⋆ Number of hits in the pixel detector (≥ 1) ⋆ Number of hits in the pixels and SCT (≥ 7) ⋆ Transverse impact parameter (<5 mm)	 d_0
Track matching	⋆ $\Delta\eta$ between the cluster and the track (< 0.01)	$\Delta\eta_1$
Tight selection (includes medium)		
b-layer	⋆ Number of hits in the b-layer (≥ 1)	
Track matching	⋆ $\Delta\phi$ between the cluster position in the track (< 0.02) ⋆ Ratio of the cluster energy to the track momentum ⋆ Tighter $\Delta\eta$ cut (< 0.005)	$\Delta\phi_2$ E/p $\Delta\eta_1$
Track quality	⋆ Tighter transverse impact parameter cut (<1 mm)	d_0
TRT	⋆ Total number of hits in the TRT ⋆ Ratio of the number of high-threshold hits to the total number of hits in the TRT	
Conversions	⋆ Electron candidates matched to reconstructed photon conversions are rejected	

Table 5.1 Definition of variables used for *loose*, *medium* and *tight* electron identification cuts for the central region of the detector with $|\eta| < 2.47$ [101].

5.1.3 Electron isolation

The cuts listed in the Table 5.1 do not include a dedicated cut for isolation as the requirements are different for various analyses. Therefore isolation cuts are applied after the electron identification, which are based on calorimeter and track variables.

A calorimeter isolation discriminator is computed from the reconstructed energy in a cone of half opening angle R_0 around the electron candidate direction, where the energy of the electron itself is excluded. While a larger cone will contain more energy in case of misidentified jets, a smaller cone is more robust against energy depositions from pile-up events [101].

A second, tracking based discriminator uses the summed scalar p_T of tracks in a cone around the electron. In contrast to the calorimetric isolation, neutral particles do not contribute to this quantity. The advantage, however, is that track quality criteria can be applied in order to reject tracks from secondary vertices [101].

Currently there are four sets of cuts defined that exploit calorimetric and tracking isolation variables, allowing to retain 99%, 98%, 95% or 90% of isolated electrons, respectively. The default isolation criteria based on tracking and calorimeter variables have been optimised to keep 95% of isolated electrons from Z-boson decays.

For top quark analyses we use the calorimeter based isolation with a cone $R_0 = 0.2$, `EtCone20`. Figure 5.1 shows the mean of the `EtCone` distributions for three cone sizes of 0.2, 0.3 and 0.4 as a function of the electron E_T for electrons from W-bosons in $t\bar{t}$ decays [102, 103]. As it can be seen from the plot the surrounding energy as measured by `EtCone20` does not tend to zero as $E_T \to 0$ GeV. This is caused by calorimeter noise and the offset increases with the size of the isolation cone.

We apply an electron isolation requirement of `EtCone20` < 4 GeV [99].

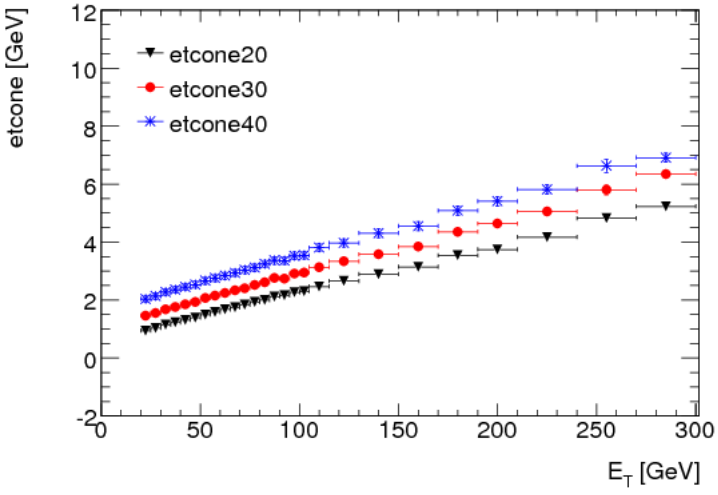

Figure 5.1 The `EtCone20`, `EtCone30` and `EtCone40` distribution mean values as a function of the electron E_T in MC simulation of electrons from W-bosons in $t\bar{t}$ decays [102].

5.1.4 Electron energy scale offset and resolution smearing

Measurements of the electron energy scale and resolution have been derived from the measurement of the $Z \to ee$ invariant mass distribution [104, 102]. The electron energy scale is quantified by a dimensionless scaling parameter α:

$$E_{\text{corr}} = \frac{E}{1+\alpha}\,, \tag{5.1}$$

where E is the electron energy and E_{corr} is its energy after the offset correction. α is determined by constraining the peak position of the dielectron invariant mass distribution from Z-boson in data as a function of the electron pseudorapidity.

An offset of less than 2% in the central region ($|\eta| < 2.5$) is observed. Systematic uncertainties are within 2–3% (except for crack region of $1.37 < |\eta| < 1.52$ where it is $\pm 5\%$), dominated by uncertainties from the the detector material and the presampler energy scale, but also include the event selection, pile-up, and hardware modelling. A software tool is provided to correct the energy for electrons in data [105], including systematic uncertainties.

Also the energy resolution in the calorimeter is measured using the di-electron invariant mass from Z-bosons. A simultaneous analysis of Z events from MC simulation and data is used to extract the energy resolution parameters, in particular the constant term, which is dominant for high energy electrons [102]. The energy resolution function is given by [104]:

$$\frac{\sigma_E}{E} = \frac{a}{\sqrt{E}} \oplus \frac{b}{E} \oplus c\,, \tag{5.2}$$

where parameters a and c have to be determined. b is the noise term which has a significant contribution only at low-energies. The difference of resolution between data and MC is measured in terms of the constant c, which includes both, the calorimeter constant term and the inhomogeneities from possible extra-material. Table 5.2 shows the constant terms needed in MC simulation to correctly reproduce the lineshape of the Z-boson peak measured in data [102].

5.1.5 Electron efficiency scale factors

Simulations were made to agree with the data by applying efficiency scale factors as multiplicative event weights. The weights are multiplicative scale factors for reconstruction,

	Constant term
Barrel	$1.1\% \pm 0.1(\text{stat}) \pm 0.2(\text{sys})$
EMEC outer-wheel	$1.8\% \pm 0.4(\text{stat}) \pm 0.2(\text{sys})$
EMEC inner-wheel	$4.0\% \pm 0.3(\text{stat}) \pm 2.0(\text{syst})$

Table 5.2 The measured constant term of the electron energy resolution.

identification and trigger efficiencies [106]. The efficiencies are measured separately by tag-and-probe methods using $Z \to ee$ and/or $W \to e\nu$ decays [107]. The ratios of the data to MC efficiencies ($\varepsilon_{\text{data}}/\varepsilon_{\text{MC}}$) are the scale factors (SF).

- The reconstruction efficiency is defined as the probability for an electron depositing its energy in a calorimeter cluster to be reconstructed as an electron candidate by the `egammaBuilder` algorithm. For 2010 data the electron reconstruction SF is estimated to be $\text{SF}^{\text{reco}} = 1.000 \pm 0.015$ [106]. The uncertainty includes statistical and systematic uncertainties.

- The identification efficiency has been defined with respect to electron candidates passing the track quality requirements. Independent measurements have been done on $Z \to ee$ and $W \to e\nu$ samples, using several E_T and η bins. Results from two measurements are combined, with largely uncorrelated systematic uncertainties, and the total uncertainty is significantly reduced. The table with SF^{id}'s together with their uncertainties is shown in Table A.1.

- The trigger efficiency is defined as the fraction of offline identified probes "firing" the trigger: offline selection criteria for which the trigger implementation is designed to be almost 100% efficient in the plateau region are considered [107]. The analysis has shown that data-MC differences have little dependence on electron E_T and η and thus an integrated value of the scale factor have been considered in physics analyses. For the e15_medium trigger, used in this analysis, the plateau efficiency normalized to offline cuts is above 99% with an associated systematic uncertainty of less than 1% [108]. The estimated data/MC scale factor is $\text{SF}^{\text{trig}} = 0.995 \pm 0.005$.

The trigger scale factor is derived from a single-lepton scale factor if only one lepton was found to match the trigger objects. In case both leptons can be matched to trigger objects the scale factor is $(1-(1-\text{SF}_1^{\text{trig}})(1-\text{SF}_2^{\text{trig}}))$, which accounts for the probability that either of the two selected leptons in a given event can pass the trigger requirements. For events with one or two selected muons, the corresponding muon trigger scale factors are used from Table 5.5.

5.1.6 Selection of electrons

Electrons are selected among candidates in the `ElecronAODCollection` with $E_T > 20$ GeV. The candidates are required to be reconstructed in the central part of the detector with $|\eta| < 2.47$, excluding the calorimeter crack region from 1.37 to 1.52. The last quality cut used for electron selection is designed for rejection of electrons built from clusters affected by some detector problems [109].

5.2 Muons

5.2.1 Reconstruction and identification of muons

The ATLAS detector has excellent muon identification capabilities, with an efficiency greater than 95% and a fractional momentum resolution better than 3% over a wide transverse momentum range. There are four types of muon candidates with different reconstruction procedures, *standalone muon, combined muon, segment tagged muon* and *calorimeter tagged muon*, which are using information from the muon spectrometer, the calorimeter and the inner detector [110, 111, 112, 95]. Below short descriptions of the reconstruction and identification of muon candidates are listed [112]:

- *Standalone muon*: The muon trajectory is reconstructed in the muon spectrometer only. The muon momentum measured in the spectrometer is corrected for the parameterized energy loss of the muon in the calorimeter, to obtain the momentum at the interaction point. The average muon energy loss in the calorimeter is 3 GeV. The direction of flight and the impact parameter of the muon at the interaction point are determined by extrapolating the spectrometer track back to the beam line.

- *Combined muon*: The momentum of the standalone muon is combined with the momentum measured in the inner detector. The muon trajectory in the inner detector also provides information about the impact parameter of the muon trajectory with respect to the primary vertex.

- *Segment tagged muon*: A trajectory in the inner detector is identified as a muon if the trajectory extrapolated to the muon spectrometer can be associated with straight track segments in the precision muon chambers.

- *Calorimeter tagged muon*: A trajectory in the inner detector is identified as a muon if the associated energy depositions in the calorimeters is compatible with the hypothesis of a minimum ionizing particle.

Standalone muons are reconstructed in the whole acceptance range of the muon spectrometer $|\eta| < 2.7$. Combined and segment tagged muons are restricted to the acceptance of the inner detector of $|\eta| < 2.5$. The calorimeter tagged muons cover the acceptance gap of the muon spectrometer at $|\eta| \sim 0$.

For each strategy there are at least two reconstruction algorithms in Athena [113, 114] software. These algorithms are grouped into two families, such that each family includes at least one algorithm for each strategy. These families are named Staco and Muid. Staco family uses MuonBoy, STACO and MuTag algorithms for standalone, combined and tagged muons, respectively [115]. Muid family has Moore and MuidStandalone algorithms for standalone muons, MuidCombined for combined muons, MuGirl and MuTagIMO for tagged muons [116].

The difference of the two families comes from the combination approach of the information from subdetectors. Muons from the Staco family are reconstructed by statistically

combining the track extrapolated to the interaction point with the matching inner detector track [111]. In contrast, Muid does not merge statistically the two independently found tracks, but it performs a global fit of all hits associated with the tracks, taking into account the calorimeter mass profile which is approximated by two scattering planes [117].

For top quark analysis we are using muons from Muid collection, which are reconstructed by the MuidCombined algorithm. In order to facilitate analysis a set of criteria have been made that categorize the muons as *loose*, *medium* or *tight* [118]. Unlike the electron case muon qualification does not rely on a cut-based selection, instead it checks which reconstruction and identification algorithm has found the muon. For the Muid collection the qualification is performed as follows:

- *tight*: MuidCombined or MuidStandalone at |eta|>2.5 or MuGirl with extended track
- *medium*: Tight or MuidStandalone or MuGirl with extended track
- *loose*: Medium or MuGirl or MuTagIMO

For this analysis combined Muid muons within the *tight* category are used.

5.2.2 Muon isolation

Similar to electrons there are calorimeter and track isolation categories for muons to reject background muons coming from heavy and light flavour decays, such as baryon and meson decays formed by b- and c-quarks.

Muons in the minimum bias data are predominantly produced from meson decays with high energy deposit in the calorimeter. Figure 5.2 shows the transverse energy deposited in the calorimeters in a cone with radius $R_0 = 0.3$ normalized to the transverse momentum of the muon as a function of the distance of the muon to the closest jet with $p_T > 5$ GeV. It is obvious from the distribution that the isolated muons at $\Delta R > 0.4$ have deposited only very little energy while muons in jets show much larger energy around them in the calorimeter [111].

For this analysis both calorimeter and track based isolations are used with a cone of $R_0 = 0.3$, requiring that both the transverse energy deposit and transverse momentum of the tracks should be below 4 GeV.

5.2.3 Muon momentum resolution scale and smearing

The momentum resolution is measured from the width of the dimuon invariant mass distribution in $Z \to \mu\mu$ decays and from comparisons of the individual inner detector and muon spectrometer momentum determination for combined muons from $W \to \mu\nu$ decays [119].

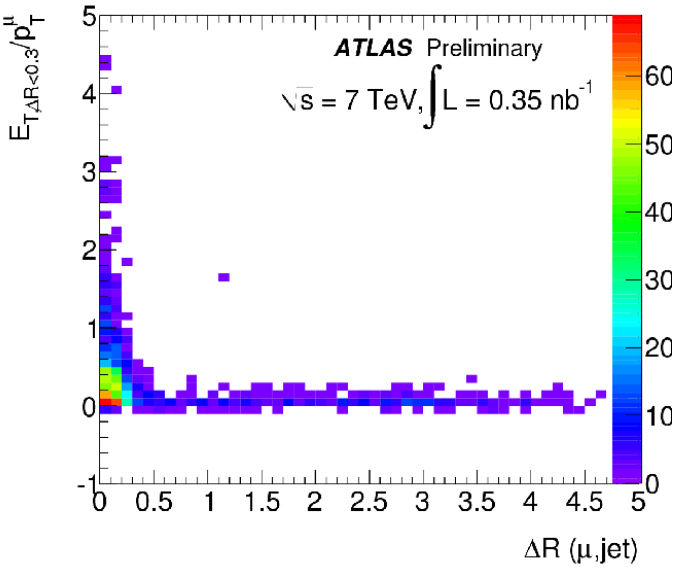

Figure 5.2 The transverse energy deposited in the calorimeters in a cone of $\Delta R = 0.3$ normalized to the transverse momentum of the muon as a function of the distance to the closest jet. No overlap removal between muons and jets is performed [111].

The relative resolution on the momentum measurement, $\frac{\sigma(p_T)}{p_T}$, is dictated by different effects related to the amount of material that the muon traverses, the spatial resolution of the individual track points and the degree of internal alignment of the two subsystems.

The muon spectrometer (MS) is designed to provide a uniform momentum resolution as a function of the pseudorapidity. The resolution can be parameterized in the following way as a function of the transverse component p_{T} [119, 120]:

$$\frac{\sigma(p_T)}{p_T} = \frac{p_0^{MS}}{p_T} \oplus p_1^{MS} \oplus p_2^{MS} \times p_T \,, \tag{5.3}$$

where p_0^{MS}, p_1^{MS} and p_2^{MS} are coefficients related to the energy loss in the calorimeters material, to multiple scattering and to intrinsic resolution, respectively.

For the inner detector (ID) a similar parameterization is used assuming uniform response in the central part and a rapidly worsening resolution beyond the central region. The following approximate parameterization is used:

$$\frac{\sigma(p_T)}{p_T} = p_1^{ID} \oplus p_2^{ID} \times p_T \ (|\eta| < 1.9) \,, \tag{5.4}$$

$$\frac{\sigma(p_T)}{p_T} = p_1^{ID} \oplus p_2^{ID} \times p_T \times \frac{1}{\tan^2(\theta)} \ (|\eta| > 1.9) \,, \tag{5.5}$$

where θ is the muon polar angle [119].

The results from $Z \to \mu\mu$ and $W \to \mu\nu$ studies are merged using a combined fit for four different pseudorapidity regions.

For the MS and ID the transformation is the following:

$$p'_T(MS,ID) = p_T(MS,ID)\ (1 + \Delta(MS,ID))\,, \tag{5.6}$$

where

$$\Delta(MS) = f(0,1)\ \Delta_{p_1}^{MS} + f(0,1)\ \Delta_{p_2}^{MS}\ p_T\,, \tag{5.7a}$$

$$\Delta(ID) = f(0,1)\ \Delta_{p_2}^{ID}\ p_T\ (|\eta| < 1.9)\,, \tag{5.7b}$$

$$\Delta(ID) = f(0,1)\ \Delta_{p_2}^{ID}\ p_T/\tan^2(\theta)\ (|\eta| > 1.9)\,, \tag{5.7c}$$

where $p'_T(MS,ID)$ indicates the simulated muon p_T after applying corrections and $f(0,1)$ is a normally distributed random number with mean 0 and width 1. The values of the additional smearing $\Delta(ID)$ and $\Delta(MS)$ are obtained from a χ^2 minimization fit to the overall spectrum. The variation of the $p_i^{ID,MS}$ parameters is performed by rescaling the simulated muon p_T [119]. The fitted correction parameters are provided in Table A.2 together with their statistical and systematic uncertainties.

The values of the correction parameters quantify the increase in momentum resolution in data when compared to simulation. The full parameterization of the experimental momentum resolution is obtained by adding quadratically the uncorrected simulated resolution terms of Equation (5.3)-(5.5) and the corresponding corrections from Table A.2. The uncertainties are directly propagated from those of the correction parameters and the statistical errors on the uncorrected MC simulated resolution. The results for the full parameterization are listed in Table 5.3.

The combined muon momentum measurement is determined by the relative weights of the ID and MS momentum measurements in the track fit. Due to the large amount of calorimeter material between ID and MS, the two measurements can be treated as uncorrelated. Therefore, starting from the corrected ID and MS p_T measurements in

	MS			ID	
η region	p_0^{MS}(TeV)	p_1^{MS}(%)	p_2^{MS}(GeV^{-1})	p_1^{ID}(%)	p_2^{ID}(TeV^{-1})
$0 < \|\eta\| < 1.05$	0.23 ± 0.01	3.75 ± 0.10	0.24 ± 0.04	1.60 ± 0.32	0.49 ± 0.04
$1.05 < \|\eta\| < 1.7$	0	8.80 ± 0.46	0.30 ± 0.16	2.60 ± 0.54	0.95 ± 0.10
$1.7 < \|\eta\| < 2.0$	0	4.77 ± 0.35	0.23 ± 0.12	3.40 ± 0.58	1.39 ± 0.05
$2.0 < \|\eta\| < 2.5$	0.17 ± 0.02	4.87 ± 0.65	0.90 ± 0.25	4.10 ± 0.50	0.140 ± 0.004

Table 5.3 Resolution parameterization as defined in Equation (5.3)-(5.5) in the MS and ID. The measurements are obtained by adding the correction parameters in quadrature to the uncorrected momentum resolution from simulation [119].

MC, the combined muon $p_T(CB)$ can be corrected in the simulation, obtaining a new measurement, $p'_T(CB)$. The new MC simulated measurement is the linear combination of the MS and ID contributions, weighted by the MS and ID resolutions:

$$p'_T(CB) = p_T(CB)[1 + \frac{\Delta(MS)w_{MS} + \Delta(ID)w_{ID}}{w_{MS} + w_{ID}}], \tag{5.8}$$

where

$$w_{MS,ID} = \frac{1}{\sigma^2(MS,ID)}. \tag{5.9}$$

$\Delta(MS,ID)$ is the overall correction to the simulated MS and ID p_T, from Equation (5.6), and $\sigma(MS,ID)$ are the values for the resolution at that $p_T(MS,ID)$, taken from Table 5.3.

5.2.4 Muon efficiency scale factors

Similar to the electron case there are reconstruction, identification and trigger multiplicative scale factors for muons determined by the tag-and-probe method using $Z \to \mu\mu$ events. Muon efficiency scale factors are listed below:

- The trigger efficiency in data and MC simulation and resulting scale factors are studied as a function of η and ϕ since disagreement between data and MC for these variables is observed [102]. Binned muon trigger scale factors are shown in Table 5.4. No data/MC disagreements which depend on p_T and $\Delta R(\mu, \text{closest jet})$ are found.

- Reconstruction and identification efficiencies do not show any dependence on geometric, kinematic or isolation quantities [102]. The estimated scale factors for muon reconstruction, identification and reconstruction+identification with their statistical and systematic uncertainties are given in the Table 5.5.

5.2.5 Selection of muons

For this analysis muons are selected from combined Muid candidates qualified as *tight* with transverse momentum $p_T > 20$ GeV and from the central part of the detector $|\eta| < 2.5$ [121]. Muons overlapping with any jet (with $p_T > 20$ GeV) within $\Delta R < 0.4$ are removed in order to suppress muon candidates from heavy flavor decays. The following ID hit requirements are used as well for muon selection:

- Number of B-Layer hits > 0, if the `expectBLayerHit` returns `true`
- Number of pixel hits + number of crossed dead pixel sensors > 1
- Number of SCT hits + number of crossed dead SCT sensors ≥ 6

Regions		
η range	ϕ range	SF value
$\lvert\eta\rvert > 1.05$	any ϕ	$0.987 \pm 0.003\ ^{+0.001}_{-0.001}$
[-1.05, 0.6]	$[-\pi, 5\pi/16] \bigcup [11\pi/16, \pi]$	$1.026 \pm 0.010\ ^{+0.003}_{-0.002}$
[-1.05, 0.6] $\bigcup$ [-0.6, -0.5] $\bigcup$ [-0.4, 0.2] $\bigcup$ [0.3, 0.6]	$[5\pi/16, \pi/2]$	$0.919 \pm 0.017\ ^{+0.007}_{-0.000}$
[-1.05, 0.6]	$[\pi/2, 11\pi/16]$	$0.952 \pm 0.030\ ^{+0.002}_{-0.003}$
[-0.6, 0.6]	$[-\pi, 5\pi/16] \bigcup [11\pi/16, \pi]$	$1.009 \pm 0.006\ ^{+0.001}_{-0.002}$
[-0.5, -0.4] $\bigcup$ [0.2, 0.3]	$[5\pi/16, \pi/2]$	$0.657 \pm 0.050\ ^{+0.010}_{-0.000}$
[-0.6, 0.6]	$[\pi/2, 11\pi/16]$	$0.906 \pm 0.019\ ^{+0.000}_{-0.004}$
[0.6, 1.05]	$[-\pi, 5/16\pi] \bigcup [11\pi/16, \pi]$	$1.005 \pm 0.010\ ^{+0.002}_{-0.003}$
[0.6, 1.05]	$[5\pi/16, \pi/2]$	$0.843 \pm 0.053\ ^{+0.000}_{-0.013}$
[0.6, 1.05]	$[\pi/2, 11\pi/16]$	$1.046 \pm 0.029\ ^{+0.011}_{-0.009}$

Table 5.4 Muon trigger scale factors from $Z \to \mu\mu$ data and MC events, using the tag-and-probe method. The results correspond to an integrated luminosity of 37 pb^{-1} [102].

Scale factors		
Reconstruction	Identification	Reco+Id
$0.997 \pm 0.001\ \pm 0.003$	$1.002 \pm 0.001\ \pm 0.001$	$0.999 \pm 0.002\ \pm 0.003$

Table 5.5 Offline scale factors, using the tag-and-probe method. The results correspond to an integrated luminosity of 37 pb^{-1}. The uncertainties are statistical and systematic [102].

- Number of pixel holes + number of SCT holes < 2
- TRT: denote n = number of TRT hits + number of TRT outliers
  - for $|\eta| < 1.9$ and $n > 5$ and number of TRT outliers$/n < 0.9$
  - for $|\eta| \geq 1.9$ and $n > 5$: number of TRT outliers$/n < 0.9$

Finally, for dilepton analysis we reject muons arising from cosmic rays by removing muon candidate pairs that are back-to-back in the $r - \varphi$ plane and that have transverse impact parameter relative to the beam axis $|d_0| > 0.5$ mm.

5.3 Jets

5.3.1 Jet reconstruction algorithms

All jets are composed from constituents, be they particles, calorimeter cells or other objects. In ATLAS several jet finding algorithms have been implemented since there is no universal way for reconstruction of jets.

The obvious way to combine energy and momenta of the constituents into four-momenta of the final jet is to simply add the four-vectors:

$$p^k = \sum_i p^i \,. \tag{5.10}$$

For all algorithms this four-vector recombination scheme is used as base [122].

The major goals of the jet finding algorithm are infrared and collinear safety and order independence [95]. Infrared safety means any soft particle not coming from the fragmentation of a hard scattered parton should not effect the number of jets produced. Collinear safety means that jet reconstruction should be independent of the fact that a certain amount of transverse momentum is carried by one particle, or if a particle is split into two collinear particles. Order independence means that the same hard scattering should be reconstructed independently at parton-, particle- or detector level.

Cone algorithms aim to maximize energy in a geometric cone where the radius of the cone is a key parameter. Most frequently used cone algorithms are "iterative" seeded, which means a candidate cone is identified, its momentum vector is calculated and the cone is redrawn around the new center [122]. The seed is usually a calorimeter tower or cluster, parton or particle with a p_T above some threshold. The seeded algorithms have been shown to be not infrared nor collinear safe [123]. Therefore, the Seedless Infrared Safe Cone algorithm (SISCone) has been developed [124] which is infrared and collinear safe at all orders of α_s, and suitable for use at parton level, hadron level and detector level.

Cluster algorithms are based on pair-wise clustering of the initial constituents of the input calorimeter towers and clusters. A distance measure between objects and some conditions on which clustering should be terminated are defined. The distance between two objects i and j and between object i and beam are defined as:

$$d_{ij} = \min(k_{Ti}^{2p}, k_{Tj}^{2p}) \frac{(\Delta R)_{ij}^2}{R^2}\,, \tag{5.11a}$$

$$d_{iB} = k_{Ti}^{2p}\,, \tag{5.11b}$$

where

$$(\Delta R)_{ij}^2 = (y_i + y_j)^2 + (\phi_i - \phi_j)^2\,, \tag{5.12}$$

where $k_{Ti,Tj}$, $y_{i,j}$ and $\phi_{i,j}$ are the transverse momentum, rapidity and azimuth of the objects i and j, respectively. R is a parameter of the algorithm, setting the resolution at which jets are resolved from each other as compared to the beam.

There are three algorithms and for each of them the variable p takes different values in Equation (5.11). For the $\mathtt{k_T}$ algorithm $p = 1$, which means objects with low relative k_T are merged first [125, 126, 127, 128]. For the `Cambridge/Aachen` algorithm $p = 0$, where objects near to each other in ΔR are merged first [129]. Finally, for the $\mathtt{anti\text{-}k_T}$ algorithm $p = -1$ [130]. In this case soft particles will tend to cluster with hard ones long before they cluster among themselves. If a hard particle has no hard neighbors within a distance $2R$, then it will simply accumulate all the soft particles within a circle of radius R, resulting in a perfectly conical jet. If two comparably hard objects are within $R < \Delta R < 2R$ of each other, energy will be shared between them depending on their relative k_T and distance.

The main advantage of the $\mathtt{anti\text{-}k_T}$ algorithm is that it is infrared safe. Moreover, it is very cone-like and therefore it is experimentally easier to handle [131]. This algorithm is used for jets in this analysis.

5.3.2 Jet energy scale

Reconstructed jets are calibrated as a baseline to the energy scale measured by the electromagnetic and hadronic calorimeters called the electromagnetic (EM) scale. The electromagnetic energy scale is established using test-beam measurements for electrons and muons in the electromagnetic and hadronic calorimeters [132]. It gives the correct response for the energy deposited in electromagnetic showers for photons and electrons, while it does not correct for the hadron response due to some energy losses (like binding energy losses in post-collision nuclear break-up), dead material, imperfect energy collection of the clustering algorithm and so on [133]. The goal of the jet energy scale (JES) calibration is to correct the energy and momentum of the jets measured in the calorimeter to those of the jet at the hadronic scale [134, 135].

In ATLAS several calibration schemes have been developed [95, 136, 135]. For the first data the simpler jet-by-jet correction is applied as a function of jet transverse momentum and pseudorapidity, denoted as EM+JES calibration which allows for direct evaluation of

the systematic uncertainty. The calibration scheme consists of the following subsequent steps [134]:

- The average additional energy due to pile-up is subtracted from the energy measured in the calorimeters using correction constants extracted from an in-situ measurement [137].

- The position of the jet is corrected such that the jet direction points to the primary vertex of the interaction instead of the geometrical center of the ATLAS detector.

- The jet energy and position as reconstructed in the calorimeters are corrected using constants derived from the comparison of the kinematics of reconstructed jets and corresponding truth jets in MC simulation.

The calibration restores the jet energy scale within 2% for the full kinematic range. The EM+JES calibration is validated in-situ up to the TeV scale [138] by exploiting the conservation of transverse momentum in events which contain a photon and a hadronic jet in the central region of the detector. The EM scale is validated as a function of p_T^{γ} and η^{jet} and the data/MC agreement is within 5% [135].

The uncertainty on the JES is the largest source of systematic uncertainty for many analyses. It is determined for jets reconstructed from topological clusters with `anti-k`$_{\mathrm{T}}$ for $R = 0.4$ and $R = 0.6$. In the early stage the JES uncertainty has been derived from inclusive di-jet events by convolving the uncertainty on the single particle response with the jet particle composition [139].

Now, the JES uncertainty is significantly reduced since it is derived for 16 pseudorapidity bins for isolated jets by combining information from in-situ and single pion test-beam measurements, uncertainties on the material budget of the ATLAS detector, the description of the electronic noise, and the MC modeling used in the event generation [134]. The jet energy scale uncertainty is found to be similar for $R = 0.4$ and $R = 0.6$ jets. In the central region $|\eta| < 0.8$ the uncertainty is 4.6% and 2.5% for jets with $p_T > 20$ GeV and $60 < p_T < 800$ GeV, respectively. In the endcap and forward regions the JES uncertainty is about 14% for the most forward pseudorapidities up to $|\eta| = 4.5$.

However, jets are produced with nearby jets in a busy environment such as found in QCD multi-jets or top quark pair production, and thus a separate study was done to determine the additional JES uncertainty for jets with nearby jet activity. The studies have shown that the close-by jet systematic uncertainty on the JES is 1.7-2.7% and 2.3-2.8% for $R = 0.4$ jets with $20 < p_T < 30$ GeV and $p_T > 30$ GeV, respectively [140].

The JES uncertainty due to pile-up is also estimated separately as a function of the number of primary vertices. In the case of two primary vertices per event, the uncertainty for jets with $p_T = 20$ GeV and pseudorapidity $0.3 \leq |\eta| < 0.8$ is about 1% while it amounts to about 2% for jets with pseudorapidity $2.1 \leq |\eta| < 2.8$. For jets with transverse momentum above 200 GeV, the uncertainty due to pile-up is negligible ($< 1\%$) in the full pseudorapidity range ($|\eta| < 4.5$) [134].

5.3.3 Jet energy resolution

The jet resolution is measured with two different data-driven methods for anti-k$_T$ jets calibrated by EM+JES scheme. They are the *di-jet balance* method which is based on momentum conservation in the transverse plane and the *bi-sector* method which is based on the definition of an imbalance (transverse) vector, defined as the vector sum of the two leading jets in the di-jet event [141, 142].

The fractional jet energy resolution, σ_{p_T}/p_T is parameterized as:

$$\frac{\sigma_{p_T}}{p_T} = \frac{N}{p_T} \oplus \frac{S}{\sqrt{p_T}} \oplus C\,, \tag{5.13}$$

where N, S and C are the noise, stochastic and constant terms. The typical values of N, S and C are 2.5, 0.7 and 0.05, respectively [143]. In order to get the final jet p_T resolution for both methods, the MC simulation result is fitted using Equation 5.13. The MC simulation reproduces the resolutions measured on the data within statistical fluctuations of $\pm 10\%$ for jets in different rapidity regions, up to $|y| < 2.8$.

For each of the two methods, the results from applying them to data and MC are found to agree within 2% [144].

5.3.4 Jet reconstruction efficiency

The jet reconstruction efficiency was studied by matching calorimeter jets to track jets [141, 145]. It is determined applying the tag-and-probe method which is based on a di-jet back-to-back event topology. The highest p_T track jet in the event is defined as the tag object ($p_T > 15$ GeV), and a second track jet is considered the probe object. The probe has to balance the tag jet by requiring a $|\Delta\phi| \leq 2.8$. Events with additional track-jets reconstructed in the $|\Delta\phi|$ window are rejected. The matching calorimeter reconstruction efficiency with respect to track jets is defined as the fraction of probe jets which are matched to a calorimeter jets in $\Delta R(probe, calo - jet) < 0.4$.

MC simulation and data efficiencies agree within 5% for calorimeter jets with $p_T \geq 15$ GeV and within 2% for calorimeter jets with $p_T \geq 20$ GeV. The systematic uncertainty on the jet reconstruction efficiency is 2%.

5.3.5 Selection of jets

Jets are selected form the AntiKt4TopoEMJets collection reconstructed from topological clusters using the anti-k$_T$ algorithm with $R_0 = 0.4$ and calibrated by the EM+JES scheme [146]. Jets are required to be high transverse momentum objects $p_T > 20$ GeV with positive energy and $|\eta| < 2.5$ (using pseudorapidity at EM scale).

In order to avoid double-counting of objects, jets overlapping with accepted electrons within $\Delta R < 0.2$ are removed.

5.4 Missing transverse energy

A precise measurement capability of the missing transverse energy ($E_{\mathrm{T}}^{\mathrm{miss}}$) is crucial for many analyses, including this one, since there are two neutrinos in the final state. Apart from the hard scattering processes of interest, where neutrinos are produced, many other source may generate additional $E_{\mathrm{T}}^{\mathrm{miss}}$. For instance underlying events, multiple interactions, pile-up and coherent electronics noise, lead to energy deposits and/or muon tracks, dead regions or readout channels. There are two algorithms for $E_{\mathrm{T}}^{\mathrm{miss}}$ reconstruction in ATLAS, the cell-based and object-based algorithms, that emphasize different aspects of energy classification and calibration [95].

The cell-based algorithm starts from the energy deposits in calorimeter cells that survive a noise suppression procedure. The cells can be calibrated using global calibration weights depending on their energy density. Corrections are applied for the muon energy and for the energy lost in the cryostat [95].

The object-based algorithm starts from the reconstructed, calibrated and classified objects in the event. For the analysis a `MET_RefFinal_em_tightewtm` object is used which is calculated from topological clusters calibrated at the EM scale and corrected according to the energy scale of the associated object. Muons, which are not primarily measured by the calorimeter, are included using their momentum measured from the track and muon spectrometer systems. The topological clusters are associated to electrons, photons, taus, high p_T jets ($p_T > 20$ GeV) and low p_T jets (SoftJets, 7 GeV $< p_T <$ 20 GeV). The ordering of these objects indicates the order of association of the clusters to the objects, where the clusters are associated with the first object used. The remaining clusters not associated with the high p_T objects are included at the EM scale in a so called `CellOut` term [147, 148].

The missing transverse energy is calculated using the following equations

$$E_{x,y}^{\mathrm{miss}} = E_{x,y}^{\mathrm{RefElec}} + E_{x,y}^{\mathrm{RefPhoton}} + E_{x,y}^{\mathrm{RefTau}} + E_{x,y}^{\mathrm{RefJet}} + E_{x,y}^{\mathrm{RefSoftJet}} + E_{x,y}^{\mathrm{RefMuon}} + E_{x,y}^{\mathrm{CellOut}} , \quad (5.14)$$

where

$$E_T^{\mathrm{miss}} = \sqrt{(E_x^{\mathrm{miss}})^2 + (E_y^{\mathrm{miss}})^2} . \quad (5.15)$$

There are data/MC discrepancies in the low $E_{\mathrm{T}}^{\mathrm{miss}}$ region coming from pile-up. These effects are observed in the `RefJet`, `RefSoftJet` and `CellOut` terms. For the `RefJet` term this effect is already included in the JES uncertainty. For the `RefSoftJet` and `CellOut` terms, 10.5% and 13.2% as systematic uncertainties are considered, respectively.

Chapter 6

Cut optimisation and event selection

The inclusive production cross section ratio of Z-boson to $t\bar{t}$ is very large. The predicted cross section of $t\bar{t}$ and Z-boson, at approximately NNLO in perturbative QCD in pp collisions at $\sqrt{s} = 7$ TeV, are 165 pb [22] and 989 pb [149, 150], respectively. This means 6 times more Z-bosons are produced at LHC than $t\bar{t}$. The kinematic characteristics of an event like $E_{\mathrm{T}}^{\mathrm{miss}}$ and invariant mass of two leptons are good handles for the separation of signal from Z-boson background.

In this chapter, first the performed multidimensional cut optimisation is presented and then the final event selection criteria.

6.1 Cut optimisation

Typically Z-boson events have small amounts of true $E_{\mathrm{T}}^{\mathrm{miss}}$, since there are no prompt neutrinos involved in Z-boson decay, and two leptons invariant mass (m_{ll}) distribution has a Breit-Wigner shape around the PDG value of the Z-boson pole mass 91.2 GeV [4]. With respect to Z-boson events, $t\bar{t}$ events in dilepton channel are characterized by a large $E_{\mathrm{T}}^{\mathrm{miss}}$, due to the presence of two neutrinos in the final state, and the invariant mass of two leptons has no peak.

A 3-D cut optimisation is performed, using $E_{\mathrm{T}}^{\mathrm{miss}}$, m_{ll}, and H_{T} as discriminant variables, for ee, $\mu\mu$, and $e\mu$ channels separately. The cut on m_{ll} is applied as a veto on events in a symmetric mass window around the Z-boson mass pole and referred to as the "Z mass window" cut. Here, H_{T} is defined as the scalar sum of transverse momenta of the two selected leptons and all selected jets in the event.

$$H_{\mathrm{T}} = \sum p_{\mathrm{T}}^{\mathrm{lep}} + \sum p_{\mathrm{T}}^{\mathrm{jet}} \,. \tag{6.1}$$

In Figure 6.1 $E_{\mathrm{T}}^{\mathrm{miss}}$, H_{T}, and m_{ll} distributions are shown applying all event selection requirements listed in Table 6.2, but relaxing the cuts on these variables. Since the ee and $\mu\mu$ channels have similar behaviour, their distributions are merged together. As Figure 6.1 (a) and (c) indicate the low $E_{\mathrm{T}}^{\mathrm{miss}}$ region ($0 < E_{\mathrm{T}}^{\mathrm{miss}} < 40$ GeV) is largely dominated by Drell-Yan events and those invariant mass distribution peaks at the Z-boson mass. However, as Figure 6.1 (e) shows, H_{T} is not a good discriminant variable for the event selection of the same flavor channels, since it does not help to suppress the contribution from $Z/\gamma^* \to ee$ an $Z/\gamma^* \to \mu\mu$, which are dominating in these channels.

Therefore, for ee and $\mu\mu$ channels, a 2-D grid optimization is performed for $E_{\mathrm{T}}^{\mathrm{miss}}$ and the Z mass window.

For the $e\mu$ channel, a 2-D grid optimization is performed as well, using $E_{\mathrm{T}}^{\mathrm{miss}}$ and H_{T} variables. m_{ll} is not considered for this channel, since the Z-boson does not decay to an electron and a muon directly. The way the Z-boson contributes to the $e\mu$ channel is mainly from the following decay process $Z/\gamma^* \to \tau\tau \to e\nu\nu\mu\nu\nu$. Due to the presence of neutrinos, the invariant mass distribution of the reconstructed electron and muon does not have Breit-Wigner structure around Z-boson mass pole, as we see from Figure 6.1 (f).

The cuts are optimised using MC simulated samples for highest significance, which includes statistical and systematic uncertainties in the definition:

$$\text{Significance} \quad = \quad \frac{N_{\mathrm{S}}}{\sqrt{N_{\mathrm{S}} + N_{\mathrm{B}} + \Sigma(\delta N^{i}_{\mathrm{B,stat}})^2 + \Sigma(\delta N^{i}_{\mathrm{syst}})^2}}\,, \tag{6.2}$$

where N_{S} and N_{B} are the expected number of signal and background events, respectively. In the denominator the $\delta N^{i}_{\mathrm{B,stat}}$ term is for the statistical uncertainty on the background prediction for each background i and is defined as

$$\delta N_{\mathrm{B,stat}} = \frac{\sqrt{N_{\mathrm{selected}}}}{N_{\mathrm{total}}} \times \sigma \times \mathcal{L}_{\mathrm{int.}}\,, \tag{6.3}$$

where N_{selected} is the number of events passing selection criteria, N_{total} is the number of events before selection, σ is the production cross section of the given process and $\mathcal{L}_{\mathrm{int.}}$ is the total integrated luminosity.

The systematic uncertainties $\delta N^{i}_{\mathrm{syst}}$ include all object related uncertainties, described in Chapter 9.

Optimization for the ee and $\mu\mu$ channels A 2-D grid optimisation is performed using $E_{\mathrm{T}}^{\mathrm{miss}}$ and the invariant mass of two leptons. Both channels have similar behavior and an optimum value of $E_{\mathrm{T}}^{\mathrm{miss}} > 40$ GeV is found, together with ± 10 GeV for the Z mass window, i.e. $|m_{(ll)} - m_Z| > 10$ GeV. The significance as a function of $E_{\mathrm{T}}^{\mathrm{miss}}$ versus the Z mass window is shown in Figure 6.2 (a) and (b) for ee and $\mu\mu$ channels respectively. Figure 6.2 middle row shows the projection of the significance as a function of $E_{\mathrm{T}}^{\mathrm{miss}}$ with the Z mass window cut fixed to its optimised value and the bottom row shows the projection of the significance as a function of Z the mass window with $E_{\mathrm{T}}^{\mathrm{miss}}$ cut also fixed to its optimised value. From the projected distributions, the optimal cut values where the significance is maximum can be seen better.

Optimization for the $e\mu$ channel For this channel, a 2-D grid optimisation is performed using the $E_{\mathrm{T}}^{\mathrm{miss}}$ and H_{T} variables. The highest significance is obtained at $H_{\mathrm{T}} > 130$ GeV. In Figure 6.3 (a), the significance as a function of H_{T} versus $E_{\mathrm{T}}^{\mathrm{miss}}$ is shown. As it can

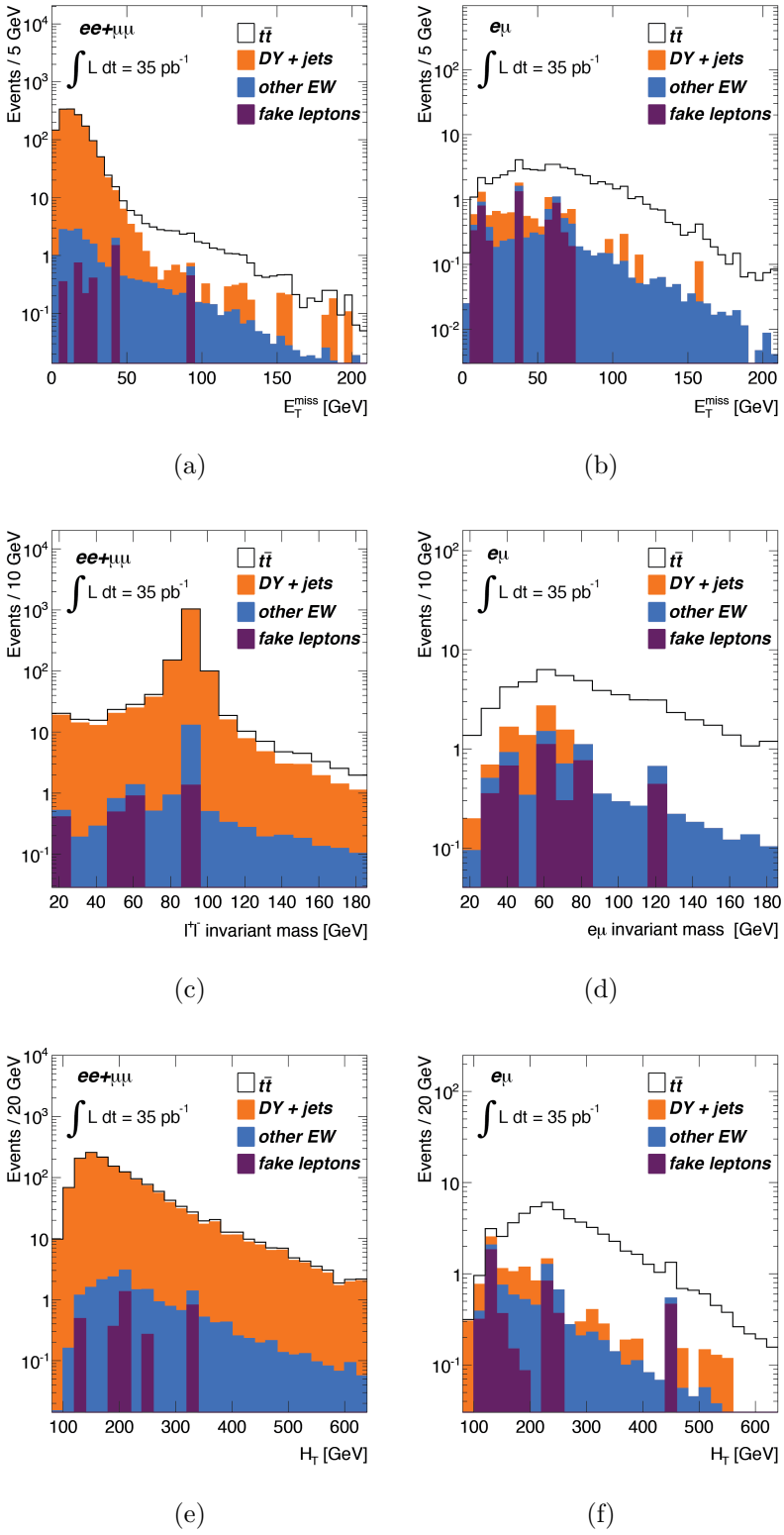

Figure 6.1 $ee + \mu\mu$ channels (left) and $e\mu$ channel (right): top row $E_{\mathrm{T}}^{\mathrm{miss}}$, middle row dilepton invariant mass and bottom row H_{T} distributions. All object and event selection (listed in the Table 6.2) requirements are applied, relaxing cuts on $E_{\mathrm{T}}^{\mathrm{miss}}$, dilepton invariant mass and H_{T}. Contributions from diboson and single top events are summarized as "other EW".

be seen from this distribution, the significance is slightly decreasing from no $E_{\mathrm{T}}^{\mathrm{miss}}$ cut to higher values. Therefore, we chose to keep this channel free from a $E_{\mathrm{T}}^{\mathrm{miss}}$ cut and avoid a dependence on the $E_{\mathrm{T}}^{\mathrm{miss}}$ scale systematic uncertainty. Figure 6.3 (b) shows the significance as a function of H_{T} where the distribution is almost flat up to 160 GeV, with a maximum at 130 GeV.

6.2 Event selection

The event selection criteria, with their descriptions, used for this analysis are listed below. The cut flow is summarised in Table 6.2.

- Trigger: We require events selected online by a single lepton trigger (e or μ). The electron trigger is required for the ee channel, the muon trigger is required for the $\mu\mu$ channel, and for the $e\mu$ channel, at least one of the triggers is required to be present. The detailed trigger requirements vary through the data-taking period, due to the rapidly increasing LHC luminosity and the commissioning of the trigger system, but with a threshold which is fully efficient for leptons satisfying $p_{\mathrm{T}} > 20$ GeV. Table 6.1 summarizes the trigger requirements during the different data periods for the electron and muon trigger. For electrons, a level-1 electromagnetic trigger object with a transverse energy threshold of 15 GeV is required. A more refined electromagnetic cluster selection is required in the level-2 trigger. Subsequently, a match between the selected calorimeter electromagnetic cluster and an inner detector track is imposed in the event filter. Muon candidates are selected by requiring a level-1 muon trigger, which are subsequently confirmed at level-2 and event filter by using the precision chambers of the muon spectrometer. In the later part of the data-taking period, the level-2 and event filter also required that the muon spectrometer track be matched to a track found in the inner detector in order to reduce the trigger rate in the face of increasing accelerator luminosity. The p_{T} threshold used by the event filter varied between 10 and 13 GeV.

Data period	Muon Trigger	Electron Trigger
E4-E7	EF_mu10_MSonly	EF_e15_medium
F	EF_mu10_MSonly	EF_e15_medium
G1-G5	EF_mu13	EF_e15_medium
G6	EF_mu13_tight	EF_e15_medium
H	EF_mu13_tight	EF_e15_medium
I	EF_mu13_tight	EF_e15_medium

Table 6.1 Trigger used for the different data periods and their luminosities, for MC EF_mu13_tight and EF_e15_medium were used.

  For MC, only the triggers EF_mu13_tight and EF_e15_medium were used. The difference in the trigger efficiencies between data and MC are taken into account by scale factors described in Chapter 5.

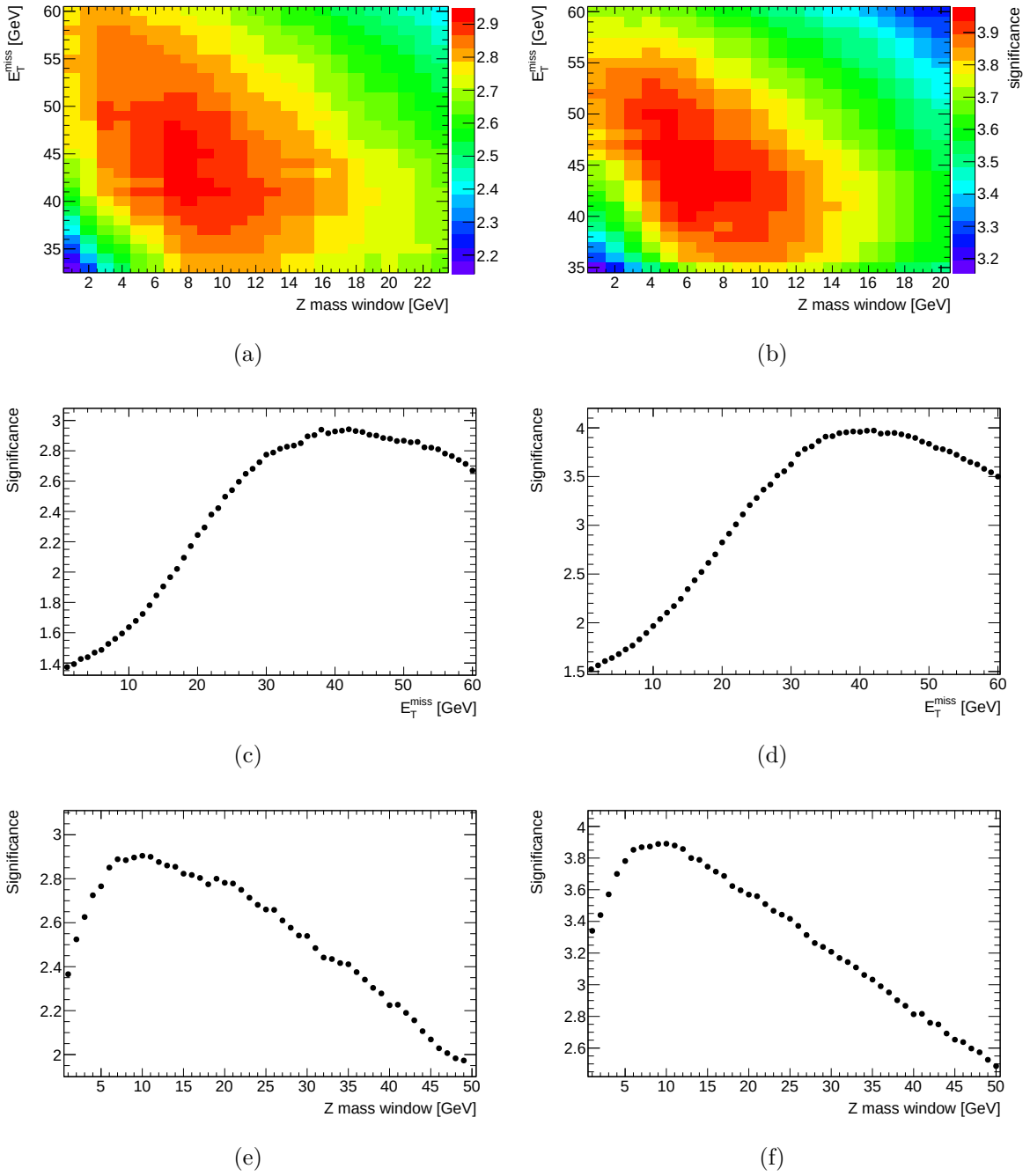

Figure 6.2 *ee* channel (left) and $\mu\mu$ channel (right): top row significance as a function of $E_{\mathrm{T}}^{\mathrm{miss}}$ versus the Z mass window, middle row projection of significance versus $E_{\mathrm{T}}^{\mathrm{miss}}$ when the Z mass window cut is applied to its optimised value, bottom row projection of significance versus Z mass window when $E_{\mathrm{T}}^{\mathrm{miss}}$ cut is applied to its optimised value.

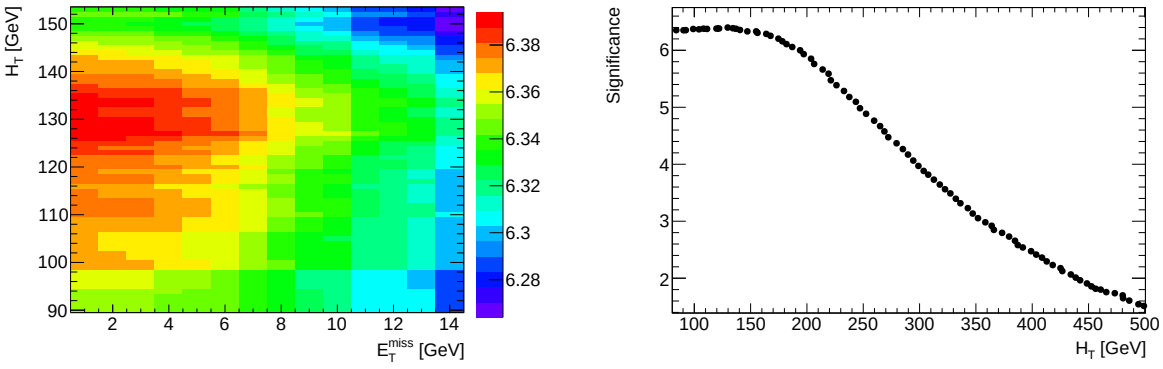

(a) (b)

Figure 6.3 $e\mu$ channel: (a) significance as a function of H_{T} versus $E_{\mathrm{T}}^{\mathrm{miss}}$, (b) projection of significance versus H_{T} when no $E_{\mathrm{T}}^{\mathrm{miss}}$ cut is applied.

- Bad jet cleaning: After the trigger selections, events are discarded if any jet with $p_T > 20$ GeV and positive energy fails jet quality cuts designed to reject jets arising from out-of-time activity or calorimeter noise. These are called `LooseBad` jets [151]. Jets failing the electron-jet overlap requirement and other selection criteria as described in Section 5.3 are not considered for the jet cleaning requirement.

- Non-collision background rejection: Events must have an offline-reconstructed primary vertex with at least five tracks.

- e and μ overlap removal: To avoid inconsistencies and double counting, events in which a selected electron and a muon, before being rejected by a jet overlap, share the same track, are not considered in the rest of the analysis.

- $E_{\mathrm{T}}^{\mathrm{miss}}$ and Z mass window: Events in the ee and $\mu\mu$ channels must satisfy $E_{\mathrm{T}}^{\mathrm{miss}} > 40$ GeV and $|m_{ll} - m_Z| > 10$ GeV requirements. Optimisation of these cuts is described in Section 6.1.

- H_{T}: Events in the $e\mu$ channel must satisfy $H_{\mathrm{T}} > 130$ GeV requirement; see Section 6.1.

- Jets requirement: Events must have at least two jets, no b-tagged jets are required.

- Leptons requirement: Exactly two oppositely-charged selected leptons (ee, $\mu\mu$, or $e\mu$). The lepton requirement criteria are divided into multiple steps in order to have a chance to see hints of new physics if it exists. As can be seen from Table 6.2, first the presence of at least two leptons in an event is checked. This provides a chance to study trilepton (or multilepton) events. The charge of leptons is checked after the requirement of exactly two leptons. In this case, we can look at the properties of events with same-sign leptons.

- Low mass region: The Z/γ^*+jets MC samples are generated with a phase space cuts on the invariant mass of two leptons $m_{ll} > 10$ GeV, see Section 4.3 Due to resolution effects, a cut on the reconstructed invariant dilepton mass of $m_{ll} > 15$ GeV is used on both MC and data events. At the same time, this removes contamination of the low-mass resonances (e.g. Υ or J/ψ).

- Trigger matching: To ensure that the event was actually triggered by the leptons used in the analysis, a match between one of the reconstructed leptons and the trigger object is required. The offline lepton and trigger object are required to be within $\Delta R < 0.15$.

- Truth matching: Important background contributions to the dilepton events are misidentified leptons (fakes) in the event. Event with misidentified leptons are also present in the MC samples, but they must be removed if data-driven background estimations for misidentified leptons are used. In MC, such an overlap is removed by requiring that the reconstructed leptons originate from a simulated leptonic W- or Z-boson decay (or subsequent tau decay). This can be checked with the `MCTruthClassifier` tool officially provided by the ATLAS Collaboration [152].

- MC truth: This cut is applied only for the $t\bar{t}$ sample for real dilepton event selection and for the acceptance calculation. On the generator level, we check the presence of two leptons (e or μ), which are originating from top quarks by following the complete decay chain. Events with $t \to Wb \to \tau\nu b \to l\nu\nu\nu b$ processes are considered as signal events as well.

In order to better understand the effect of each cut, Table 6.3, Table 6.4, and Table 6.5 are provided. They show the cut flow and the corresponding relative efficiencies (ε) for the ee, $\mu\mu$, and $e\mu$ channel selection, scaled to an integrated luminosity of 35 pb^{-1}. The relative efficiency is calculated as the ratio of the number of events passing a cut to the number of events before the cut. In the tables e and μ overlap cut is not included due to 100% efficiency almost everywhere.

We provide the cut flow for data, $t\bar{t}$ and MC modeled background samples. Numbers for other backgrounds, which are estimated from data ($Z/\gamma^* \to ee$, $Z/\gamma^* \to \mu\mu$ and mis-identified leptons), we provide in the next chapter.

As can be seen from the cut flow tables, the trigger selection is very efficient for signal events. The relative efficiency is $\sim$90% for all channels. At the same time, it is worth mentioning that trigger matching cut efficiency is $\sim$100% as well, which means almost all selected events were triggered by the selected leptons.

cut	ee	$\mu\mu$	$e\mu$
MC truth	only for $t\bar{t}$ sample: two truth leptons from t- and $\bar{t}$-quarks		
trigger (MC)	EF_e15_medium	EF_mu_13tight	EF_e15_medium or EF_mu_13tight
trigger (data)	see Table 6.1		
bad jet cleaning	reject events with bad jets		
nun coll. BG rejection	reject events with $N_{\mathrm{trk}} \leq 4$		
lepton req.	at least 2 leptons		
e and μ overlap	reject event, if e and μ share a track		
$E_{\mathrm{T}}^{\mathrm{miss}}$ or H_{T}	$E_{\mathrm{T}}^{\mathrm{miss}} > 40$ GeV		$H_{\mathrm{T}} > 130$ GeV
jet req.	at least 2 jets		
lepton req.	exactly 2 leptons		
sign req.	opposite signed leptons		
low-mass req.	$m_{ll} > 15$ GeV		
Z mass window	$\lvert m_{ll} - m_Z \rvert > 10$ GeV		
trigger matching	match lepton trigger $\Delta R < 0.15$		
truth matching	match reconstructed lepton to truth lepton from W or Z		

Table 6.2 List of cuts that is used for the Table 6.3, Table 6.4 and Table 6.4. e and μ overlap cut is not included in the tables, since its efficiency is 100% for most of the cases.

	Data		$t\bar{t}$		single top		diboson		$Z/\gamma^* \to \tau\tau$	
cut	events	ε%	events	ε%	events	ε%	events	ε%	events	ε%
before cuts	2×10^7	-	3×10^3	-	1×10^3	-	4×10^4	-	251.3	-
MC truth	-	-	96.4	3.2	-	-	-	-	-	-
trigger	7×10^6	34.6	87.1	91.4	314.7	23.9	3×10^3	7.5	106.3	42.3
bad jet cleaning	7×10^6	99.9	87.1	100.0	314.7	100.0	3×10^3	100.0	106.3	100.0
non coll. BG reject	7×10^6	100.0	87.1	100.0	314.6	100.0	3×10^3	99.9	106.2	99.9
$N_l \geq 2$	7×10^3	0.1	20.3	23.3	2.2	0.7	14.3	0.5	13.3	12.6
$E_{\mathrm{T}}^{\mathrm{miss}} > 40$ GeV	58	0.8	15.3	75.3	1.5	70.2	0.9	6.1	4.2	31.2
$N_{\mathrm{jet}} \geq 2$	24	41.4	13.4	88.0	0.8	50.7	0.4	42.3	1.2	29.4
$N_l = 2$	24	100.0	13.3	99.8	0.8	100.0	0.4	100.0	1.1	91.4
OS req	23	95.8	13.3	99.3	0.8	97.6	0.4	100.0	1.0	90.7
$m_{ll} > 15$ GeV	22	95.7	13.2	99.3	0.8	99.5	0.4	100.0	1.0	99.9
Z mass window	17	77.3	11.1	84.6	0.7	86.8	0.4	100.0	0.5	50.8
trigger matching	17	100.0	11.1	100.0	0.7	100.0	0.4	100.0	0.5	100.0
truth matching	17	100.0	10.9	98.3	0.6	95.6	0.4	100.0	0.5	97.3

Table 6.3 Cut flow table with number of selected events and relative efficiencies for *ee* channel selection for an integrated luminosity of 35 pb^{-1}. The relative efficiency ε, the ratio of the number of events passing a cut to the number of events before the cut, is also shown. The "MC truth" cut is applied only for the $t\bar{t}$ sample, it checks the existence of two truth leptons originating from t- and $\bar{t}$-quarks in the event.

	Data		$t\bar{t}$		single top		diboson		$Z/\gamma^* \to \tau\tau$	
cut	events	ε%	events	ε%	events	ε%	events	ε%	events	ε%
before cuts	1×10^7	-	3×10^3	-	1×10^3	-	4×10^4	-	250.5	-
MC truth	-	-	95.0	3.1	-	-	-	-	-	-
trigger	4×10^6	38.3	83.7	88.2	319.8	24.3	3×10^3	8.0	99.9	39.9
bad jet cleaning	4×10^6	99.9	83.7	100.0	319.8	100.0	3×10^3	100.0	99.9	100.0
non coll. BG reject	4×10^6	97.2	83.7	100.0	319.7	100.0	3×10^3	99.9	99.9	99.9
$N_l \geq 2$	1×10^4	0.3	34.9	41.7	4.0	1.3	34.2	1.1	23.9	24.0
$E_{\mathrm{T}}^{\mathrm{miss}} > 40$ GeV	69	0.5	26.6	76.2	3.0	73.4	2.2	6.5	8.0	33.2
$N_{\mathrm{jet}} \geq 2$	45	65.2	23.2	87.3	1.5	49.8	1.2	54.6	2.0	25.1
$N_l = 2$	44	97.8	23.2	99.9	1.5	100.0	1.2	100.0	1.8	92.2
OS req	44	100.0	23.2	100.0	1.5	99.6	1.2	100.0	1.7	93.5
$m_{ll} > 15$ GeV	43	97.7	23.1	99.6	1.5	99.3	1.2	100.0	1.7	99.6
Z mass window	30	69.8	19.4	84.1	1.2	84.7	1.2	100.0	0.9	51.2
trigger matching	30	100.0	19.4	99.8	1.2	100.0	1.2	100.0	0.9	100.0
truth matching	30	100.0	19.4	100.0	1.2	99.8	1.2	100.0	0.9	100.0

Table 6.4 Cut flow table with number of selected events and relative efficiencies for $\mu\mu$ channel selection for an integrated luminosity of 35 pb^{-1}. The relative efficiency ε, the ratio of the number of events passing a cut to the number of events before the cut, is also shown. The "MC truth" cut is applied only for the $t\bar{t}$ sample, it checks the existence of two truth leptons originating from t- and $\bar{t}$-quarks in the event.

	Data		$t\bar{t}$		single top		diboson		$Z/\gamma^* \to \tau\tau$	
cut	events	ε%	events	ε%	events	ε%	events	ε%	events	ε%
before cuts	1×10^7	-	3×10^3	-	611.2	-	6×10^3	-	182.5	-
MC truth	-	-	188.8	6.2	-	-	-	-	-	-
trigger	1×10^7	36.0	170.7	90.4	611.2	100.0	6×10^3	100.0	182.5	100.0
bad jet cleaning	1×10^7	99.9	170.7	100.0	611.2	100.0	6×10^3	100.0	182.5	100.0
non coll. BG reject	1×10^7	98.9	170.7	100.0	611.1	100.0	6×10^3	99.9	182.3	99.9
$N_l \geq 2$	160	0.0	53.3	31.2	5.4	0.9	39.5	0.7	14.9	8.2
$H_{\mathrm{T}} > 130$ GeV	70	43.8	52.2	96.0	4.5	83.4	4.5	11.3	6.8	45.9
$N_{\mathrm{jet}} \geq 2$	60	85.7	46.1	90.2	2.5	56.6	3.1	70.0	2.8	40.4
$N_l = 2$	60	100.0	46.1	100.0	2.5	100.0	3.1	100.0	2.5	89.0
OS req	57	95.0	45.8	99.4	2.5	97.9	3.1	100.0	2.1	83.7
$m_{ll} > 15$ GeV	57	100.0	45.8	100.0	2.5	100.0	3.1	100.0	2.1	100.0
trigger matching	57	100.0	45.8	100.0	2.5	100.0	3.1	100.0	2.1	100.0
truth matching	57	100.0	45.7	99.8	2.4	97.8	3.0	97.2	2.0	99.1

Table 6.5 Cut flow table with number of selected events and relative efficiencies for $e\mu$ channel selection for an integrated luminosity of 35 pb^{-1}. The relative efficiency ε, the ratio of the number of events passing a cut to the number of events before the cut, is also shown. The "MC truth" cut is applied only for the $t\bar{t}$ sample, it checks the existence of two truth leptons originating from t- and $\bar{t}$-quarks in the event.

Chapter 7

Background determination

Several processes can mimic the $t\bar{t}$ dilepton signal by producing a similar signature in the detector, i.e. two leptons, $E_{\mathrm{T}}^{\mathrm{miss}}$, and two and more jet. There are three categories of background sources:

- The background from Drell-Yan processes ($Z/\gamma^* \to ll$) produced with associated jets and with large $E_{\mathrm{T}}^{\mathrm{miss}}$, due to resolution effects and measurement errors. $Z/\gamma^* \to ll$ (here $\ell = e, \mu$) is the main background source for the same-flavor lepton channels (i.e. ee and $\mu\mu$ channels), while $Z/\gamma^* \to \tau\tau$ is the main background source for the $e\mu$ channel.

- Processes that contain hadrons misidentified as leptons or non-prompt leptons (i.e. leptons that do not originate from W-boson decay). Both the misidentified hadrons and the non-prompt leptons are referred to as "fake leptons", or "fakes".

  Fakes enter the sample in events with W-boson produced in association with jets, and QCD multi-jet events. For instance in W+jets, $t\bar{t}$ in single lepton channel or t-channel single top events one lepton can be real (from the W-boson decay), and the second is a fake lepton produced by one of the jets. In the case of QCD multi-jet events, both leptons must be fakes in order to contribute as background.

  Fakes are an important background in the ee and $e\mu$ channels, but relatively small in $\mu\mu$ channel, since there are more sources for electron misidentification (jets, photons, Dalitz decays, heavy flavor decays) than for muons (mainly heavy flavor decays).

- Other background sources are electroweak processes including two leptons in the decay, such as single top and diboson (WW, ZZ, and WZ) production processes.

The background contribution is evaluated using data whenever possible in order to minimize the reliance on MC simulations. The Drell-Yan and fake lepton backgrounds are determined using data. $Z/\gamma^* \to \tau\tau$ and the backgrounds from electroweak processes are evaluated purely from MC simulation.

7.1 Data-driven backgrounds

A data-driven approach is preferred to be used for background estimation since it is difficult in MC simulation to predict instrumental effects and backgrounds involving the

tails of distributions. Data-driven procedures for estimation of backgrounds from Drell-Yan and mis-identified leptons are described in the following two subsections.

7.1.1 Drell-Yan background

The event selection described in Section 6.2 includes cuts to reject Drell-Yan (DY) background, dominating in ee and $\mu\mu$ channels. Requiring large $E_{\mathrm{T}}^{\mathrm{miss}}$ and the dilepton invariant mass to be outside of the Z mass window significantly reduces this background, but does not completely eliminate it. The Drell-Yan events in the tail of the $E_{\mathrm{T}}^{\mathrm{miss}}$ distribution and away from the Z mass peak still pass event selection criteria.

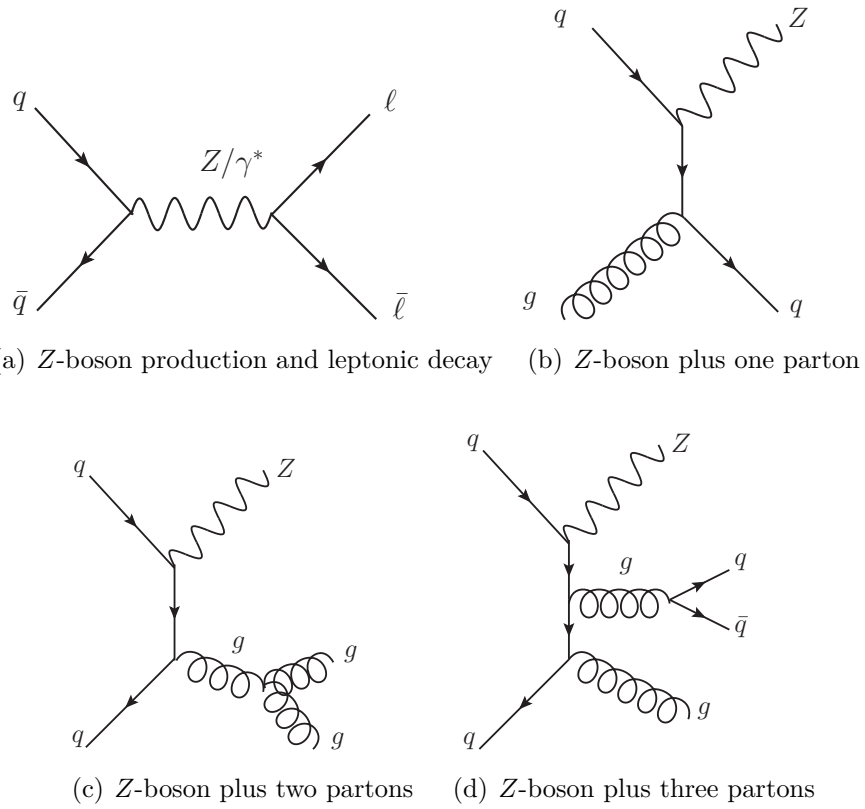

(a) Z-boson production and leptonic decay (b) Z-boson plus one parton

(c) Z-boson plus two partons (d) Z-boson plus three partons

Figure 7.1 Examples of Feynman diagrams for Z-boson production and decay.

Due to large theoretical uncertainties regarding the Z-boson production cross-section in association with high jet multiplicities (see Section 9.3), as well as the difficulty of modelling the non-Gaussian nature of missing transverse momentum distribution tails in the simulation, a direct calculation of this background from MC is not feasible for analysis.

The Feynman diagrams of the Z/γ^*-boson production and decay process is shown in Figure 7.1 (a). Some examples for Z-boson production in association with jets are shown in Figure 7.1 (b) - (d).

In order to estimate the contribution of Drell-Yan background in the ee and $\mu\mu$ channels, the $E_{\mathrm{T}}^{\mathrm{miss}}$ versus dilepton invariant mass plane is divided into regions that are expected to be dominated by signal (referred to as signal region) or by the Drell-Yan background (referred to as control region).

The division of the events can be seen in Figure 7.2. The bins contain different physical processes. For instance, bins A and C are dominated by $t\bar{t}$ events and the admixture of $Z/\gamma^* \to ee$ and $Z/\gamma^* \to \mu\mu$ events needs to be estimated there, whereas Drell-Yan events fall largely in bin H. The contents in the bins G, I, B, and H are measured in data, and they are dominated by Drell-Yan events. Bins D, E and F are excluded to avoid correlation between $E_{\mathrm{T}}^{\mathrm{miss}}$ and dilepton invariant mass.

In order to have a data sample that contains only Drell-Yan events, the contaminations from other non-Drell-Yan processes are subtracted from data yields in each bin relying on the MC prediction.

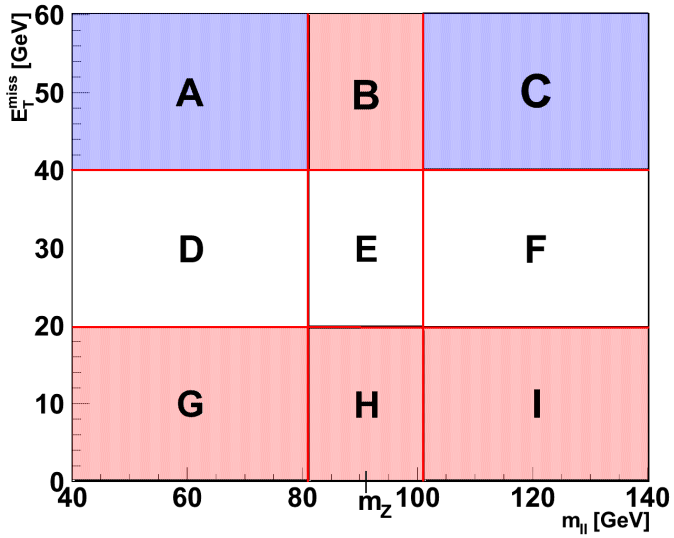

Figure 7.2 Diagram of $E_{\mathrm{T}}^{\mathrm{miss}}$ versus dilepton invariant mass (m_{ll}) with labelled areas for Drell-Yan data-driven background estimates using the "ABCD" method. Regions A and C are the signal region, dominated by $t\bar{t}$ with ≥ 2 jets.

Using the formulae in Equation 7.1 and Equation 7.2, the amount of Drell-Yan background in the signal regions is estimated by scaling the data to MC in signal and control regions.

$$A_{\mathrm{DY}} = G_{\mathrm{data}} \left(\frac{A_{\mathrm{MC}}}{G_{\mathrm{MC}}}\right) \left(\frac{H_{\mathrm{MC}}}{B_{\mathrm{MC}}}\right) \left(\frac{B_{\mathrm{data}}}{H_{\mathrm{data}}}\right) , \tag{7.1}$$

$$C_{\mathrm{DY}} = I_{\mathrm{data}} \left(\frac{C_{\mathrm{MC}}}{I_{\mathrm{MC}}}\right) \left(\frac{H_{\mathrm{MC}}}{B_{\mathrm{MC}}}\right) \left(\frac{B_{\mathrm{data}}}{H_{\mathrm{data}}}\right) , \tag{7.2}$$

where $A - I$ denote the number of events in the corresponding bins of Figure 7.2 and the subscript MC or data denote the number of Z events in MC and data (subtracting non-Drell-Yan components), respectively.

The total Drell-Yan estimate is then:

$$\text{Drell}-\text{Yan background estimates} = A_{\text{DY}} + C_{\text{DY}} \,. \tag{7.3}$$

For the 35 pb^{-1} data sample used for this analysis, the method described above turned out to be not applicable due to the lack of statistics in the bin B. This affects mainly the ee channel, since electrons are selected using tight criteria (see Section 5.1.6). In bin B, there are only 5 selected events, which cause a large statistical uncertainty with resulting large systematic fluctuations.

Therefore, a slightly different approach is used simplifying this method by changing the grid bands in Figure 7.2 for control regions. In this approach, the Z mass window columns are left unchanged, but the control region is formed by events with an invariant dilepton mass inside the Z mass window and with $E_{\text{T}}^{\text{miss}} > 30$ GeV, see Figure 7.3. With this approach, there are 19 ee selected events in bin B. The $E_{\text{T}}^{\text{miss}}$ cut is obtained using the same cut optimisation method described in Chapter 6.

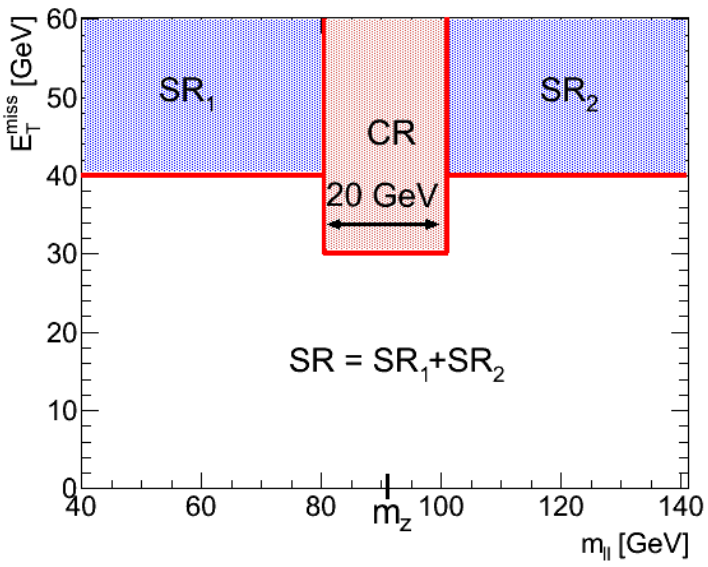

Figure 7.3 Diagram of $E_{\text{T}}^{\text{miss}}$ versus dilepton invariant mass (m_{ll}) for Drell-Yan data-driven background estimates using a simplified version of the "ABCD" method. Regions SR_1 and SR_2 are the signal regions, dominated by $t\bar{t}$ with ≥ 2 jets.

Here, a scale factor is derived using Drell-Yan simulations to extrapolate from the control region into the signal region:

$$\text{Drell}-\text{Yan background estimates} = \frac{\text{MC}_{\text{DY}}(\text{SR})}{\text{MC}_{\text{DY}}(\text{CR})} \times (\text{data}(\text{CR}) - \text{MC}_{\text{other}}(\text{CR}))\,, \tag{7.4}$$

where $MC_{DY}(SR)$ and $MC_{DY}(CR)$ represent the number of events in the signal and control region, respectively. MC_{other} is the number of events from other processes that contaminate the control region. data(CR) represents the observed number of events in the control region in 35 pb^{-1} of collision data. The observed and expected numbers in the control and signal region are summarized in Table 7.1 for the ee and $\mu\mu$ channels.

		DY sources		other sources (CR)					
channel	data(CR)	MC(CR)	MC(SR)	$t\bar{t}$	$Z\tau\tau$	W	diboson	single top	total
ee	19	31.0	2.2	2.3	0.0	0.0	1.0	0.1	3.5
$\mu\mu$	60	45.3	2.9	4.1	0.0	0.0	1.6	0.2	6.0

Table 7.1 Number of observed events in data in the control region (data(CR)), the number of MC events in the signal (MC(R)) and control (MC(CR)) regions and the number of events from other sources contaminating the control region.

The number of Drell-Yan background events, with statistical and systematic uncertainties, derived from the described is compared to MC expectation in Table 7.2 for the ee and $\mu\mu$ channel, respectively.

The uncertainties on this estimate are shown in Table 7.3. The systematic uncertainty of the method is tested by varying the $E_{\mathrm{T}}^{\mathrm{miss}}$ cut in the control region by ± 5 GeV. The other uncertainties include the statistical uncertainty of data and MC (data stat., MC stat.) and systematic uncertainties such as the jet energy scale, resolution, and efficiency (JES, JER, JEF), on the lepton identification and trigger scale factor (ID SF, Trig. SF), the lepton energy scale and resolution (ES, ER), on the theoretical cross section for MC backgrounds (MC cross section) and the uncertainty due to pile-up (Pile-up). Details concerning systematic uncertainties and their evaluation are provided in the Chapter 9.

The comparison of the uncertainties between the data-driven method and the MC prediction shows that they are larger on the MC prediction. The uncertainties, except for the statistical uncertainties for the data-driven method, largely cancel out in the ratio between the MC signal and control region in Equation 7.4. The statistical uncertainties are similar in size, and despite the additional statistical uncertainty from the number of selected data events, the total uncertainty is smaller for the data-driven method.

	ee	$\mu\mu$
DD	1.1 ± 0.5	3.5 ± 1.4
MC	$2.2^{+1.3}_{-1.0}$	$2.9^{+1.8}_{-1.6}$

Table 7.2 Estimates of the contamination from Drell-Yan processes in the signal region of the $t\bar{t}$ analysis from both the data-driven (DD) method and from MC simulations.

Uncertainty(%)	ee (DD)	ee (MC)	$\mu\mu$ (DD)	$\mu\mu$ (MC)
Luminosity	±0.8	±3.4	±0.4	±3.4
Data stat	+35.1/-27.9	-	+16.3/-14.3	-
JES	-1.3/+12.8	+42.7/-21.8	-5.5/+16.7	+26.8/-0.7
JER	±0.5	±5.6	±12.4	±34.5
JEF	±0.7	±0.0	±0.2	±0.0
$E_{\mathrm{T}}^{\mathrm{miss}}$ CellOut	+3.0/+0.3	+4.2/+0.2	-5.2/+2.4	-5.9/+6.2
El ID SF	$\pm - 1.6$	±7.6	±0.0	±0.0
El Trig SF	±0.0	±0.0	±0.0	±0.0
Mu ID SF	±0.0	±0.0	±0.1	±1.4
Mu Trig SF	±0.0	±0.0	±0.0	+0.3/-0.3
MC cross section	-3.8/+6.4	±30.0	+2.5/-5.3	±35.1
MC stat	±20.3	±19.5	±16.7	±16.1
Pile-up	±0.3	±14.7	±5.2	±6.9
El ES	+8.6/+1.2	+4.9/+0.4	+0.2/+0.1	+0.0/+0.1
El ER	+1.0/+10.1	+0.2/+9.3	±0.0	±0.0
Mu ES	±0.0	±0.0	+4.0/-5.7	+3.1/-5.3
Mu ER (MS)	±0.0	±0.0	+9.7/-4.7	+9.3/-6.6
Mu ER (ID)	±0.0	±0.0	+2.6/-5.9	+3.3/-6.1
Method	±34.6	-	±19.2	-
total (syst + lumi + stat)	±51.1	+59.6/-45.5	+37.9/-34.8	+60.1/-53.7

Table 7.3 Uncertainties on the predicted number of Drell-Yan events in the signal region. The uncertainties are compared between the data-driven (DD) determination and the determination from MC simulations. The uncertainty due to the method is evaluated from the variation of the prediction when the $E_{\mathrm{T}}^{\mathrm{miss}}$ cut in the control region is varied by ±5 GeV. The uncertainties of the prediction are presented as $+1\sigma/-1\sigma$ variation of the systematic source.

7.1.2 Mis-identified leptons

True $t\bar{t}$ dilepton events contain two leptons from the two W-boson decays. The background comes predominantly from W+jets events and single lepton $t\bar{t}$ production with a real and a fake lepton, though there is a smaller contribution with two fake leptons coming from QCD multi-jet production. For muons the dominant fake lepton mechanism is a semi-leptonic decay of a heavy-flavor hadron, where a muon survives the isolation requirement. In the case of electrons, the three mechanisms are heavy flavor decay, light flavor jets, and conversion of photons.

A method called "matrix method" is used [153, 154] to estimate the fraction of the dilepton sample that contains fake leptons. The basic idea of the method is to define two sets for loose (L) and tight (T) selections and estimate the mis-identification probability (f) of a loose fake (F) lepton to pass tight selection and the real efficiency (r) for real (R) loose lepton to be reconstructed as tight. From the loose and tight definitions, the

number of observed dilepton events with zero, one or two tight leptons together with two, one or zero loose leptons, respectively (N_{LL}, N_{TL}, N_{LT}, N_{TT}), can be counted. The loose and tight definitions are provided later in this chapter. N_{TL} is different from N_{LT} since leptons are ordered by highest transverse momentum, which means in N_{TL} the tight lepton has higher transverse momentum than loose lepton and the opposite for N_{LT}.

The ensemble with tight leptons is a subset of the loose leptons, and r and f probabilities are defined as:

$$r = \frac{N_R^T}{N_R^L} \qquad f = \frac{N_F^T}{N_F^L} \tag{7.5}$$

Using r and f, linear expressions can be obtained for the observed yields as a function of the number of events with zero, one, and two real leptons together with two, one, and zero fake leptons, respectively (N_{FF}, N_{FR}, and N_{RF}, N_{RR}, respectively). These linear expressions form a matrix can be inverted in order to extract the real and fake content of the observed dilepton event sample.

$$\begin{bmatrix} N_{TT} \\ N_{TL} \\ N_{LT} \\ N_{LL} \end{bmatrix} = \mathbf{M} \begin{bmatrix} N_{RR} \\ N_{RF} \\ N_{FR} \\ N_{FF} \end{bmatrix} \tag{7.6}$$

$$\mathbf{M} = \begin{bmatrix} r_1 r_2 & r_1 f_2 & f_1 r_2 & f_1 f_2 \\ r_1 (1 - r_2) & r_1 (1 - f_2) & f_1 (1 - r_2) & f_1 (1 - f_2) \\ (1 - r_1) r_2 & (1 - r_1) f_2 & (1 - f_1) r_2 & (1 - f_1) f_2 \\ (1 - r_1)(1 - r_2) & (1 - r_1)(1 - f_2) & (1 - f_1)(1 - r_2) & (1 - f_1)(1 - f_2) \end{bmatrix} \tag{7.7}$$

The N_{LL}, N_{LT}, and N_{TL} and N_{TT} events contain exactly two leptons. They are not subsets of each other, which means there is no double counting of objects.

The matrix (7.7) can be inverted to solve for the unknown real and fake lepton events:

$$\begin{bmatrix} N_{RR} \\ N_{RF} \\ N_{FR} \\ N_{FF} \end{bmatrix} = \mathbf{M}^{-1} \begin{bmatrix} N_{TT} \\ N_{TL} \\ N_{LT} \\ N_{LL} \end{bmatrix} \tag{7.8}$$

$$\mathbf{M}^{-1} = \frac{1}{(r_1 - f_1)(r_2 - f_2)} \begin{bmatrix} (1 - f_1)(1 - f_2) & (f_1 - 1) f_2 & f_1 (f_2 - 1) & f_1 f_2 \\ (f_1 - 1)(1 - r_2) & (1 - f_1) r_2 & f_1 (1 - r_2) & -f_1 r_2 \\ (r_1 - 1)(1 - f_2) & (1 - r_1) f_2 & r_1 (1 - f_2) & -r_1 f_2 \\ (1 - r_1)(1 - r_2) & (r_1 - 1) r_2 & r_1 (r_2 - 1) & r_1 r_2 \end{bmatrix} \tag{7.9}$$

The inverse matrix in (7.9) solves for the expected number of fake events in the loose signal sample. Changing the definition to tight selection according to (7.5) and summing up the fake lepton contribution gives:

$$\begin{aligned} N_f &= r_1 f_2 N_{RF} + f_1 r_2 N_{FR} + f_1 f_2 N_{FF} \qquad (7.10) \\ &= \alpha r_1 f_2 \left[(f_1 - 1)(1 - r_2) N_{TT} + (1 - f_1) r_2 N_{TL} + f_1 (1 - r_2) N_{LT} - f_1 r_2 N_{LL} \right] \\ &\quad + \alpha f_1 r_2 \left[(r_1 - 1)(1 - f_2) N_{TT} + (1 - r_1) f_2 N_{TL} + r_1 (1 - f_2) N_{LT} - r_1 f_2 N_{LL} \right] \\ &\quad + \alpha f_1 f_2 \left[(1 - r_1)(1 - r_2) N_{TT} + (r_1 - 1) r_2 N_{TL} + r_1 (r_2 - 1) N_{LT} + r_1 r_2 N_{LL} \right] \end{aligned}$$

where

$$\alpha = \frac{1}{(r_1 - f_1)(r_2 - f_2)}.$$

The relation (7.10) is exact in a statistical sense as long as f and r are correctly estimated. If f is defined to be very loose with respect to r ($f \simeq O(1\%)$), then terms quadratic in f can be neglected. A further approximation is to neglect N_{LL}. This results in the following approximation valid for small f's

$$N_f \simeq \left[\frac{f_1(r_1 - 1)}{r_1} + \frac{f_2(r_2 - 1)}{r_2} \right] N_{TT} + f_2 N_{TL} + f_1 N_{LT}. \qquad (7.11)$$

The tight criteria are always the lepton definitions used in the analysis, see Chapter 5. The loose lepton selection is chosen such that it is kinematically similar to the tight lepton selection, but some cuts are relaxed.

The loose lepton selection criteria are:

- Loose muons are defined in the same way as tight muons, except that the calorimeter and track isolation requirements are not applied.
- Loose electrons must fulfil the tight electron cuts, except for the "tight" ID cut, which is replaced by the "medium" plus b-layer hit requirement. The isolation requirement is loosened from 4 GeV to $6 + 0.3 \times p_T$ GeV.

The fake and tight lepton efficiencies are measured directly from the same lepton trigger stream as the final data selection and using the same integrated luminosity.

The real efficiency is estimated using tag-and-probe where tight and loose pairs are selected within the Z mass window as a function of p_{T} and η. Background is subtracted using same-sign dilepton events. Both loose leptons are exposed to the same tight criteria test. The measured efficiencies are shown in Figures 7.4-7.5 [153].

The mis-identification probabilities are measured in a control region defined as $E_{\mathrm{T}}^{\mathrm{miss}} < 10(20)$ GeV for muons (electrons), where the selection is exactly one loose lepton, and at least one jet with the requirement $\Delta R(\mathrm{jet}, \mathrm{lepton}) > 0.7$.

The dominant systematic uncertainty on the fake lepton background estimation, as determined by the matrix method, is from the possible difference in the mixture of

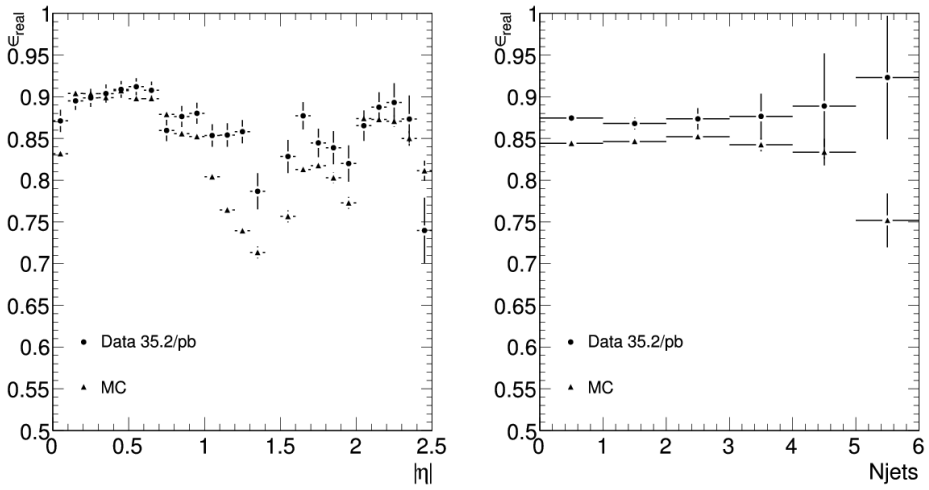

(a) Efficiency vs. η (b) Efficiency vs. number of jets

Figure 7.4 Reconstruction efficiency for loose electrons [153].

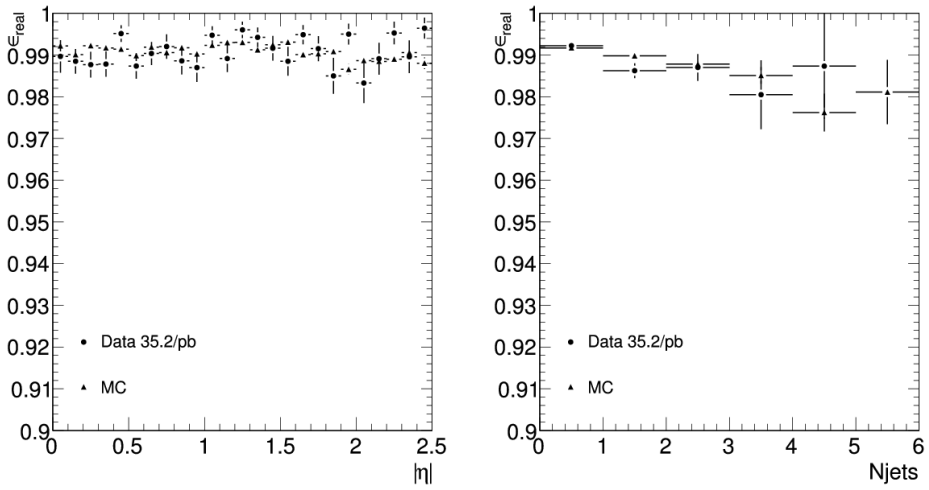

(a) Efficiency vs. η (b) Efficiency vs. number of jets

Figure 7.5 Reconstruction efficiency for loose muons [153].

processes where the efficiency for fake leptons f is measured (dijet events) and where it is applied (the signal region). A larger contribution is expected from heavy flavor events in the signal region due to $t\bar{t} \to \ell\nu bjjb$ events. This effect is accounted for by measuring the dependence of the efficiency for fake leptons on the heavy-flavor fraction and calculating a corrected efficiency for fake leptons based on the expected heavy-flavor fraction in the signal region in simulation studies.

The results of the matrix method for the fake lepton background with statistical and systematic uncertainties are summarised in Table 7.4 for 0,1 and ≥ 2 jet bins.

N_{jets}	ee	$\mu\mu$	$e\mu$
0	$1.6 \pm 0.8 \pm 0.8$	$0.5 \pm 0.5 \pm 0.3$	$0.0 \pm 0.7 \pm 0.4$
1	$0.6 \pm 0.5 \pm 0.6$	$0.0 \pm 0.5 \pm 0.2$	$1.1 \pm 0.9 \pm 0.3$
≥ 2	$1.0 \pm 0.7 \pm 0.6$	$0.4 \pm 0.4 \pm 0.3$	$1.9 \pm 1.5 \pm 0.7$

Table 7.4 Overview of the estimated fake lepton background yields in the signal ($N_{\text{jets}} \geq 2$) and control regions using the matrix method for each sub-channel. Statistical and systematic uncertainties are shown as well.

7.2 Other MC simulated background

The contributions from other electroweak background processes such as single top, dibosons and $Z/\gamma^* \to \tau\tau$ are estimated directly from the MC.

The Feynman diagrams for the single top and diboson productions are shown in Figure 2.7 and Figure 7.6, respectively. $Z/\gamma^* \to \tau\tau$ cannot be derived using Equation 7.4 because the neutrinos from the τ decay preclude a straightforward reconstruction of the Z peak. Therefore, this background is evaluated using MC as well.

The contribution from single top, dibosons, and $Z/\gamma^* \to \tau\tau$ backgrounds are estimated using their theoretical cross sections. The calculated number of expected background events from a process is given by:

$$N_{\text{expected}} = \mathcal{L}_{\text{int.}} \times \sigma \times \frac{N_{\text{selected}}}{N_{\text{total}}}, \tag{7.12}$$

where acceptance $A = \frac{N_{\text{selected}}}{N_{\text{total}}}$ is a ratio of events which pass selection criteria and $\mathcal{L}_{\text{int.}}$ is the total integrated luminosity used for the analysis 35 pb^{-1}.

The full set of systematic uncertainties are included for the MC simulated backgrounds (JES, JER, etc.), as well as the uncertainty on the theoretical production cross sections, see Chapter 9. Event yields together with statistical and systematic uncertainties for these background sources can be found in Table 9.2, Table 9.4, and Table 9.6. The

largest uncertainty for these backgrounds is from the uncertainty on their production cross sections.

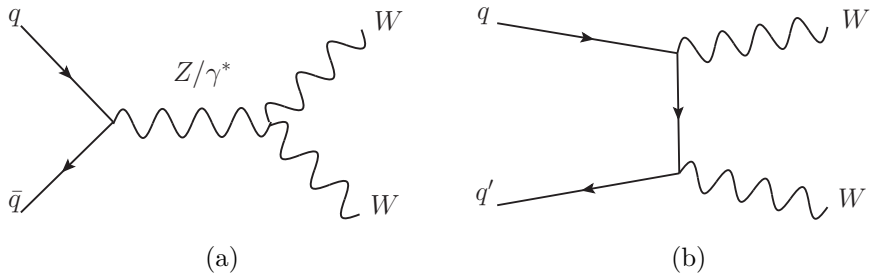

Figure 7.6 Examples of Feynman diagrams for WW pair production. ZZ and WZ pairs can be produced similarly.

Chapter 8

Cut and count analysis

8.1 Counting method

The production cross section of $t\bar{t}$ is extracted by using a counting method, which is based on the following formula:

$$\sigma = \frac{N_{\text{obs}} - N_{\text{bkg}}}{A \times \varepsilon \times \mathcal{L}_{\text{int.}}}, \tag{8.1}$$

where N_{obs} is the number of observed events from data, N_{bkg} is the number of expected background events. In the denominator, A is the geometrical acceptance of the selection, ε is the selection efficiency for signal, and $\mathcal{L}_{\text{int.}}$ is the integrated luminosity. Experimental uncertainties are $\Delta\sigma_{\text{stat.}}$, $\Delta\sigma_{\text{syst.}}$ and $\Delta\sigma_{\mathcal{L}}$, which represent statistical, systematic and luminosity uncertainties correspondingly.

The number of observed events is obtained from the selection of a candidate sample from the data. The number of expected background events is either calculated from MC simulations or estimated with data-driven methods in order to reduce the dependence on the simulation or on theoretical uncertainties of the background cross sections. The geometrical acceptance A is taken from MC simulations of the detector. The efficiency ε contains the selection efficiency of signal events, which includes trigger and lepton reconstruction and identification efficiencies.

8.2 Control regions

The modeled acceptances and efficiencies are validated by comparing MC simulations with data in control regions which are depleted of $t\bar{t}$ events, but have similar kinematics. In general, a good agreement between the background model and the data is observed.

Same-flavor control sample

The Z mass window, defined as $|m_{ll} - m_Z| < 10$ GeV, and low $E_{\text{T}}^{\text{miss}}$ region, defined as $E_{\text{T}}^{\text{miss}} < 40$ GeV, are used for the same-flavor control sample consideration. These are the kinematic regions, which are expected to be largely dominated by $Z \to ee$ and $Z \to \mu\mu$ events. All other event selection criteria, listed in Section 6.2, are used. Figure 8.1 (a) and (b) show $E_{\text{T}}^{\text{miss}}$ for events with the dilepton invariant mass inside the Z mass window

and examine the jet energy scale and resolution. Figure 8.1 (c) and (d) show the jet multiplicity for events where the dilepton invariant mass lies inside the Z mass window and low $E_{\mathrm{T}}^{\mathrm{miss}}$ region. The agreement in the jet multiplicity plots shows that there is no problem in the modeling with ISR/FSR and Drell-Yan processes. Finally, Figure 8.1 (e) and (f) show the dilepton invariant mass distribution in the low $E_{\mathrm{T}}^{\mathrm{miss}}$ region and probe the lepton energy scale and resolution.

"Same-sign" control sample

The understanding of conversions can be tested by using same-sign events. Additional control regions are events passing event selection requirements, but instead of having two opposite-sign leptons we require to have same-sign lepton pairs.

There are three observed events in the $e\mu$ channel. Figure 8.2 shows the invariant mass distribution of an electron and a muon same-sign pairs and the jet multiplicity distribution in $e\mu$ channel. As distributions indicate the observed three events match with expectations, where there are three expected events from data-driven fake estimation and 0.4 events from diboson simulation in ≥ 2 jets signal region. The total uncertainty on the expectation is approximately 100% as shown in the plot. There are no observed same-sign events with ≥ 2 jets and dilepton invariant mass outside Z mass window for ee and $\mu\mu$ channels. Figure 8.3 shows the same distributions for ee channel. There is one observed event in the dielectron invariant mass distribution, which is lying inside the Z mass window, and two events in the jet multiplicity distribution, which are in the 1 jet bin. Similar plots for $\mu\mu$ channel are not provided since there are no observed events anywhere.

$e\mu$ control sample

The probability that tau leptons decay to an electron or a muon, with correspondingly flavored neutrinos, is $\sim$17.5% [4] and some of their momentum is carried off by neutrinos, so the $Z \to \tau\tau$ process lacks the large and easily identifiable peak in the dilepton invariant mass distribution.

However, a signature can be found in which $Z \to \tau\tau$ is the largest contribution, which allows us to check its normalization and kinematics. After the selection of $e\mu$ channel events, with exactly zero jets, there is no contribution from $Z \to ee$ and $Z \to \mu\mu$, making the $Z \to \tau\tau \to e\mu\nu\nu\nu\nu$ visible, see Figure 8.4.

8.3 Signal region and event yields

Observed $t\bar{t}$ candidate event yields

The expected and measured numbers of events in the signal region after applying all selection cuts, as described in Chapter 6, for each of the individual dilepton channels are shown in Table 8.1. In a data set of 35 pb^{-1} a total of 104 candidate events are observed, 17 in the ee-channel, 30 in the $\mu\mu$-channel and 57 in the $e\mu$-channel. The number of

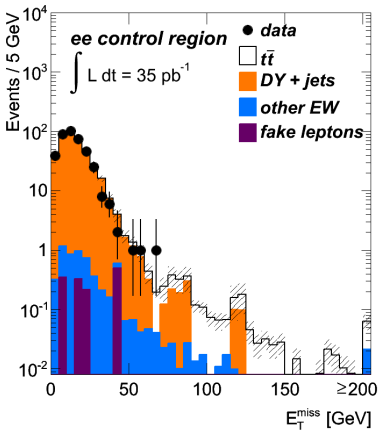

(a) $E_{\mathrm{T}}^{\mathrm{miss}}$ (ee)

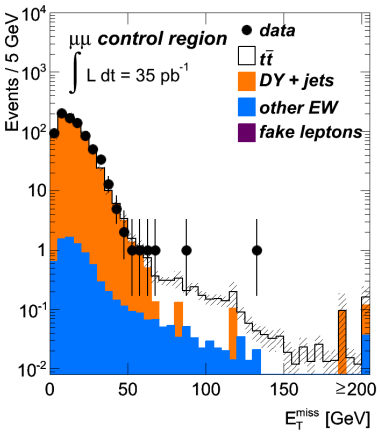

(b) $E_{\mathrm{T}}^{\mathrm{miss}}$ $(\mu\mu)$

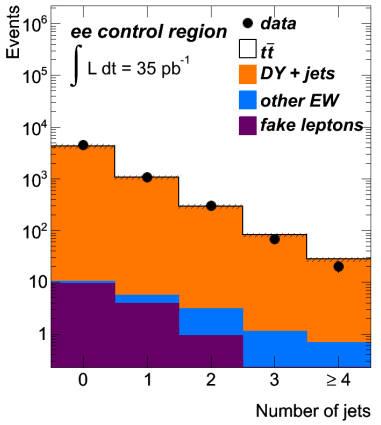

(c) N_{jets} (ee)

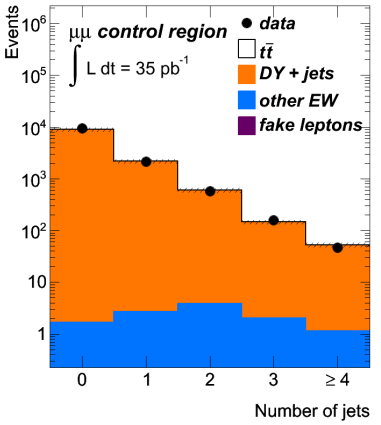

(d) N_{jets} $(\mu\mu)$

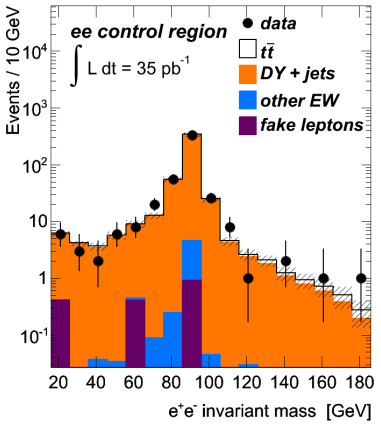

(e) OS mass (ee)

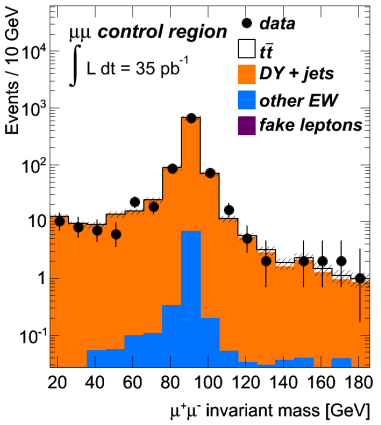

(f) OS mass $(\mu\mu)$

Figure 8.1 Top row $E_{\mathrm{T}}^{\mathrm{miss}}$ in events with a dilepton mass inside the Z mass window, middle row the number of jets in events with a dilepton mass inside the Z mass window and $E_{\mathrm{T}}^{\mathrm{miss}} < 40$ GeV, bottom row the invariant mass in events with $E_{\mathrm{T}}^{\mathrm{miss}} < 40$ GeV. Contributions from diboson and single top events are summarized as "other EW". The uncertainty on the data points are statistical uncertainties only, whereas the uncertainty bands include statistical and systematic uncertainties.

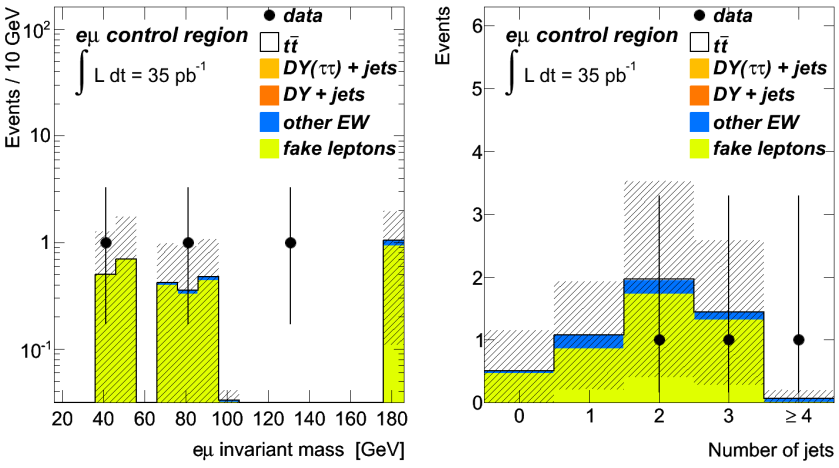

(a) (b)

Figure 8.2 Invariant mass of same-sign $e\mu$ pairs and jet multiplicity distribution. Contributions from diboson and single top events are summarized as "other EW". The uncertainty on the data points are statistical uncertainties only, whereas the uncertainty bands include statistical and systematic uncertainties.

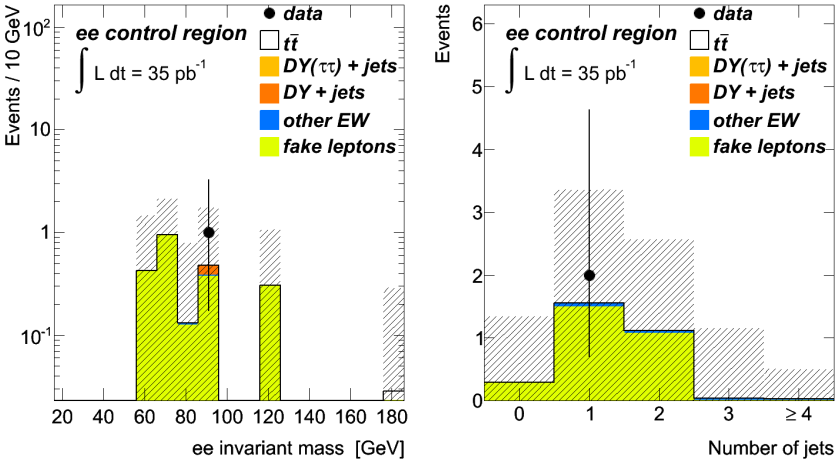

(a) (b)

Figure 8.3 Invariant mass of same-sign ee and $\mu\mu$ pairs and jet multiplicity distribution. Contributions from diboson and single top events are summarized as "other EW". The uncertainty on the data points are statistical uncertainties only, whereas the uncertainty bands include statistical and systematic uncertainties.

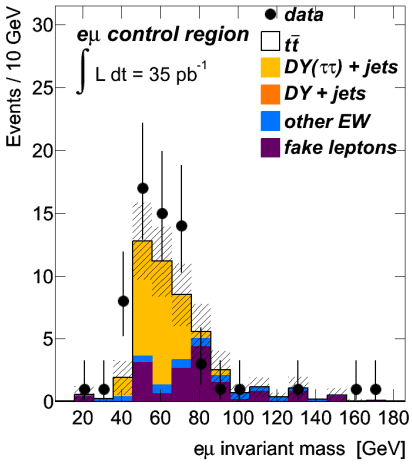

Figure 8.4 Data and backgrounds in the $e\mu$ channel with exactly zero reconstructed jets, where $Z \to \tau\tau$ is the largest expected source. Contributions from diboson and single top events are summarized as "other EW". The uncertainty on the data points are statistical uncertainties only, whereas the uncertainty bands include statistical and systematic uncertainties.

total expected events is 98.9 ± 5.3, where the $Z(\to ee, \mu\mu)$+jets (see Section 7.1.1) and fake lepton (see Section 7.1.2) backgrounds are extracted from data. The rest of the backgrounds, as well as the signal, are estimated from simulation. Details with cut flow of selected events and relative ε can be found in the Table 6.3, Table 6.4, and Table 6.5 for ee, $\mu\mu$ and $e\mu$ channels, respectively.

The estimation shows that almost 80% of observed events are $t\bar{t}$ events, and in all channels the Z+jets events are the largest background. The estimated signal region acceptances are $11.5 \pm 1.2\%$ (ee), $20.5 \pm 1.3\%$ ($\mu\mu$), and $24.2 \pm 1.5\%$ ($e\mu$).

From Figure 8.5 to Figure 8.8, kinematic distributions of selected events, with the expectation of 35 pb^{-1}, are shown, where in each of the plots, the selection has been relaxed to omit the cut on the shown observable. In Figure 8.5 and Figure 8.6, the number of selected jets and b-tagged jets are shown for ee, $\mu\mu$, and $e\mu$ channels. In Figure 8.7 the same distributions are shown for three dilepton channels combined together. From the number of jets distributions, it can be seen that for the required multiplicity of at least two jets, the selection is dominated by the signal, whereas for lower jet multiplicities background dominates. In these distributions, jets are considered b-tagged, if the secondary vertex-based tagger SV0 [155] returns a value above a threshold that is defined by a 50% tagging efficiency, obtained from studies of simulated $t\bar{t}$ events [156]. b-tagged jet multiplicity distributions show that a majority of the selected events have at least one b-tagged jet and are consistent with the hypothesis that the excess of events over the estimated background originates from $t\bar{t}$ decay.

The variables $E_{\mathrm{T}}^{\mathrm{miss}}$ for the same-flavor channels and H_{T} for the $e\mu$ channel are shown in Figure 8.8, and again, as it can be seen the selection is dominated by signal above cut values.

	ee	$\mu\mu$	$e\mu$
Z+jets (DD)	1.1 ± 0.5	3.5 ± 1.4	-
$Z(\rightarrow \tau\tau)$+jets (MC)	0.4 ± 0.3	1.2 ± 0.6	3.0 ± 1.3
Mis-identified lep. (DD)	1.0 ± 0.9	0.4 ± 0.5	1.9 ± 1.7
Single top (MC)	0.6 ± 0.1	1.2 ± 0.2	2.4 ± 0.3
Dibosons (MC)	0.5 ± 0.1	0.9 ± 0.1	2.0 ± 0.3
Total (non $t\bar{t}$)	3.6 ± 1.2	7.2 ± 1.6	9.4 ± 2.5
$t\bar{t}$ (MC)	10.9 ± 1.2	19.4 ± 1.5	45.7 ± 3.7
Total expected events	14.5 ± 1.7	26.6 ± 2.1	55.1 ± 4.4
Observed events	17	30	57

Table 8.1 The full breakdown of the expected $t\bar{t}$-signal and background in the signal region compared to the observed event yields, for each of the dilepton channels (MC is simulation based, DD is data-driven). All systematic uncertainties are included and the correlation between the different background sources are taken into account.

Kinematic properties of selected events

From the measured missing transverse energy, and the transverse momenta of the leptons and jets, the so-called stransverse mass m_{T2} is constructed for each selected event [157]. It is defined as

$$m_{T2}^2 = \min_{\not{p}_T^{(1)}+\not{p}_T^{(2)}=E_{\mathrm{T}}^{\mathrm{miss}}} \left[\max\left\{ m_T^2\left(p^{(1)},\not{p}^{(1)}\right), m_T^2\left(p^{(2)},\not{p}^{(2)}\right) \right\} \right]$$

$$m_T^2\left(p^{(n)},\not{p}^{(n)}\right) = m_{(n)}^2 + \not{m}^2 + 2\left(E_T^{(n)}\not{E}_T - \vec{p}_T^{(n)}\cdot\vec{\not{p}}_T\right)$$

where:

- $p^{(n)}$ is the four-momentum of the visible particle
- $\vec{p}_T^{(n)}$ is the transverse momentum of the visible particle
- $\not{p}^{(n)}$ is the four-momentum of the invisible particle
- $\vec{\not{p}}_T^{(n)}$ is the trial transverse momentum of the invisible particle
- (n) indicates from which parent particle the particle is coming

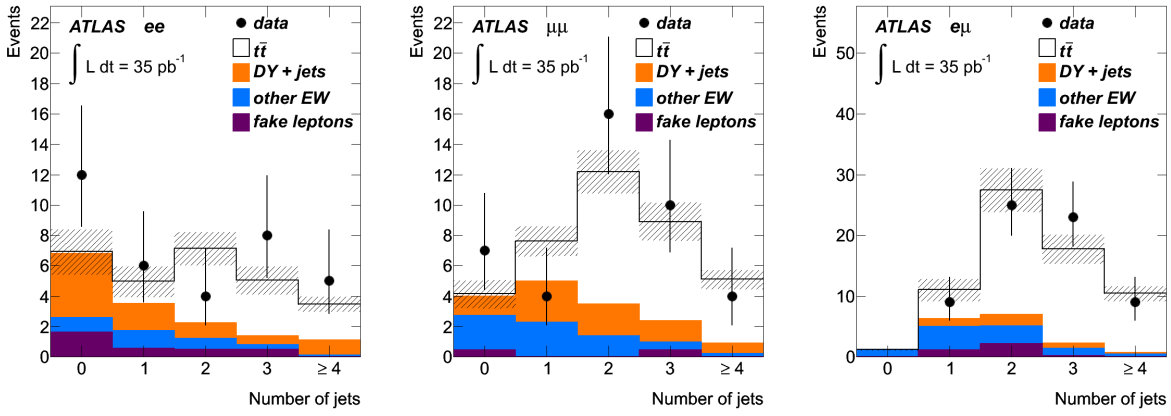

(a) (b) (c)

Figure 8.5 Jet multiplicities for the signal region omitting the $N_{\text{jets}} \geq 2$ requirement in (a) the ee channel, (b) the $\mu\mu$ channel and (c) the $e\mu$ channel. Contributions from diboson and single top events are summarized as "other EW". The uncertainty on the data points are statistical uncertainties only, whereas the uncertainty bands include statistical and systematic uncertainties.

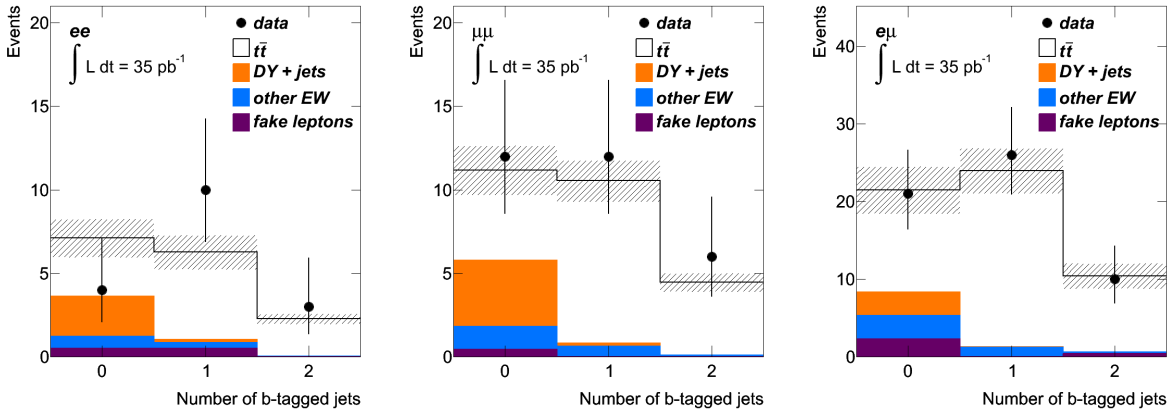

(a) (b) (c)

Figure 8.6 b-tagged jet multiplicities for the signal region in (a) the ee channel, (b) the $\mu\mu$ channel and (c) the $e\mu$ channel. Contributions from diboson and single top events are summarized as "other EW". The uncertainty on the data points are statistical uncertainties only, whereas the uncertainty bands include statistical and systematic uncertainties.

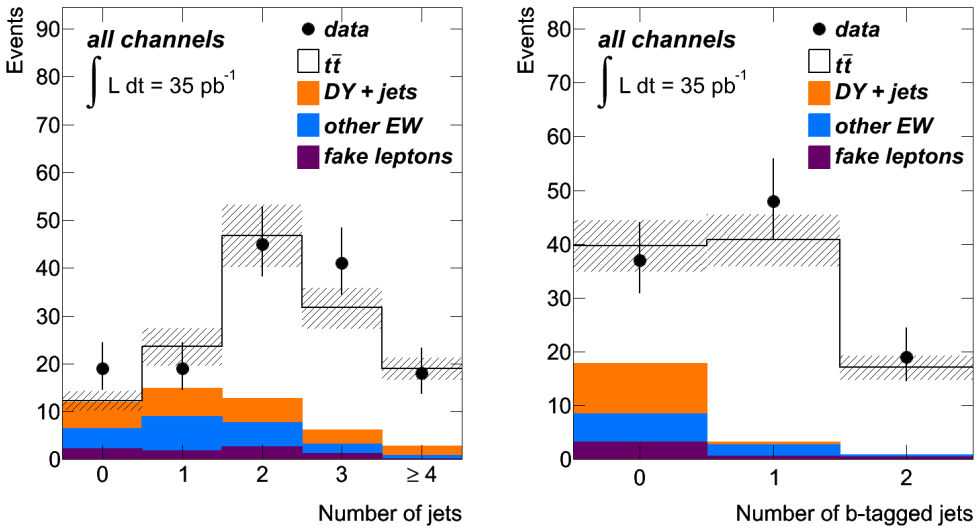

(a) (b)

Figure 8.7 (a) Jet multiplicity in the signal region without the $N_{\text{jets}} \geq 2$ requirement and (b) the b-tagged jet multiplicity in the signal region, both for the combined dilepton channels. Contributions from diboson and single top events are summarized as "other EW". The uncertainty on the data points are statistical uncertainties only, whereas the uncertainty bands include statistical and systematic uncertainties.

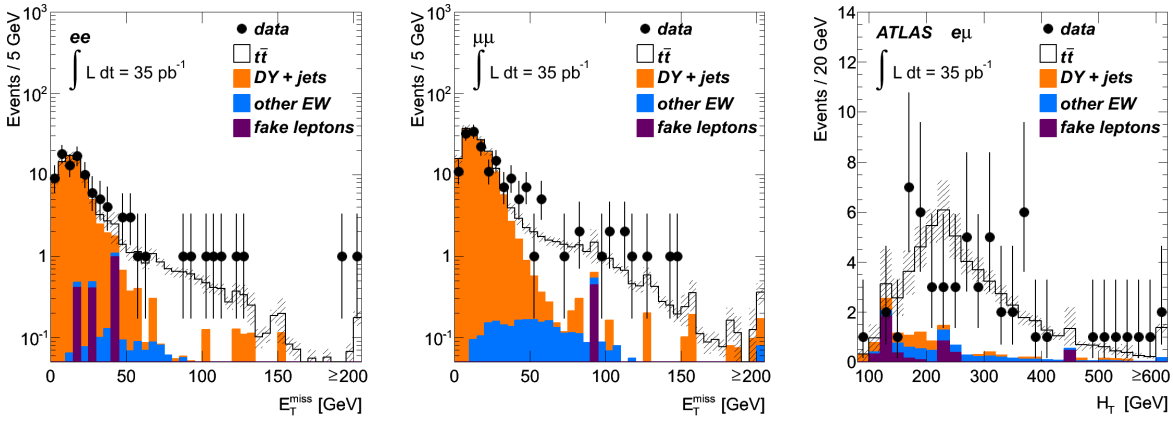

(a) (b) (c)

Figure 8.8 The $E_{\text{T}}^{\text{miss}}$ distribution in the signal region for (a) the ee channel and for (b) the $\mu\mu$ channel without the $E_{\text{T}}^{\text{miss}} > 40$ GeV requirement, and (c) the distribution of the H_{T}, defined as the scalar sum of the transverse energies of the two leptons and all selected jets, in the signal region without the $H_{\text{T}} > 130$ GeV requirement. Contributions from diboson and single top events are summarized as "other EW". The uncertainty on the data points are statistical uncertainties only, whereas the uncertainty bands include statistical and systematic uncertainties.

	ee	$\mu\mu$	$e\mu$
Z+jets (DD)	1.1 ± 0.5	3.5 ± 1.4	-
$Z(\rightarrow \tau\tau)$+jets (MC)	0.4 ± 0.3	1.2 ± 0.6	3.0 ± 1.3
Non-Z leptons (DD)	1.0 ± 0.9	0.4 ± 0.5	1.9 ± 1.7
Single top (MC)	0.6 ± 0.1	1.2 ± 0.2	2.4 ± 0.3
Dibosons (MC)	0.5 ± 0.1	0.9 ± 0.1	2.0 ± 0.3
Total (non $t\bar{t}$)	3.6 ± 1.2	7.2 ± 1.6	9.4 ± 2.5
$t\bar{t}$ (MC)	10.9 ± 1.2	19.4 ± 1.5	45.7 ± 3.7
Total expected events	14.5 ± 1.7	26.6 ± 2.1	55.1 ± 4.4
Observed events	17	30	57

Table 8.2 The full breakdown of the expected $t\bar{t}$-signal and background in the signal region compared to the observed event yields, for each of the dilepton channels (MC is simulation based, DD is data-driven). All systematic uncertainties are included and the correlation between the different background sources are taken into account.

The minimization uses trial momenta for the neutrinos which only have to satisfy the measured $E_{\mathrm{T}}^{\mathrm{miss}}$. From the two possible combinations of leptons and highest-p_{T} jets the combination with the smallest m_{T2} is chosen.

The distribution shown in Figure 8.9 is consistent with the hypothesis of a pair-produced heavy particle with mass around $170 - 175$ GeV that decays in final states with invisible particles.

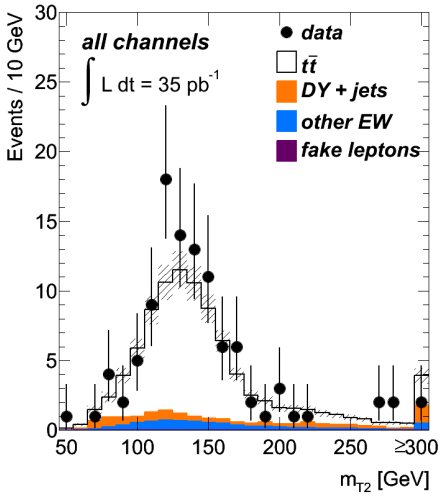

Figure 8.9 The m_{T2} distributions for events that pass the selection criteria for selected data events in the three dilepton channels overlayed over the expected distribution from MC simulation from signal and background events. Contributions from diboson and single top events are summarized as "other EW". The uncertainty on the data points are statistical uncertainties only, whereas the uncertainty bands include statistical and systematic uncertainties.

Chapter 9

Systematic uncertainties

Systematic uncertainties arise from uncertainties associated with the nature of the measurement apparatus, assumptions made by the experimenter, or the model used to make inferences based on the observed data. Common examples of systematic uncertainty include uncertainties that arise from the calibration of the measurement device, the probability for the detection of a given type of interaction (acceptance), and parameters of the model used to make inferences that themselves are not precisely known [158].

In Equation 8.1, used for the cross section measurement, we quote the luminosity uncertainty ($\Delta\sigma_{\mathcal{L}}$) separately from other systematic uncertainties, which are included in the $\Delta\sigma_{\text{syst}}$ term. In the $\Delta\sigma_{\text{syst}}$ term uncertainties associated with the jet energy scale, the resolution and efficiency, lepton reconstruction, identification and trigger scale factors, lepton energy scale and resolution, $E_{\text{T}}^{\text{miss}}$, theoretical cross sections for MC simulated backgrounds, data-driven background estimations, pile-up and $t\bar{t}$ production modelling are included. Each systematic uncertainty is described below, closely following prescriptions developed by the ATLAS top physics working group [159].

The impact of systematic uncertainties are estimated by redoing the full analysis chain after each variation and comparing with the nominal analysis.

$$\frac{\Delta\sigma}{\sigma} = \frac{\sigma_{\text{variated}} - \sigma_{\text{nominal}}}{\sigma_{\text{nominal}}}\,, \tag{9.1}$$

The largest uncertainties are the jet energy scale uncertainty and the theoretical cross sections for MC simulated backgrounds. Channels with electrons have large contributions from the uncertainty on the background with fake leptons and on the electron identification efficiency. The MC modeling of the parton shower, the ISR/FSR and the limited statistics of background MC in the same lepton channels also contribute to the total uncertainty.

The results with statistical and systematic uncertainties are summarized in Table 9.1, Table 9.3, and Table 9.5 for ee, $\mu\mu$, and $e\mu$ channels, respectively. The uncertainties for the backgrounds estimated with MC simulations are shown in Table 9.2, Table 9.4, and Table 9.6. In the tables quoted "total" uncertainty includes quadratically added all uncertainties. The cross section is calculated for each channel using the selected data events and the estimated acceptance. The total systematic uncertainty is smaller than the statistical uncertainty.

9.1 Luminosity

As mentioned in Chapter 4 for this analysis 35 pb^{-1} data sample is used taken under stable pp beam conditions during the 2010 LHC run at $\sqrt{s} = 7$ TeV. The luminosity measurement has a relative uncertainty of 3.4% [160].

9.1.1 Pile-up

The simulation includes effects from pile-up by overlaying randomly minimum bias events to achieve a certain average number of vertices. Pile-up effects result in additional energy deposits that affect not only the jet reconstruction, but also the $E_{\mathrm{T}}^{\mathrm{miss}}$ in an event, which is an important discrimination variable for the analysis.

Figure 9.1 shows the number of reconstructed vertices in events with an invariant dilepton mass around the Z-boson mass. The vertices are required to have more than 4 tracks and must be identified as a primary or pile-up vertex [154]. It can be seen that in both ee and $\mu\mu$ channels, the MC has pile-up events with a higher average number of vertices.

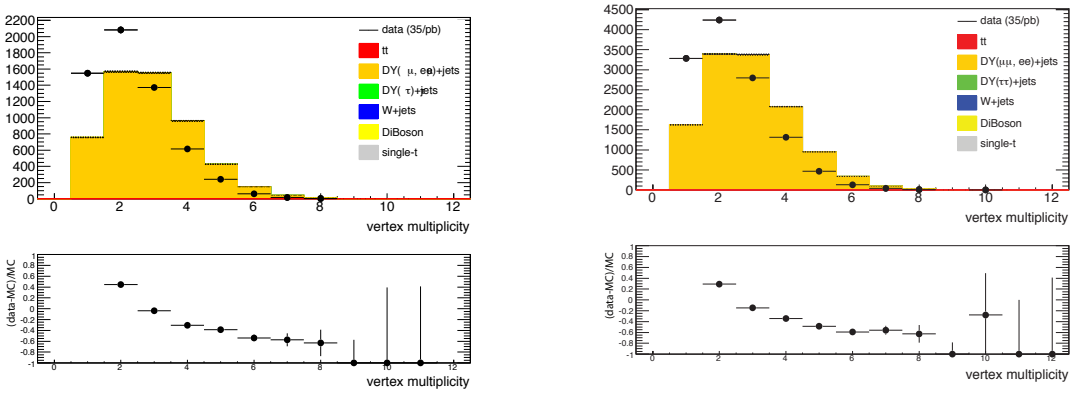

Figure 9.1 Number of reconstructed vertices with more than 4 tracks and selected as primary or pile-up vertices in the ee channel (left) and the $\mu\mu$ channel (right) in the Z-boson enhanced region [154].

A reweighting method according to the number of vertices in the event has been adopted for MC events. The weights are consistent between ee and $\mu\mu$ events. The effect of the reweighting can be seen in Figure 9.2.

A comparison of $E_{\mathrm{T}}^{\mathrm{miss}}$ of events, within the Z mass window and with at least 2 jets, shows that the agreement between data and MC is nevertheless good, as it can be seen in Figure 9.3, regardless of the reweighting. A similar behaviour has been seen for $\mu\mu$ events. Hence, the samples are used are not reweighted and the change of the analysis with pile-up reweighting can the used as a systematic uncertainty.

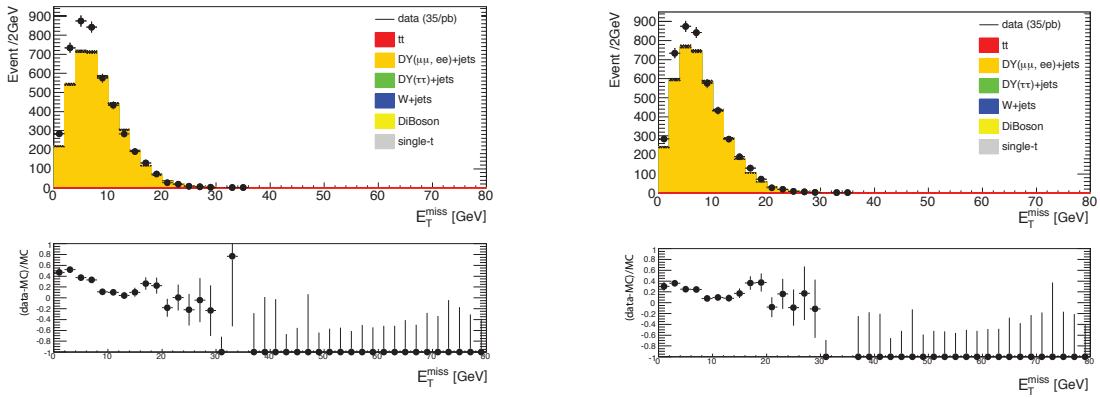

Figure 9.2 $E_{\mathrm{T}}^{\mathrm{miss}}$distribution for $Z \to ee$ enhanced events and 0-jets before (left) and after (right) reweighting [154].

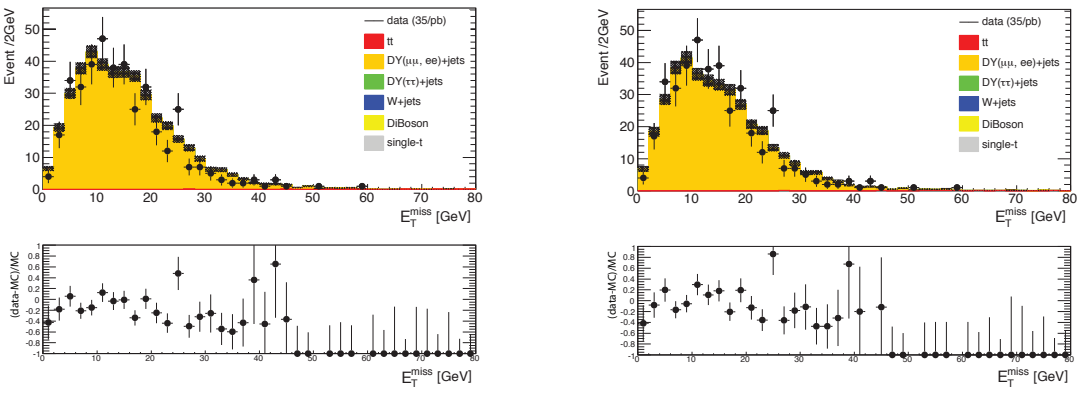

Figure 9.3 $E_{\mathrm{T}}^{\mathrm{miss}}$distribution for $Z \to ee$ enhanced events with 2 or more jets before (left) and after (right) reweighting in the ee channel [154].

9.2 Systematics on data-driven backgrounds

9.2.1 Data-driven Drell-Yan estimation

The uncertainty due to the data-driven method used for Drell-Yan background estimation is tested by varying the $E_{\mathrm{T}}^{\mathrm{miss}}$ cut in the control region is varied by ± 5 GeV, see Section 7.1.1.

9.2.2 Mis-identified leptons

Uncertainty from the fake background estimate [153] is derived from the difference in the observed and predicted number of fake events in control regions, defined as opposite sign events with zero or one jet without H_{T} cut or same sign events with more than one jet. The matrix method used for fake background estimations is described in Section 7.1.2 and the systematic uncertainties on the estimation are provided in Table 7.4.

9.3 Theoretical cross section

For Z/γ^*+jets background events, the normalization uncertainty is modelled by separately considering events with a given jet multiplicity. While the cross section in the 0-jet multiplicity sample has 4% uncertainty, the extrapolation to each following jet multiplicity increases the uncertainty by an additional 24% [161].

Overall, normalization uncertainties on the backgrounds from single top quark and diboson production are 10 % [162, 163] and 5 % [164, 149], respectively.

9.4 Jets

9.4.1 Jet energy scale (JES)

The jet energy scale and its uncertainty was discussed in Section 5.3. JES uncertainty has been derived combining information from test-beam data, LHC collision data and simulation [165] and varies as a function of jet p_T and η. As it was discussed, JES includes several terms. To account for effects from nearby jets, a conservative approach is used by adding an additional 5% term to the jet energy scale uncertainty if a jet with $p_{\mathrm{T}} > 10$ GeV is found in the vicinity of $\Delta R < 0.6$.

The `MultijetJESUncertaintyProvider` tool [145, 166], provided by the ATLAS collaboration, was used to access specific uncertainty values. JES uncertainty value is used to vary the jet energy by $\pm 1\sigma$.

Each of the objects included in the $E_{\mathrm{T}}^{\mathrm{miss}}$ calculation (see Equation 5.14) has an uncertainty related to its energy scale and energy resolution. Therefore, calculated energy scale and resolution uncertainty scale factors on the objects should be propagated into the $E_{\mathrm{T}}^{\mathrm{miss}}$ [167]. This is done by using $E_{\mathrm{T}}^{\mathrm{miss}}$ weights calculated from the

`MissingETComposition` tool [168]. The $E_{\mathrm{T}}^{\mathrm{miss}}$ weights contain the information on whether or not the object has been included in the $E_{\mathrm{T}}^{\mathrm{miss}}$ calculation.

9.4.2 Jet energy resolution (JER)

The jet energy resolution and its uncertainty have been measured using two different methods, as described in Section 5.3. It is estimated that resolution in data and simulation agree within 10%. The goal of JER is to smear MC jet resolution to match to the data and consider the difference with respect to nominal MC sample as systematic uncertainty. The nominal samples are smeared according to the quadratic difference between the data uncertainty and the MC resolution as provided by the `JERProvider` tool [169].

The effect due to JER systematic variation has been propagated to $E_{\mathrm{T}}^{\mathrm{miss}}$ in the same way as for JES, described in the previous subsection.

9.4.3 Jet reconstruction efficiency (JEF)

The jet reconstruction efficiency accounts for the difference between data and MC in the reconstruction efficiency of calorimeter jets with respect to track jets, measured with a tag-and-probe method in QCD dijet events. The effects of the jet reconstruction efficiency uncertainty are studied by randomly removing about 2% of jets from the events [142].

The effect due to the JEF systematic variation has been propagated to $E_{\mathrm{T}}^{\mathrm{miss}}$.

9.5 Missing transverse energy

The $E_{\mathrm{T}}^{\mathrm{miss}}$ is calculated using Equation 5.14 and Equation 5.15 as it was discussed in Section 5.4. The systematic uncertainty on the `CellOut` term ($E_{\mathrm{T}}^{\mathrm{miss,CellOut}}$), which is built from topoclusters with a correction based on tracks, is calculated from the topoclusters energy scale uncertainties. These uncertainties can be estimated from comparisons between data and MC simulation, for example using the E/p response from single tracks. The overall systematic uncertainty on $E_{\mathrm{T}}^{\mathrm{miss,CellOut}}$ is about 13.2%, which results in a systematic uncertainty of less than 1% on $E_{\mathrm{T}}^{\mathrm{miss}}$ [170].

The systematic uncertainty on the `RefSoftJet` term is 10.5%, which has quite small effect on the cross section, as it is expected, since for the analysis high p_T jets are used. This systematic uncertainty is not considered separately in the analysis and its small effect is covered by including a special treatment for soft jets in the jet energy scale and resolution uncertainties estimation tools.

9.6 Leptons

9.6.1 Lepton identification and trigger (ID SF, Trig SF)

The uncertainties due to MC simulation modeling of the lepton trigger, reconstruction and identification efficiencies have been assessed using tag-and-probe techniques

on $Z \to ll$ and $W \to l\nu$ events selected from the same data sample as used for the $t\bar{t}$ analysis [102]. Lepton trigger, reconstruction and identification efficiencies in simulation were found to be consistent with data. For muons this agreement is within 0.2% (statistical uncertainty) for the reconstruction and identification efficiencies, however, on average the trigger efficiencies disagree by a few percent in specific η and ϕ bins. The disagreements between data and MC can be associated to local residual miscalibrations of the Level-1 barrel trigger [102].

The uncertainties on efficiency scale factor weights, provided in Section 5.1 and Section 5.2 for electrons and muons, respectively, are taken as systematic uncertainty. The identification scale factors for electrons are η and p_{T} dependent, while the muon trigger scale factors are η and ϕ dependent.

9.6.2 Lepton energy scale and resolution (ES, ER)

The accuracy of lepton momentum scale and resolution in simulation was checked using reconstructed distributions of the dilepton invariant mass. To correct for a few percent discrepancy in the $Z \to \mu\mu$ mass distributions between data and simulation, the p_T of a simulated muon was corrected and smeared at the analysis level to reproduce the width and position of the $Z \to \mu\mu$ peak as observed in data. The residual systematic uncertainty on the cross section taking into account the uncertainties of the ID and the MS smearing parameters was also studied. A similar smearing procedure is applied to electrons.

The effect due to systematic variation has been propagated to $E_{\mathrm{T}}^{\mathrm{miss}}$.

9.7 $t\bar{t}$ production modelling

9.7.1 Monte-Carlo generators

Two types of NLO matrix element generators are used to estimate the systematic uncertainty due to the choice of the signal MC generator. The $t\bar{t}$ sample that is used for nominal analysis is generated by MC@NLO and it is compared with a sample generated with POWHEG, see Section 4.3. Both generators are interfaced to HERWIG/JIMMY for hadronization.

9.7.2 Parton shower

The effect of changing the hadronization model in the signal MC is estimated by hadronizing the same POWHEG NLO events once with HERWIG/JIMMY and once with PYTHIA.

9.7.3 Initial and final state radiation

Initial (ISR) and final state (FSR) radiation can affect the jet multiplicity of both signal and background events. The effects of variations in the amount of ISR and FSR were

studied using the LO AcerMC generator [171] interfaced to Pythia, and varying the parameters controlling ISR and FSR in a range consistent with experimental data, see Section 4.3. Two samples with more and less ISR and two samples with more and less FSR are compared with an optimal AcerMC sample.

9.7.4 PDF uncertainties

The effect of uncertainties in the PDF used to generate $t\bar{t}$ and single top events was evaluated using the envelope of error bands from CTEQ6.6, MSTW08 [172] and NNPDF 2.0 [173] sets at NLO [154]. The reweighting method is used to estimate the uncertainty due to the PDF. As the PDF uncertainty, the envelope of all PDF bands is taken and the central value is the center of the envelope [174].

	Background	Acceptance (%)	Cross Section
	3.6 events	11.5	202.0 pb
	Δ Background %	Δ Acceptance	Δ Cross Section %
Luminosity	±1.2	-	±3.7
Data stat	+10.9/-8.6	-	+38.8/-30.5
MC stat	±8.2	±2.2	±3.1
Pile-up	±0.6	±0.3	±0.1
Mis-identified lep.	±26.2	-	±7.0
Drell-Yan method	±10.7	-	±2.6
MC cross section	+5.6/-4.8	-	-1.6/+1.4
JES	+5.3/-1.2	+4.0/-2.8	-5.2/+2.6
JER	±3.0	±0.9	±1.7
JEF	±0.2	±0.1	~ 0.0
$E_{\mathrm{T}}^{\mathrm{miss}}$ CellOut	+3.8/-0.1	+0.1/-0.5	+1.1/-0.5
Mu ID SF	-	-	-
Mu Trig SF	-	-	-
El ID SF	±2.7	±7.4	-7.6/+8.5
El Trig SF	~ 0.0	~ 0.0	~ 0.0
Mu ES	-	-	-
Mu ER (MS)	-	-	-
Mu ER (ID)	-	-	-
El ES	+2.9/-0.0	+0.5/-0.2	-1.2/+0.2
El ER	-0.3/+3.2	+0.0/-0.1	-0.1/+1.0
Parton shower	-	±1.7	±1.7
Generator	-	±0.3	±0.3
ISR	-	+3.4/-0.0	-3.4/+0.0
FSR	-	+6.2/-1.3	-6.2/+1.3
PDF	-	±2.5	±2.5
Syst total	±30.7	+11.7/-8.8	+12.6/-14.8
Cross Section (observed)	$202.0^{+78.5\ +25.6}_{-61.5\ -29.9} \pm 7.6\,\mathrm{pb}$		

Table 9.1 Uncertainties on the background estimation, acceptance and cross section in the *ee* channel. The uncertainties are presented as $+1\sigma/-1\sigma$ variation of the systematic source.

	single top	diboson	$Z\tau\tau$
Yield (events)	0.6	0.5	0.4
Uncertainty(%)			
Lumi	±3.4	±3.4	±3.4
JES	+9.1/-3.6	+10.6/-5.6	+25.9/-13.0
JER	±1.6	±1.5	±25.9
JEF	∼ 0.0	∼ 0.0	∼ 0.0
$E_{\mathrm{T}}^{\mathrm{miss}}$ CellOut	+0.6/-0.3	+0.7/-0.2	+25.9/+0.0
El ID SF	±7.4	±7.4	±7.8
El Trig SF	∼ 0.0	∼ 0.0	∼ 0.0
Mu ID SF	-	-	-
Mu Trig SF	-	-	-
MC cross section	±10.0	±5.0	+41.9/-41.9
MC stat	±6.0	±5.1	±50.1
Pile-up	±2.6	±2.1	±12.4
El ES	+0.6/-1.3	+0.9/-0.8	∼ 0.0
El ER	±0.3	±0.1	∼ 0.0
Mu ES	-	-	-
Mu ER (MS)	-	-	-
Mu ER (ID)	-	-	-
total (syst + lumi)	+17.2/-15.0	+15.5/-12.4	+80.7/-73.0

Table 9.2 Uncertainties on the MC background contributions in the *ee* channel. The uncertainties are presented as $+1\sigma/-1\sigma$ variation of the systematic source.

	Background	Acceptance (%)	Cross Section
	7.2 events	20.5	192.3 pb
	Δ Background %	Δ Acceptance	Δ Cross Section %
Luminosity	±1.4	-	±3.9
Data stat	+7.8/-6.9	-	+28.8/-24.0
MC stat	±9.2	±1.6	±3.4
Pile-up	∼ 0.0	±1.2	±1.2
Mis-identified lep.	±7.1	-	±2.3
Drell-Yan method	±9.2	-	±0.8
MC cross section	+9.1/-10.5	-	-2.8/+3.3
JES	-3.1/+4.2	+1.6/-2.4	-2.6/+1.1
JER	±7.7	±0.1	±2.4
JEF	±0.1	∼ 0.0	∼ 0.0
$E_{\mathrm{T}}^{\mathrm{miss}}$ CellOut	-1.4/+1.2	-0.1/+0.0	+0.5/-0.3
Mu ID SF	±0.6	±1.4	±1.6
Mu Trig SF	±0.1	±0.3	±0.3
El ID SF	-	-	-
El Trig SF	-	-	-
Mu ES	+1.9/-2.8	±0.2	-0.8/+1.1
Mu ER (MS)	+4.7/-2.2	∼ 0.0	-1.5/+0.7
Mu ER (ID)	+1.4/-1.9	-0.2/+0.0	-0.3/+0.6
El ES	-	-	-
El RS	-	-	-
Parton shower	-	±3.3	±3.3
Generator	-	±0.1	±0.1
ISR	-	+1.3/-1.4	-1.3/+1.4
FSR	-	+6.0/-0.0	-6.0/+0.0
PDF	-	±1.9	±1.9
Syst. total	±20.3	+7.8/-5.3	+7.6/-9.9
Cross Section (observed)	$192.3^{+55.4\ +14.6}_{-46.2\ -18.9} \pm 7.6\,\mathrm{pb}$		

Table 9.3 Uncertainties on the background estimation, acceptance and cross section in the $\mu\mu$ channel. The uncertainties are presented as $+1\sigma/-1\sigma$ variation of the systematic source.

	single top	diboson	$Z\tau\tau$
Yield (events)	1.2	0.9	1.2
Uncertainty(%)			
Lumi	±3.4	±3.4	±3.4
JES	±5.3	±9.0	+21.7/-10.9
JER	±0.3	±0.7	±9.7
JEF	±0.3	±0.1	~ 0.0
$E_{\mathrm{T}}^{\mathrm{miss}}$ CellOut	-0.6/+0.3	+0.5/-0.4	+6.7/+0.0
El ID SF	-	-	-
El Trig SF	-	-	-
Mu ID SF	±1.4	±1.4	±1.4
Mu Trig SF	±0.3	+0.2/-0.3	±0.2
MC cross section	±10.0	±5.0	±33.3
MC stat	±4.3	±3.8	±26.9
Pile-up	±2.3	±3.7	±9.8
El ES	-	-	-
El ER	-	-	-
Mu ES	+0.0/-0.2	±0.1	~ 0.0
Mu ER (MS)	-0.2/+0.5	+0.5/-0.1	~ 0.0
Mu ER (ID)	-0.3/+0.5	+1.0/-0.4	-0.0/+5.5
total (syst + lumi)	±12.9	±12.2	+50.8/-46.4

Table 9.4 Uncertainties on the MC background contributions in the $\mu\mu$ channel. The uncertainties are presented as $+1\sigma/-1\sigma$ variation of the systematic source.

	Background	Acceptance (%)	Cross Section
	9.4 events	24.2	171.6 pb
	Δ Background %	Δ Acceptance	Δ Cross Section %
Luminosity	± 2.7	-	± 4.0
Data stat	-	-	+18.0/-15.8
MC stat	± 5.7	± 1.1	± 1.6
Pile-up	± 5.4	± 0.3	± 1.4
Mis-identified lep.	± 18.0	-	± 3.5
Drell-Yan method	-	-	-
MC cross section	± 15.1	-	± 3.0
JES	+7.3/-5.8	+1.3/-1.5	± 2.7
JER	± 1.0	∼ 0.0	± 0.2
JEF	± 0.1	∼ 0.0	± 0.1
$E_{\mathrm{T}}^{\mathrm{miss}}$ CellOut	∼ 0.0	∼ 0.0	∼ 0.0
Mu ID SF	± 0.6	± 0.7	± 0.8
Mu Trig SF	∼ 0.0	∼ 0.0	∼ 0.0
El ID SF	± 3.0	± 3.7	± 4.3
El Trig SF	± 0.1	± 0.1	± 0.1
Mu ES	+0.1/-0.0	+0.0/-0.1	-0.0/+0.1
Mu ER (MS)	∼ 0.0	∼ 0.0	∼ 0.0
Mu ER (ID)	∼ 0.0	∼ 0.0	∼ 0.0
El ES	+1.1/-0.0	+0.1/-0.3	± 0.3
El ER	-0.0/+1.1	∼ 0.0	+0.0/-0.2
Parton shower	-	± 1.2	± 1.2
Generator	-	± 1.3	± 1.3
ISR	-	+3.6/-0.0	-3.6/+0.0
FSR	-	+3.1/-0.0	-3.1/+0.0
PDF	-	± 2.2	± 2.2
Syst. total	± 25.9	+6.9/-5.1	+7.8/-9.0
Cross Section (observed)	$171.6^{+30.9\ +13.4}_{-27.1\ -15.5} \pm 6.8\,\mathrm{pb}$		

Table 9.5 Uncertainties on the background estimation, acceptance and cross section in the $e\mu$ channel. The uncertainties are presented as $+1\sigma/-1\sigma$ variation of the systematic source.

	single top	diboson	$Z\tau\tau$
Yield (events)	2.4	2.0	3.0
Uncertainty(%)			
Lumi	±3.4	±3.4	±3.4
JES	± 5.5	+9.0/-6.5	+12.3/-9.2
JER	±0.2	±4.4	±0.1
JEF	±0.3	±0.1	∼ 0.0
$E_{\mathrm{T}}^{\mathrm{miss}}$ CellOut	∼ 0.0	∼ 0.0	∼ 0.0
El ID SF	± 3.7	± 3.7	± 3.8
El Trig SF	± 0.1	± 0.1	± 0.1
Mu ID SF	± 0.7	± 0.7	± 0.7
Mu Trig SF	∼ 0.0	∼ 0.0	∼ 0.0
MC cross section	± 10.0	± 5.0	± 35.5
MC stat.	±3.1	±2.5	±17.4
Pile-up	±2.3	±2.4	±13.2
El ES	+0.2/-0.0	+0.0/-0.2	+3.1/+0.0
El ER	-0.0/+0.1	-0.0/+0.1	+0.0/+3.1
Mu ES	+0.2/-0.1	+0.1/-0.0	∼ 0.0
Mu ER (MS)	-0.0/+0.2	±0.1	∼ 0.0
Mu ER (ID)	-0.2/+0.1	±0.1	∼ 0.0
total (syst + lumi)	±13.1	+12.8/-11.1	± 43.5

Table 9.6 Uncertainties on the MC background contributions in the $e\mu$ channel. The uncertainties are presented as $+1\sigma/-1\sigma$ variation of the systematic source.

Chapter 10

Results

The measurement of the top quark pair production cross section with the ATLAS detector at LHC, using a data sample corresponding to 35 pb^{-1} collected in 2010, in pp collisions at $\sqrt{s} = 7$ TeV in dilepton final states have been analyzed. The analysis in this thesis is based on a cut-based counting experiment where the Drell-Yan and mis-identified lepton backgrounds are extracted from data, while the rest of the backgrounds and signal contributions are estimated from simulation.

Cross section extraction and the combination of channels

The observed event count for each channel N^{obs} is modeled as being Poisson distributed about some expectation $N^{\text{exp}}_{\text{tot}}$, which is the sum of several contributions from signal and background processes. The variation in the expected number of events from each process due to systematic uncertainties is parametrized and additional terms are included into a likelihood function that summarizes the uncertainty in the corresponding nuisance parameters. The signal expectation is scaled according to the luminosity, and the signal cross section σ_{sig} the parameter of interest, is a free parameter in the fit.

The various sources of systematic uncertainties are organized such that they are considered either totally uncorrelated or totally correlated. For each source of uncertainty (indexed by j), a nuisance parameter α_j is introduced, such that $\alpha_j = 0$ represents the nominal estimate and $\alpha_j = \pm 1$ represents a $\pm 1\sigma$ variation of that source. The sources of the systematics are varied (e.g. jet energy scale, trigger efficiencies, etc.) and a piecewise-linear interpolation is used to parametrize the expected number of events $N^{\text{exp}}_i(\vec{\alpha})$ for each signal and background using the RooFit/RooStats software package [175, 176]. A change in the source of the j^{th} systematic introduces a totally correlated variation among the contributions.

Additional Gaussian (G) terms are added to the likelihood function to summarize our knowledge of the α_j derived from auxiliary measurements or assumptions about the uncertainty in the MC modeling. This leads to the final form of the likelihood function [177]:

$$L(\sigma_{\text{sig}}, \mathcal{L}, \alpha_j) = \prod_{i \in \text{ channel}} \text{Pois}\left(N^{\text{obs}}_i \mid N^{\text{exp}}_{i,\text{tot}}(\vec{\alpha})\right) \times G(\mathcal{L}_0|\mathcal{L}, \sigma_{\mathcal{L}}) \times \prod_{j \in \text{syst}} G(0|\alpha_j, 1)\,. \quad (10.1)$$

The uncertainty on the luminosity is added to the likelihood by multiplying a Gaussian distribution of the luminosity around the nominal estimate $\mathcal{L}_0$ with its uncertainty $\sigma_{\mathcal{L}}$ given the true luminosity $\mathcal{L}$.

The maximum of the function in (10.1) gives the best estimates $\hat{\sigma}_{\text{sig}}$, $\hat{\mathcal{L}}$, and $\hat{\alpha}^{(j)}$. The likelihood ratio r at this point is defined as

$$r(\sigma_{\text{sig}}) = \frac{L(\sigma_{\text{sig}},\hat{\mathcal{L}},\hat{\alpha}^{(j)})}{L(\hat{\sigma}_{\text{sig}},\hat{\mathcal{L}},\hat{\alpha}^{(j)})}\,, \tag{10.2}$$

and the profile likelihood λ is defined as

$$\lambda(\sigma_{\text{sig}}) = \frac{L(\sigma_{\text{sig}},\hat{\hat{\mathcal{L}}},\hat{\hat{\alpha}}^{(j)})}{L(\hat{\sigma}_{\text{sig}},\hat{\mathcal{L}},\hat{\alpha}^{(j)})}\,. \tag{10.3}$$

where $\hat{\hat{\mathcal{L}}}$ and $\hat{\hat{\alpha}}_j$ represent the conditional maximum likelihood estimates of $\mathcal{L}$ and α_j holding σ_{sig} fixed. The best fit value of the cross section is $\hat{\sigma}_{sig}$ and the 68% confidence interval is derived from the values of σ_{sig}, which give $-2\ln\lambda(\sigma_{sig}) = 1$, since $-2\ln\lambda(\sigma_{sig})$ is disrtibuted as $\chi^2(1)$, see [178].

The profile likelihood is always greater than the likelihood ratio, except at the maximum likelihood estimate where they are equal. This means that the curve of $-2\ln\lambda$ is broader than $-2\ln r$, and the difference in the intervals is attributed to systematics.

Table 10.1 summarizes the cross sections extracted from the profile likelihood ratio for the individual channels and for the combination of all three channels. The cross section that corresponds to the minimum position of the likelihood agrees very well with the calculated cross section in the previous section.

Table 10.2 provides the systematic uncertainties for each systematic contribution. The dominant systematic uncertainties are from luminosity, from the electron identification efficiency scale factor, jet energy scale, initial and final state radiation, the background estimation methods and the uncertainties on the simulated samples.

The result of fitting to the observed data, combining all channels together, gives a $\hat{\sigma}_{t\bar{t}}$ of 181 $\pm$ 27 pb, with the 68% confidence interval inferred from the asymptotic properties of the profile likelihood ratio, which is shown in Figure 10.1. This interval includes the effect of all systematic and statistical uncertainties, with their correlated effects on the signal and backgrounds. The statistical uncertainty is obtained by fixing all the nuisance parameters associated with underlying sources of systematics to their best fit values. The component of the total uncertainty attributed to the effect of systematics is obtained by subtracting in quadrature the statistical contribution from the uncertainty obtained by including all sources of systematics, except for the luminosity uncertainty. Finally, the uncertainty attributed to the luminosity is obtained by subtracting in quadrature the combined systematic and statistical uncertainty from the total uncertainty, ensuring that the quadratic sum of all three components is consistent with the uncertainty from all contributions.

The combined result agrees well with the weighted average of the individual cross sections. The uncertainties of the combined result show smaller uncertainties.

Channel	$\sigma_{t\bar{t}}$ (pb)
ee	$202\,^{+67}_{-57}(\text{stat.})\,^{+30}_{-26}(\text{syst.})\,^{+11}_{-1}(\text{lumi.})$
$\mu\mu$	$192\,^{+49}_{-44}(\text{stat.})\,\pm 17(\text{syst.})\,^{+10}_{-5}(\text{lumi.})$
$e\mu$	$172\,\pm 27(\text{stat.})\,\pm 14(\text{syst.})\,^{+8}_{-6}(\text{lumi.})$
combined	$181 \pm 22(\text{stat.})\,\pm 14(\text{syst.})^{+8}_{-7}(\text{lumi.})$

Table 10.1 Measured cross sections in each individual dilepton channel, and all three channels combined. The uncertainties are obtained from the likelihood minimization.

	ee	$\mu\mu$	$e\mu$	combined
Uncertainties (%)				
Data Stat	-28.3 / 33.3	-22.6 / 25.6	-15.2 / 16.6	-11.8 / 12.6
Luminosity	-0.7 / 5.6	-2.4 / 5.2	-3.5 / 4.4	-3.6 / 4.2
MC Stat	-0.7 / 4.6	-2.6 / 4.1	-1.4 / 1.6	-1.9 / 0.5
El/Mu ES	-0.0 / 1.8	-1.1 / 0.7	-0.0 / 0.0	-1.0 / 0.0
El/Mu ER	-0.0 / 1.8	-0.0 / 2.3	-0.0 / 0.0	-1.2 / 0.0
El/Mu SF	-5.0 / 10.9	-0.0 / 3.0	-3.8 / 4.9	-3.6 / 4.1
JES	-3.3 / 4.5	-0.6 / 2.8	-2.7 / 2.8	-3.5 / 2.3
JER	-0.0 / 2.9	-1.6 / 3.0	-0.0 / 0.0	-1.8 / 0.0
JEF	-0.0 / 0.7	-0.0 / 0.0	-0.0 / 0.0	-0.8 / 0.0
$E_{\mathrm{T}}^{\mathrm{miss}}$ CellOut	-0.0 / 1.8	-0.9 / 0.0	-0.0 / 0.0	-0.7 / 0.0
Drell-Yan method	-3.7 / 4.0	-3.9 / 3.6	-0.0 / 0.0	-1.4 / 1.1
Mis-identified lep.	-6.3 / 7.7	-1.4 / 3.0	-3.6 / 3.4	-2.8 / 2.0
Generator	-0.0 / 1.0	-0.0 / 0.0	-1.1 / 1.5	-1.6 / 0.0
Parton shower	-0.0 / 3.1	-1.6 / 4.6	-0.9 / 1.4	-1.9 / 1.7
ISR	-1.0 / 2.4	-1.9 / 0.0	-3.1 / 0.0	-2.5 / 0.0
FSR	-3.0 / 4.0	-3.9 / 2.9	-2.7 / 0.0	-3.7 / 2.4
PDF	-0.0 / 4.1	-0.0 / 3.0	-1.9 / 2.5	-2.0 / 2.4
Pile-up	-0.0 / 1.5	-0.0 / 2.1	-0.8 / 0.6	-0.8 / 0.0
MC cross section	-0.0 / 2.3	-0.9 / 2.7	-2.4 / 2.3	-2.5 / 1.5
All Syst. but Lumi	-12.9 / 14.7	-9.2 / 8.7	-7.9 / 8.1	-7.6 / 7.6
All Syst.	-13.2 / 15.5	-8.6 / 9.9	-8.6 / 9.3	-9.1 / 8.1
Syst+Stat	-31.2 / 36.7	-24.2 / 27.4	-17.4 / 19.0	-14.9 / 15.0

Table 10.2 Overview of the $t\bar{t}$ cross section uncertainties for each channel and each systematic variation obtained from the combination.

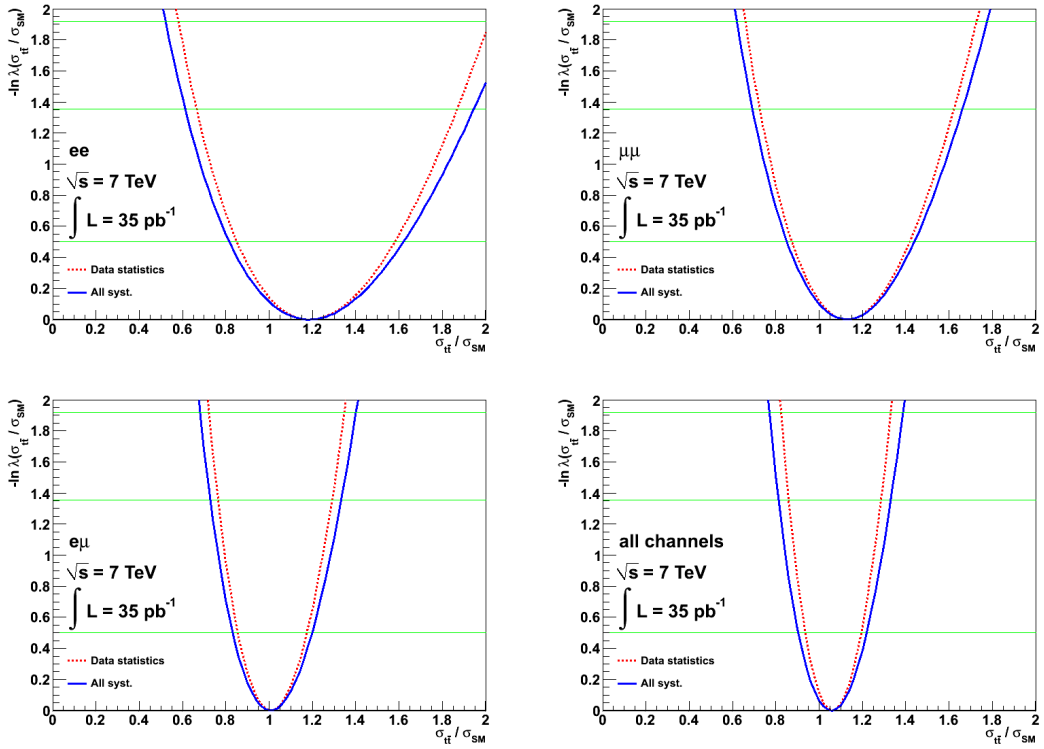

Figure 10.1 Plots of $-\log\lambda(\sigma_{t\bar{t}})$ vs. $\sigma_{t\bar{t}}/\sigma_{\mathrm{SM}}$ with (blue, solid) and without (red, dashed) systematics for the ee (top, left), $\mu\mu$ (top, right), $e\mu$ (bottom, left), and three-channel combined fit (bottom, right). The horizontal lines indicate likelihood values for the 68%, 90% and 95% confidence intervals, respectively.

Chapter 11

Cross-checks with other analyses

Cut and count analysis with b-tagging

The presence of two b-quarks in $t\bar{t}$ decay hints that a requirement of having at least a b-tagged jet in events would help to improve the signal to background ratio. Hence, as an alternative a counting method is used with additional requirement of at least one b-tagged jet in event, using the JetProb algorithm [179] at 70% tagging efficiency operating point. The effectiveness of this strategy is limited by the efficiency (ϵ_b) of the b-tagging algorithms and the uncertainties on the b-tagging efficiency and rejection.

Because of the b-tagging application, requirements on $E_{\mathrm{T}}^{\mathrm{miss}}$, H_{T} and invariant mass of two leptons are loosened. Backgrounds are determined in the same way as described in Chapter 7.

The analysis has some of the same sources of systematic uncertainty as the analysis without b-tagging, see Chapter 9, and these have been estimated in the same way. The only additional source of systematic uncertainty arises from the uncertainty in the efficiencies of the JetProb tagging algorithm. This has been estimated to be 6% for b-quark jets, based on b-tagging calibration studies using inclusive lepton and multijet final states. The uncertainties on the tagging efficiencies for light and charm quarks are several times higher, but are not a large source of uncertainty due to the intrinsically high S/B ratio in the dilepton final state.

These estimates result in $\sim$14 background and $\sim$71 signal events, which is consistent with the observed yield of 98 candidate events. The measured cross section is [1]:

$$\sigma_{t\bar{t}} = 194 \pm 23(\mathrm{stat.})^{+18}_{-14}(\mathrm{syst.}) \pm 7(\mathrm{lumi.})\ \mathrm{pb}\,. \tag{11.1}$$

An inclusive dilepton analysis (AIDA)

A further method is using an inclusive dilepton analysis technique to measure simultaneously the production cross sections of $t\bar{t}$, WW and $Z(\rightarrow \tau\tau)$ in the dilepton final state [180, 181]. This analysis is similar to the dilepton counting analysis without using b-tagging, except that a template shape fit is used instead of counting events, and the selection is relaxed with respect to the number of jets and H_{T}. For the ee and $\mu\mu$ channels which suffer from an overwhelming Drell-Yan contribution, the cuts on $E_{\mathrm{T}}^{\mathrm{miss}}$ and m_{ll} are retained.

The dominant processes with real leptons contributing to the $e\mu$ final state are $t\bar{t}$, WW and $Z(\rightarrow \tau\tau)$, each of which has distinct $E_{\mathrm{T}}^{\mathrm{miss}}$ and N_{jets} characteristics. Typical $t\bar{t}$ events have large $E_{\mathrm{T}}^{\mathrm{miss}}$ and large N_{jets}. WW events usually have large $E_{\mathrm{T}}^{\mathrm{miss}}$ and relatively low N_{jets}, while $Z(\rightarrow \tau\tau)$ events tend to have low $E_{\mathrm{T}}^{\mathrm{miss}}$ and smaller N_{jets}. Therefore, a two-dimensional parameter space defined by $E_{\mathrm{T}}^{\mathrm{miss}}$ and N_{jets} is used to naturally separate these contributions, and fit the observed data to MC generated templates of all expected processes. The normalizations of the main processes described vary as parameters in the fit, allowing a simultaneous measurement of their cross sections. The other "background" contributions are included with fixed normalizations, also considering data-driven backgrounds from Drell-Yan and fake leptons. The $e\mu$ channel is fitted first, and then the $e\mu$, ee and $\mu\mu$ channels are combined in a single fit, using knowledge from $e\mu$ fit.

The measured $t\bar{t}$ cross section is:

$$\sigma_{t\bar{t}} = 171 \pm 22(\mathrm{stat.}) \pm 14(\mathrm{syst.}) \pm 5(\mathrm{lumi.})\ \mathrm{pb}\,. \tag{11.2}$$

WW and $Z(\rightarrow \tau\tau)$ cross sections are estimated to be 59±21(stat.)±12(syst.)±2(lumi.) pb and 1400±290(stat.)±160(syst.)±40(lumi.) pb, respectively, where the theoretical expectations are 46.2±2.3 pb and 1076±54 pb [181].

Cross section measurement with Z normalization

The standard method to extract the cross section uses the luminosity measurement as a normalization. An alternative method is to normalize the measured $\sigma_{t\bar{t}}$ to a theoretically well understood high energy process, such as Z-boson production [154, 181]. This can be achieved by performing an inclusive Z-boson analysis. For the inclusive Z selection MC@NLO is used as the MC generator because the ALPGEN samples were found to give a poor description of the lepton η distributions. The MC is normalized to the NNLO cross section of 989 pb with 5% uncertainty [150].

$\sigma_{t\bar{t}}$ can be extracted by performing a combined fit to the five analysis channels ($t\bar{t} \rightarrow ee$,$e\mu$,$\mu\mu$; $Z \rightarrow ee$,$\mu\mu$), where the free parameters are $\sigma_{t\bar{t}}$ and $\mathcal{L}$. In this way the luminosity (and its uncertainty) used in the standard analysis is replaced with the theoretical prediction and the associated uncertainty on the Z-boson production cross section.

In order to derive $\sigma_{t\bar{t}}$, the likelihood function described in Chapter 10 is extended by adding terms to describe the Z-boson analysis. The top-pair production cross section and integrated luminosity are simultaneously measured from the fit.

$$\sigma_{t\bar{t}} = 178 \pm 22(\mathrm{stat.}) \pm 20(\mathrm{syst.})\ \mathrm{pb}\,, \tag{11.3a}$$

$$\mathcal{L}_{int} = 34.5^{+2.4}_{-2.1}\ \mathrm{pb}^{-1}\,. \tag{11.3b}$$

Simultaneous measurement of the b-tagging efficiency and $\sigma_{t\bar{t}}$

The $t\bar{t}$ candidate events are used directly to measure the fraction of jets that are successfully tagged as b-jets and simultaneously to measure the $t\bar{t}$ production cross section.

In the case that two b-jets are tagged, the expected number of events is $N_{\text{sig}} \cdot \epsilon_b^2$, and with one b-tagged is $2N_{\text{sig}} \cdot \epsilon_b(1-\epsilon_b)$, where N_{sig} is the number of $t\bar{t}$ signal events. However, the number of b-jets varies since b-jets from top quark decays can be out of acceptance or additional b-jets are produced through gluon radiation and gluon splitting. Moreover, c-jets and light jets in the event can also be tagged. These effects are taken into account by defining fractions of events containing b-jets, c-jets and light jets after applying the event selection requirements.

The selection of dilepton candidate events in this analysis is identical to the cut and count analysis without b-tagging. The SV0 b-tagging algorithm [155] is used to b-tag the jets using an operating point that has a nominal b-tagging efficiency of about 50%.

The number of tagged jets distribution is used to simultaneously determine the b-tagging efficiency and the $t\bar{t}$ cross section form a likelihood fit [156, 181]. The measured cross section is:

$$\sigma_{t\bar{t}} = 176 \pm 22(\text{stat.}) \pm 22(\text{syst.}) \pm 6(\text{lumi.})\ \text{pb}\,. \tag{11.4}$$

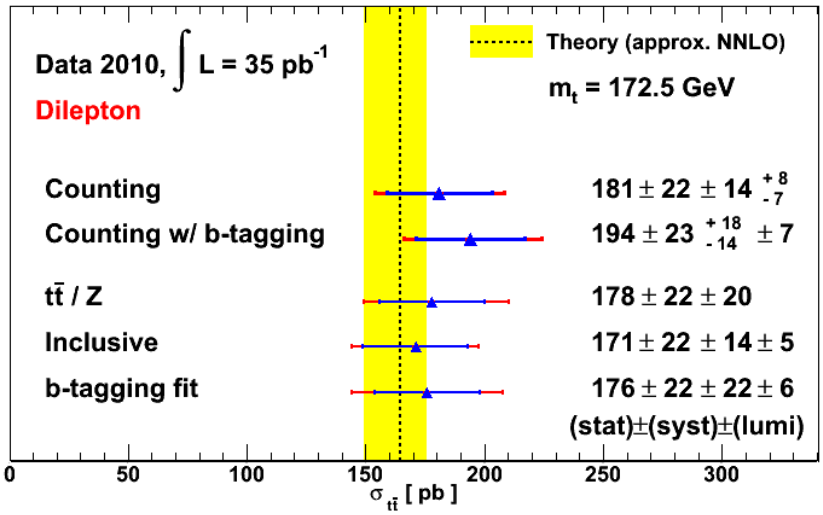

Figure 11.1 The $\sigma_{t\bar{t}}$ cross section measurements from different methods. The yellow bar reflects the uncertainty on the theoretical prediction, which includes some of the NNLO corrections supplemented by soft gluon resummation at the next-to-next-to-leading-logarithm accuracy.

Chapter 12

Conclusion

A measurement of $t\bar{t}$ production cross section with the ATLAS detector at the LHC in pp collisions at $\sqrt{s} = 7$ TeV in final states with two oppositely-charged leptons (ee, $\mu\mu$ and $e\mu$), significant missing transverse energy and two or more jets is presented. In a data set corresponding to an integrated luminosity of 35 pb^{-1}, using a counting method, we observe 104 candidate events, 17 events in the ee channel, 30 events in the $\mu\mu$ channel and 57 events in the $e\mu$ channel. Two background sources, Drell-Yan background and events with one or two mis-identified leptons, are estimated using data-driven techniques. The other processes, $t\bar{t}$ signal, single top, dibosons and $Z/\gamma^* \to \tau\tau$ are considered using MC simulation. The estimated number of signal and background events is 98.9 ± 5.3, with a signal fraction of $\sim 80\%$. The measured cross sections are:

$$ee \text{ channel: } 202\,^{+67}_{-57}(\text{stat.})\,^{+30}_{-26}(\text{syst.})\,^{+11}_{-1}(\text{lumi.}) \text{ pb},$$

$$\mu\mu \text{ channel: } 192\,^{+49}_{-44}(\text{stat.}) \pm 17(\text{syst.})\,^{+10}_{-5}(\text{lumi.}) \text{ pb},$$

$$e\mu \text{ channel: } 172 \pm 27(\text{stat.}) \pm 14(\text{syst.})\,^{+8}_{-6}(\text{lumi.}) \text{ pb},$$

$$\text{Combined: } 181 \pm 22(\text{stat.}) \pm 14(\text{syst.})^{+8}_{-7}(\text{lumi.}) \text{ pb}.$$

To the measured cross section we assign three sources of uncertainties: statistical, systematic, and luminosity uncertainty. As can be seen for all channels, as well as for the combination of three channels, statistical uncertainty dominates. The dominant sources of the systematic uncertainty on the measurement are uncertainties on the luminosity, electron identification efficiency scale factor, jet energy scale, initial and final state radiation, the background estimation methods and the uncertainties on the simulated samples.

The cross sections measured in each of the three sub-channels and for the combination are consistent with each other and kinematic properties of the selected events are consistent with SM $t\bar{t}$ production. The measured $t\bar{t}$ cross section is in good agreement with the SM prediction of 165^{+11}_{-16} pb, and with other analyses performed in the dilepton channel using alternative methods. The measured cross sections also are in good agreement with a similar measurement by the CMS collaboration of $168 \pm 18 \pm 14 \pm 7$ pb [182], using approximately the same amount of data. Figure 12.1 shows the ATLAS and CMS measurements together with previous Tevatron measurements.

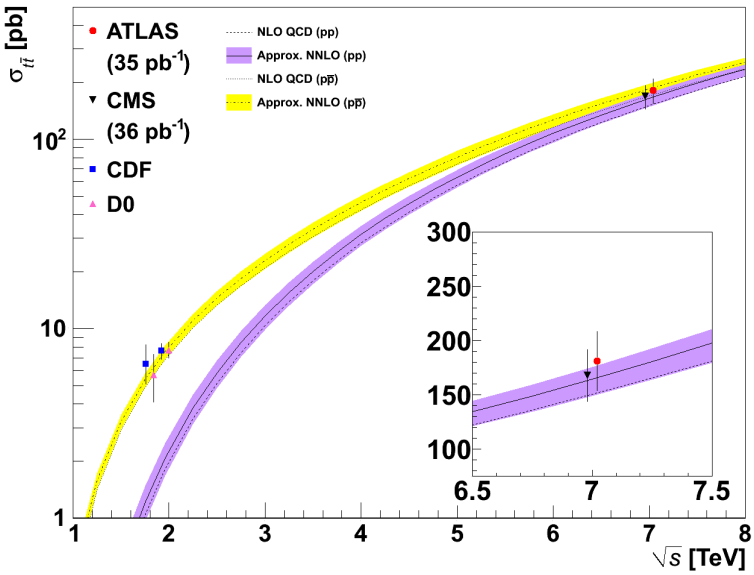

Figure 12.1 Top quark pair-production cross-section at hadron colliders as measured by CDF and D0 at Tevatron, CMS and ATLAS. The theoretical predictions for pp and $p\bar{p}$ collisions include the scale and PDF uncertainties, obtained using the HATHOR tool with the CTEQ6.6 PDFs and assume a top-quark mass of 172.5 GeV.

The analysis presented in this work supersedes the dilepton analysis that was used for the first observation of top quark pairs in ATLAS at the LHC using 2.9 pb^{-1} data sample [24]. The result was $151\,^{+78}_{-62}(\text{stat.})\,^{+37}_{-24}(\text{syst.})$pb [24] (the systematic uncertainty includes the uncertainty from the luminosity). With respect to the previous analysis the number of dilepton candidate events is increased from 9 to 104 events and the statistical uncertainty has decreased to the level of the systematic uncertainty.

With the prospect of accumulation of larger data samples, the statistical and systematic uncertainty on the $t\bar{t}$ cross section can be decreased. Using 0.70 fb^{-1} data collected by ATLAS detector in 2011, a similar measurement has been performed. The measured cross section is $177 \pm 6(\text{stat.})\,^{+17}_{-14}(\text{syst.}) \pm 8(\text{lumi.})$ pb [183], where the systematic uncertainty dominates in the analysis. Precise measurement can challenge the SM prediction based on QCD calculations and constrain the parton distribution functions. Even though ATLAS has reached a point where the systematic uncertainty dominates the analysis many systematic uncertainties are of statistical nature. The systematic uncertainty can be reduced more by using kinematic fits, which also require high statistics. Thus, with a larger sample of $t\bar{t}$ events precision studies can be performed of the production, mass, decay properties of top quarks, and be essential in new physics searches.

Appendix A

Useful information

(a)

E_T/η_{clus}	$[-2.47, -2.01]$	$[-2.01, -1.52]$	$[-1.37, -0.8]$	$[-0.8,0]$
$[20, 25]$	0.917 ± 0.082	0.946 ± 0.084	0.968 ± 0.083	0.907 ± 0.082
$[25, 30]$	0.960 ± 0.028	0.990 ± 0.032	1.013 ± 0.029	0.949 ± 0.027
$[30, 35]$	0.998 ± 0.027	1.029 ± 0.030	1.053 ± 0.027	0.987 ± 0.025
$[35, 40]$	0.996 ± 0.024	1.027 ± 0.028	1.051 ± 0.025	0.985 ± 0.023
$[40, 45]$	0.998 ± 0.025	1.029 ± 0.029	1.053 ± 0.026	0.987 ± 0.024
$[45, \text{inf}]$	1.007 ± 0.033	1.038 ± 0.037	1.062 ± 0.034	0.995 ± 0.032

(b)

E_T/η_{clus}	$[0, 0.8]$	$[0.8, 1.37]$	$[1.52, 2.01]$	$[2.01, 2.47]$
$[20, 25]$	0.912 ± 0.082	0.970 ± 0.082	0.961 ± 0.086	0.953 ± 0.086
$[25, 30]$	0.955 ± 0.027	1.016 ± 0.028	1.006 ± 0.038	0.998 ± 0.036
$[30, 35]$	0.993 ± 0.025	1.056 ± 0.026	1.046 ± 0.037	1.037 ± 0.035
$[35, 40]$	0.991 ± 0.023	1.054 ± 0.024	1.044 ± 0.035	1.035 ± 0.034
$[40, 45]$	0.993 ± 0.024	1.056 ± 0.024	1.046 ± 0.036	1.037 ± 0.034
$[45, \text{inf}]$	1.002 ± 0.032	1.065 ± 0.033	1.055 ± 0.042	1.046 ± 0.041

Table A.1 The efficiency scale factors in different E_T and η_{clus} bins for electron identification $ElectronTight\_WithTrackMatch$.

(a)

	MS	
η region	$\Delta_{p_1}^{MS}(\%)$	$\Delta_{p_2}^{MS}(\ \mathrm{TeV}^{-1})$
barrel	$2.60 \pm 0.10 \pm 0.04$	$0.21 \pm 0.05 \pm 0.01$
transition	$6.95 \pm 0.23\ ^{+0.80}_{-0.00}$	$0.193 \pm 0.09\ ^{+0.06}_{-0.15}$
end-caps	$3.45 \pm 0.35 \pm 0.05$	$0.21 \pm 0.12 \pm 0.01$
CSC/no TRT	$4.05 \pm 0.61 \pm 0.22$	$0.90 \pm 0.19 \pm 0.16$

(b)

	ID	
η region	$\Delta_{p_1}^{ID}(\%)$	$\Delta_{p_2}^{ID}(\ \mathrm{TeV}^{-1})$
barrel	0.03 ± 0.32	$0.396 \pm 0.044 \pm 0.008$
transition	$0.03 \pm 0.54\ ^{+0.10}_{-0.00}$	$0.900 \pm 0.091\ ^{+0.05}_{-0.00}$
end-caps	0.04 ± 0.58	$1.324 \pm 0.045 \pm 0.013$
CSC/no TRT	0.07 ± 0.50	$0.129 \pm 0.004 \pm 0.001$

Table A.2 Set of corrections to be applied to the p_T parameterization of the simulated resolution in the MS and ID to reproduce the one in data [119].

Bibliography

[1] G. Aad et al., *Measurement of the top quark pair production cross section in pp collisions at $\sqrt{s} = 7$ TeV in dilepton final states with ATLAS*, Phys.Lett. **B707** (2012), arXiv:1108.3699 [hep-ex].

[2] D. Griffiths, *Introduction to elementary particles*. 2008.

[3] M. Herrero, *The Standard model*, arXiv:hep-ph/9812242 [hep-ph].

[4] K. Nakamura et al., *Review of particle physics*, J. Phys. G **G37** (2010).

[5] C. Quigg, *Unanswered Questions in the Electroweak Theory*, Ann. Rev. Nucl. Part. Sci. **59** (2009), arXiv:0905.3187 [hep-ph].

[6] F. Deliot and D. A. Glenzinski, *Top Quark Physics at the Tevatron*, arXiv:1010.1202 [hep-ex].

[7] R. Demina and E. J. Thomson, *Top quark properties and interactions*, Ann. Rev. Nucl. Part. Sci. **58** (2008).

[8] J. R. Incandela, A. Quadt, W. Wagner, and D. Wicke, *Status and Prospects of Top-Quark Physics*, Prog. Part. Nucl. Phys. **63** (2009), arXiv:0904.2499 [hep-ex].

[9] R. Kehoe, M. Narain, and A. Kumar, *Review of Top Quark Physics Results*, Int. J. Mod. Phys. **A23** (2008), arXiv:0712.2733 [hep-ex].

[10] A. Quadt, *Top quark physics at hadron colliders*, Eur. Phys. J. **C48** (2006).

[11] D. Wicke, *Properties of the Top Quark*, Eur. Phys. J. **C71** (2011), arXiv:1005.2460 [hep-ex].

[12] W. Bernreuther, *Top quark physics at the LHC*, J. Phys. G **G35** (2008), arXiv:0805.1333 [hep-ph].

[13] M. A. Pleier, *Review of Properties of the Top Quark from Measurements at the Tevatron*, Int. J. Mod. Phys. **A24** (2009), arXiv:0810.5226 [hep-ex].

[14] M. Kobayashi and T. Maskawa, *CP Violation in the Renormalizable Theory of Weak Interaction*, Prog. Theor. Phys. **49** (1973).

[15] S. Herb et al., *Observation of a Dimuon Resonance at 9.5 GeV in 400 GeV Proton-Nucleus Collisions*, Phys. Rev. Lett. **39** (1977).

[16] S. L. Glashow, J. Iliopoulos, and L. Maiani, *Weak Interactions with Lepton-Hadron Symmetry*, Phys. Rev. **D2** (1970).

[17] F. Abe et al., *Observation of top quark production in $p\bar{p}$ collisions*, Phys. Rev. Lett. **74** (1995), arXiv:hep-ex/9503002 [hep-ex].

[18] S. Abachi et al., *Observation of the top quark*, Phys. Rev. Lett. **74** (1995), arXiv:hep-ex/9503003 [hep-ex].

[19] A. D. Martin, W. J. Stirling, R. S. Thorne, and G. Watt, *Update of parton distributions at NNLO*, Phys. Lett. **B652** (2007), arXiv:0706.0459 [hep-ph].

[20] J. Pumplin et al., *New generation of parton distributions with uncertainties from global QCD analysis*, JHEP **0207** (2002), arXiv:hep-ph/0201195 [hep-ph].

[21] P. M. Nadolsky et al., *Implications of CTEQ global analysis for collider observables*, Phys. Rev. **D78** (2008), arXiv:0802.0007 [hep-ph].

[22] U. Langenfeld, S. Moch, and P. Uwer, *New results for $t\bar{t}$ production at hadron colliders*, arXiv:0907.2527 [hep-ph].

[23] S. Catani, *Aspects of QCD, from the Tevatron to the LHC*, arXiv:hep-ph/0005233 [hep-ph].

[24] G. Aad et al., *Measurement of the top quark-pair production cross section with ATLAS in pp collisions at $\sqrt{s} = 7$ TeV*, Eur. Phys. J. **C71** (2011), arXiv:1012.1792 [hep-ex].

[25] V. Khachatryan et al., *First Measurement of the Cross Section for Top-Quark Pair Production in Proton-Proton Collisions at $\sqrt{s} = 7$ TeV*, Phys. Lett. **B695** (2011), arXiv:1010.5994 [hep-ex].

[26] T. Affolder et al., *Measurement of the $t\bar{t}$ production cross section in $p\bar{p}$ collisions at $\sqrt{s} = 1.8$ TeV*, Phys.Rev. **D64** (2001), arXiv:hep-ex/0101036 [hep-ex].

[27] CDF Collaboration, *Measurement of the Top Cross Section in the Lepton+Jets Channel Using Simultaneous Kinematic Fits with 2.7 fb^{-1} of CDF Data*, CDF public note 10137 .

[28] V. M. Abazov et al., *$t\bar{t}$ production cross-section in $p\bar{p}$ collisions at $\sqrt{s} = 1.8$ TeV*, Phys.Rev. **D67** (2003), arXiv:hep-ex/0205019 [hep-ex].

[29] D0 Collaboration, *Measurement of the $t\bar{t}$ production cross section in the lepton+jets final states at D0 using 4.3 fb^{-1} of data*, D0 note 6037-CONF .

[30] M. Jezabek and J. H. Kuhn, *QCD Corrections to Semileptonic Decays of Heavy Quarks*, Nucl.Phys. **B314** (1989).

[31] T. E. W. G., *Combination of CDF and D0 Measurements of the Single Top Production Cross Section*, arXiv:0908.2171 [hep-ex].

[32] N. Kidonakis, *Next-to-next-to-leading-order collinear and soft gluon corrections for t-channel single top quark production*, Phys. Rev. **D83** (2011), arXiv:1103.2792 [hep-ph].

[33] N. Kidonakis, *Two-loop soft anomalous dimensions for single top quark associated production with a W^- or H^-*, Phys. Rev. **D82** (2010), arXiv:1005.4451 [hep-ph].

[34] N. Kidonakis, *NNLL resummation for s-channel single top quark production*, Phys. Rev. **D81** (2010), arXiv:1001.5034 [hep-ph].

[35] ATLAS Collaboration, *Measurement of the t-channel Single Top-Quark Production Cross Section in 0.70 fb^{-1} of pp Collisions at $\sqrt{s} = 7$ TeV with the ATLAS detector*, ATLAS-CONF-2011-101, http://cdsweb.cern.ch/record/1369217.

[36] ATLAS Collaboration, *Search for $W+t$ single-top events in the dileptonic channel at ATLAS*, ATLAS-CONF-2011-104, http://cdsweb.cern.ch/record/1369829.

[37] ATLAS Collaboration, *Search for s-Channel Single Top-Quark Production in pp Collisions at $\sqrt{s} = 7$ TeV*, ATLAS-CONF-2011-118, http://cdsweb.cern.ch/record/1376410.

[38] S. Chatrchyan et al., *Measurement of the t-channel single top quark production cross section in pp collisions at $\sqrt{s} = 7$ TeV*, Phys. Rev. Lett. **107** (2011), arXiv:1106.3052 [hep-ex].

[39] CMS Collaboration, *Search for single top tW associated production in the dilepton decay channel in pp collisions at $\sqrt{s} = 7$ TeV*, CMS-PAS-TOP-11-022, https://cdsweb.cern.ch/record/1385552.

[40] M. Lancaster, *Combination of CDF and D0 results on the mass of the top quark using up to 5.8 fb^{-1} of data*, arXiv:1107.5255 [hep-ex].

[41] ATLAS Collaboration, *Measurement of the top quark mass from 2011 ATLAS data using the template method*, ATLAS-CONF-2011-120, http://cdsweb.cern.ch/record/1376412.

[42] CMS Collaboration, *Measurement of the top quark mass in the l+jets channel*, CMS-PAS-TOP-10-009, https://cdsweb.cern.ch/record/1356578.

[43] ATLAS Collaboration, *Measurement of spin correlation in $t\bar{t}$ production from pp collisions at $\sqrt{s} = 7$ TeV using the ATLAS detector*, ATLAS-CONF-2011-117, http://cdsweb.cern.ch/record/1376409.

[44] ATLAS Collaboration, *Measurement of the top quark charge in pp collisions at $\sqrt{s} = 7$ TeV in the ATLAS experiment.*, ATLAS-CONF-2011-141, http://cdsweb.cern.ch/record/1385517.

[45] ATLAS Collaboration, *Measurement of the charge asymmetry in top quark pair production in pp collisions at $\sqrt{s} = 7$ TeV using the ATLAS detector*, ATLAS-CONF-2011-106, http://cdsweb.cern.ch/record/1372916.

[46] CMS Collaboration, *Measurement of the Charge Asymmetry in Top Quark Pair Production*, CMS-PAS-TOP-11-014, https://cdsweb.cern.ch/record/1369205.

[47] A. Czarnecki, J. G. Korner, and J. H. Piclum, *Helicity fractions of W bosons from top quark decays at NNLO in QCD*, Phys. Rev. **D81** (2010), arXiv:1005.2625 [hep-ph].

[48] ATLAS Collaboration, *Measurement of the W boson polarisation in top quark decays in 0.70 fb^{-1} of pp collisions at $\sqrt{s} = 7$ TeV with the ATLAS detector*, ATLAS-CONF-2011-122, http://cdsweb.cern.ch/record/1376422.

[49] ATLAS Collaboration, *A search for Flavour Changing Neutral Currents in Top Quark Decays $t \to qZ$ at $\sqrt{s} = 7$ TeV in 0.70 fb^{-1} of pp collision data collected with the ATLAS Detector*, ATLAS-CONF-2011-154, http://cdsweb.cern.ch/record/1398198.

[50] S. Brüning et al., *LHC Design Repor. 1. The LHC Main Ring*, CERN-2004-003-V-1, http://cdsweb.cern.ch/record/782076.

[51] O. S. Brüning et al., *LHC Design Report. 2. The LHC Infrastructure and General Services*, CERN-2004-003-V-2, http://cdsweb.cern.ch/record/815187.

[52] C. Lefèvre, *The CERN accelerator complex. Complexe des accélérateurs du CERN*, http://cdsweb.cern.ch/record/1260465.

[53] ATLAS Collaboration, *ATLAS detector and physics performance technical design report. Volume 1*, CERN-LHCC-99-014, http://cdsweb.cern.ch/record/391176.

[54] ATLAS Collaboration, *ATLAS detector and physics performance technical design report. Volume 2*, CERN-LHCC-99-15, http://cdsweb.cern.ch/record/391177.

[55] ATLAS Collaboration, *The ATLAS Experiment at the CERN Large Hadron Collider*, JINST 3 **S08003** (2008).

[56] ATLAS Collaboration, *ATLAS inner detector: Technical Design Report, 1*, CERN-LHCC-97-016, http://cdsweb.cern.ch/record/331063.

[57] ATLAS Collaboration, *ATLAS inner detector: Technical Design Report, 1*, CERN-LHCC-97-017, http://cdsweb.cern.ch/record/331064.

[58] ATLAS Collaboration, *ATLAS pixel detector: Technical Design Report*, ATLAS-TDR-011, CERN-LHCC-98-013, http://cdsweb.cern.ch/record/381263.

[59] ATLAS Collaboration, *ATLAS liquid-argon calorimeter: Technical Design Report*, ATLAS-TDR-002, CERN-LHCC-96-041, http://cdsweb.cern.ch/record/331061.

[60] H. J. Kim, *Electron and Photon Identification Performance in ATLAS*, arXiv:0810.3415 [hep-ex].

[61] ATLAS Collaboration, *ATLAS tile calorimeter: Technical Design Report*, ATLAS-TDR-003, CERN-LHCC-96-042, http://cdsweb.cern.ch/record/331062.

[62] ATLAS Collaboration, *ATLAS muon spectrometer: Technical Design Report*, ATLAS-TDR-010, CERN-LHCC-97-022, http://cdsweb.cern.ch/record/331068.

[63] ATLAS Collaboration, G. Aad et al., *Luminosity Determination in pp Collisions at $\sqrt{s} = 7$ TeV Using the ATLAS Detector at the LHC*, Eur. Phys. J. **C71** (2011), arXiv:1101.2185 [hep-ex].

[64] ATLAS Collaboration, *Report from the Luminosity Task Force*, ATL-GEN-PUB-2006-002, https://cdsweb.cern.ch/record/970678.

[65] ATLAS Collaboration, *Determination of the absolute luminosity and the visible cross section from LHC van der Meer scans performed in October 2010, using events with MBTS triggers and with primary vertices*, ATL-COM-LUM-2011-003, https://cdsweb.cern.ch/record/1326897.

[66] *2010 pp Collisions*, https://twiki.cern.ch/twiki/bin/view/AtlasPublic/LuminosityPublicResults#2010_pp_Collisions.

[67] *2010 Data Periods for pp running*, https://twiki.cern.ch/twiki/bin/view/AtlasProtected/DataPeriods#2010_Data_Periods_for_pp_running.

[68] ATLAS Collaboration, *Technical aspects of the first top pair analyses*, ATL-PHYS-INT-2010-140, https://cdsweb.cern.ch/record/1317309.

[69] *Moriond* GRL, https://twiki.cern.ch/twiki/bin/view/AtlasProtected/TopGRLs#Moriond.

[70] M. A. Dobbs et al., *Les Houches guidebook to Monte Carlo generators for hadron collider physics*, arXiv:hep-ph/0403045 [hep-ph].

[71] A. D. Martin et al., *Uncertainties of predictions from parton distributions. 1: Experimental errors*, Eur. Phys. J. **C28** (2003), arXiv:hep-ph/0211080 [hep-ph].

[72] ATLAS Collaboration, *The HepMC C++ Monte Carlo Event Record for High Energy Physics*, ATL-SOFT-2000-001, https://cdsweb.cern.ch/record/684090.

[73] B. P. Kersevan and E. Richter-Was, *The Monte-Carlo event generator AcerMC version 1.0 with interfaces to Pythia 6.2 and Herwig 6.3*, Comput. Phys. Commun. **149** (2003), arXiv:hep-ph/0201302 [hep-ph].

[74] *AcerMC Monte-Carlo Generator*, http://borut.web.cern.ch/borut/.

[75] M. L. Mangano et al., ALPGEN*, a generator for hard multiparton processes in hadronic collisions*, JHEP **0307** (2003), arXiv:hep-ph/0206293 [hep-ph].

[76] S. Frixione and B. R. Webber, *Matching NLO QCD computations and parton shower simulations*, JHEP **0206** (2002), arXiv:hep-ph/0204244 [hep-ph].

[77] S. Frixione, P. Nason, and B. R. Webber, *Matching NLO QCD and parton showers in heavy flavor production*, JHEP **0308** (2003), arXiv:hep-ph/0305252 [hep-ph].

[78] S. Frixione, P. Nason, and C. Oleari, *Matching NLO QCD computations with Parton Shower simulations: the POWHEG method*, JHEP **0711** (2007), arXiv:0709.2092 [hep-ph].

[79] T. Sjostrand et al., *High-energy physics event generation with Pythia 6.1*, Comput. Phys. Commun. **135** (2001), arXiv:hep-ph/0010017 [hep-ph].

[80] *PYTHIA*, http://home.thep.lu.se/~torbjorn/Pythia.html.

[81] G. Corcella et al., HERWIG *6: An Event generator for hadron emission reactions with interfering gluons (including supersymmetric processes)*, JHEP **0101** (2001), arXiv:hep-ph/0011363 [hep-ph].

[82] J. M. Butterworth, J. R. Forshaw, and M. H. Seymour, *Multiparton interactions in photoproduction at HERA*, Z. Phys. **C72** (1996), arXiv:hep-ph/9601371 [hep-ph].

[83] J. M. Butterworth and J. R. Forshaw, *Photoproduction of multi-jet events at HERA: A Monte Carlo simulation*, J. Phys. G **G19** (1993).

[84] *ATLAS Generators and Interface Documentation*, https://twiki.cern.ch/twiki/bin/view/AtlasProtected/McGeneratorsForAtlas.

[85] S. Agostinelli et al., GEANT4*: A Simulation toolkit*, Nucl. Instrum. Meth. **A506** (2003).

[86] G. Aad et al., *The ATLAS Simulation Infrastructure*, Eur. Phys. J. **C70** (2010), arXiv:1005.4568 [physics.ins-det].

[87] S. Frixione, E. Laenen, P. Motylinski, and B. R. Webber, *Single-top production in MC@NLO*, JHEP **0603** (2006), arXiv:hep-ph/0512250 [hep-ph].

[88] M. Aliev et al., *HATHOR: HAdronic Top and Heavy quarks cross section calculatoR*, Comput. Phys. Commun. **182** (2011), arXiv:1007.1327 [hep-ph].

[89] S. Frixione, E. Laenen, P. Motylinski, B. R. Webber, and C. D. White, *Single-top hadroproduction in association with a W boson*, JHEP **0807** (2008), arXiv:0805.3067 [hep-ph].

[90] J. M. Campbell and R. K. Ellis, *An Update on vector boson pair production at hadron colliders*, Phys. Rev. **D60** (1999), arXiv:hep-ph/9905386 [hep-ph].

[91] ATLAS Collaboration, *First tuning of* Herwig/Jimmy *to ATLAS data*, ATL-PHYS-PUB-2010-014, https://cdsweb.cern.ch/record/1303025.

[92] ATLAS Collaboration, *Monte Carlo samples used for top physics*, ATL-PHYS-INT-2010-132, https://cdsweb.cern.ch/record/1312945.

[93] *TopMC2010*, https://twiki.cern.ch/twiki/bin/view/AtlasProtected/TopMC2010.

[94] ATLAS Collaboration, *Expected electron performance in the ATLAS experiment*, ATL-PHYS-PUB-2011-006, https://cdsweb.cern.ch/record/1345327.

[95] G. Aad et al., *Expected Performance of the ATLAS Experiment - Detector, Trigger and Physics*, arXiv:0901.0512 [hep-ex].

[96] *ElectronReconstruction*, https://twiki.cern.ch/twiki/bin/view/AtlasProtected/ElectronReconstruction.

[97] *Sliding Window Clustering*, https://twiki.cern.ch/twiki/bin/viewauth/Atlas/SlidingWindowClustering.

[98] ATLAS Collaboration, *In-situ electron performance measurements with the ATLAS detector using the 2010 LHC proton-proton collision data*, ATL-COM-PHYS-2011-546, https://cdsweb.cern.ch/record/1352407.

[99] *Electron selection*, https://twiki.cern.ch/twiki/bin/view/AtlasProtected/TopCommonObjects2010#Electrons.

[100] *Overlap between egamma and softe*, https://twiki.cern.ch/twiki/bin/view/AtlasProtected/EnergyRescaler.

[101] ATLAS Collaboration, *Expected electron performance in the ATLAS experiment*, ATL-COM-PHYS-2010-990, https://cdsweb.cern.ch/record/1309937.

[102] ATLAS Collaboration, *Lepton trigger and identification for the Winter 2011 top quark analyses*, ATL-COM-PHYS-2011-123, https://cdsweb.cern.ch/record/1328033.

[103] ATLAS Collaboration, *Study of electron isolation in $Z \to ee$ and $t\bar{t}$ decays*, ATL-PHYS-INT-2009-113, https://cdsweb.cern.ch/record/1229419.

[104] ATLAS Collaboration, *Electromagnetic energy scale in-situ calibration and performance: Supporting document for the egamma performance paper*, ATL-COM-PHYS-2011-263, https://cdsweb.cern.ch/record/1335395.

[105] *EnergyRescaler*, https://twiki.cern.ch/twiki/bin/view/AtlasProtected/EnergyRescaler.

[106] *Electron efficiency scale factors*, https://twiki.cern.ch/twiki/bin/view/AtlasProtected/TopCommonScales2010#Electrons_ElectronTight_WithTrac.

[107] ATLAS Collaboration, *Electron efficiency measurements using ATLAS 2010 data at $\sqrt{s} = 7$ TeV: Supporting note for the 2010 egamma paper*, ATL-COM-PHYS-2011-322, https://cdsweb.cern.ch/record/1340242.

[108] *Trigger efficiency*, https://twiki.cern.ch/twiki/bin/view/AtlasProtected/EfficiencyMeasurements#Trigger_efficiency.

[109] *ObjectQualityMaps*, https://twiki.cern.ch/twiki/bin/view/AtlasProtected/ObjectQualityMaps.

[110] ATLAS Collaboration, *Identification of muon candidates in pp collisions at $\sqrt{s} = 900$ GeV with the ATLAS detector*, ATLAS-CONF-2010-015, https://cdsweb.cern.ch/record/1276549.

[111] ATLAS Collaboration, *Muon Performance in Minimum Bias pp Collision Data at $\sqrt{s} = 7$ TeV with ATLAS*, ATLAS-CONF-2010-036, https://cdsweb.cern.ch/record/1277675.

[112] ATLAS Collaboration, *Muon Reconstruction Performance*, ATLAS-CONF-2010-064, https://cdsweb.cern.ch/record/1281339.

[113] ATLAS Collaboration, *Atlas Computing Technical Design Report*, CERN-LHCC-2005-022, ATLAS-TDR-017, https://cdsweb.cern.ch/record/837738.

[114] *Athena Core software*, http://atlas-computing.web.cern.ch/atlas-computing/packages/athenaCore/athenaCore.php.

[115] *StacoMuonCollection*, https://twiki.cern.ch/twiki/bin/view/AtlasProtected/StacoMuonCollection.

[116] *MuidMuonCollection*, https://twiki.cern.ch/twiki/bin/view/AtlasProtected/MuidMuonCollection.

[117] *MuonRecoPedia*, https://twiki.cern.ch/twiki/bin/view/AtlasProtected/MuonRecoPedia.

[118] *Quality Definition for Identified Muons*, https://twiki.cern.ch/twiki/bin/view/AtlasProtected/MuonCombinedQualityDocumentation.

[119] ATLAS Collaboration, *Muon Momentum Resolution in First Pass Reconstruction of pp Collision Data Recorded by ATLAS in 2010*, ATLAS-CONF-2011-046, https://cdsweb.cern.ch/record/1338575.

[120] G. Aad et al., *Commissioning of the ATLAS Muon Spectrometer with Cosmic Rays*, Eur. Phys. J. **C70** (2010), arXiv:1006.4384.

[121] *Muon selection*, https://twiki.cern.ch/twiki/bin/view/AtlasProtected/TopCommonObjects2010#Muons.

[122] ATLAS Collaboration, *Performance of Jet Algorithms in the ATLAS Detector*, ATL-PHYS-INT-2010-129, https://cdsweb.cern.ch/record/1311867.

[123] M. Seymour, *Jet shapes in hadron collisions: Higher orders, resummation and hadronization*, Nucl. Phys. **B513** (1998), arXiv:hep-ph/9707338 [hep-ph].

[124] G. P. Salam and G. Soyez, *A practical Seedless Infrared-Safe Cone jet algorithm*, JHEP **05** (2007), arXiv:0704.0292 [hep-ph].

[125] S. Catani, Y. L. Dokshitzer, M. H. Seymour, and B. R. Webber, *Longitudinally invariant k_T clustering algorithms for hadron hadron collisions*, Nucl. Phys. **B406** (1993).

[126] S. D. Ellis and D. E. Soper, *Successive combination jet algorithm for hadron collisions*, Phys. Rev. **D48** (1993), arXiv:hep-ph/9305266 [hep-ph].

[127] G. P. Salam, *Towards Jetography*, Eur. Phys. J. **C67** (2010), arXiv:0906.1833 [hep-ph].

[128] ATLAS Collaboration, *k_T Algorithms in Athena: timing performances and new implementation*, ATL-COM-SOFT-2006-007, https://cdsweb.cern.ch/record/974641.

[129] Y. L. Dokshitzer, G. D. Leder, S. Moretti, and B. R. Webber, *Better jet clustering algorithms*, JHEP **9708** (1997), arXiv:hep-ph/9707323 [hep-ph].

[130] M. Cacciari, G. P. Salam, and G. Soyez, *The Anti-k_T jet clustering algorithm*, JHEP **0804** (2008), arXiv:0802.1189 [hep-ph].

[131] *JetAlgorithms*, https://twiki.cern.ch/twiki/bin/view/AtlasProtected/JetAlgorithms.

[132] ATLAS Collaboration, *Jet energy scale and its systematic uncertainty in ATLAS for jets produced in proton-proton collisions at* $\sqrt{s} = 7$ *TeV*, ATLAS-CONF-2010-056, https://cdsweb.cern.ch/record/1281329.

[133] K. J. Grahn, A. Kiryunin, and G. Pospelov, *Tests of local hadron calibration approaches in ATLAS combined beam tests*, J. Phys. Conf. Ser. **293** (2011).

[134] ATLAS Collaboration, *Jet energy scale and its systematic uncertainty in proton-proton collisions at* $\sqrt{s} = 7$ *TeV in ATLAS 2010 data*, ATLAS-CONF-2011-032, https://cdsweb.cern.ch/record/1337782.

[135] ATLAS Collaboration, *Determination of the ATLAS jet energy measurement uncertainty using photon-jet events in proton-proton collisions at* $\sqrt{s} = 7$ *TeV*, ATLAS-CONF-2011-031, https://cdsweb.cern.ch/record/1337781.

[136] ATLAS Collaboration, *Properties of Jets and Inputs to Jet Reconstruction and Calibration with the ATLAS Detector Using Proton-Proton Collisions at* $\sqrt{s} = 7$ *TeV*, ATLAS-CONF-2010-053, https://cdsweb.cern.ch/record/1281310.

[137] ATLAS Collaboration, *In-situ jet energy scale and jet shape corrections for multiple interactions in the first ATLAS data at the LHC*, ATLAS-CONF-2011-030, https://cdsweb.cern.ch/record/1337780.

[138] ATLAS Collaboration, *Probing the jet energy measurement at the TeV-scale using the multi-jet balance technique in proton-proton collisions at* $\sqrt{s} = 7$ *TeV*, ATLAS-CONF-2011-029, https://cdsweb.cern.ch/record/1337076.

[139] ATLAS Collaboration, *ATLAS Calorimeter Response to Single Isolated Hadrons and Estimation of the Calorimeter Jet Scale Uncertainty*, ATLAS-CONF-2010-052, https://cdsweb.cern.ch/record/1281309.

[140] ATLAS Collaboration, *Close-by Jet Effects on Jet Energy Scale Calibration in pp Collisions at* $\sqrt{s} = 7$ *TeV with the ATLAS Detector*, ATLAS-CONF-2011-062, https://cdsweb.cern.ch/record/1345091.

[141] ATLAS Collaboration, *Jet energy resolution and selection efficiency relative to track jets from in-situ techniques with the ATLAS Detector Using Proton-Proton Collisions at a Center of Mass Energy* $\sqrt{s} = 7$ *TeV*, ATLAS-CONF-2010-054, https://cdsweb.cern.ch/record/1281311.

[142] ATLAS Collaboration, *Jet selection for top physics*, ATL-PHYS-INT-2010-134, https://cdsweb.cern.ch/record/1312952.

[143] ATLAS Collaboration, *Jet Energy Resolution Improvement After Calibration Using Longitudinal Calorimeter Segmentation in ATLAS*, ATL-PHYS-INT-2009-051, https://cdsweb.cern.ch/record/1171280.

[144] ATLAS Collaboration, *Jet Energy Resolution from In-situ Techniques with the ATLAS Detector Using Proton-Proton Collisions at a Center of Mass Energy* $\sqrt{s} = 7$ *TeV*, ATL-COM-PHYS-2011-240, https://cdsweb.cern.ch/record/1334193.

[145] ATLAS Collaboration, *Jets, Missing Transverse Energy and Taus for Top Physics Analyses in Release 16 with the 2010 Dataset*, ATL-PHYS-INT-2011-079, https://cdsweb.cern.ch/record/1386329.

[146] *Jet selection*, https://twiki.cern.ch/twiki/bin/view/AtlasProtected/TopCommonObjects2010#Jets.

[147] ATLAS Collaboration, *Missing Transverse Energy for Top Physics analyses with early ATLAS data at* $\sqrt{s} = 7$ *TeV*, ATL-PHYS-INT-2010-135, https://cdsweb.cern.ch/record/1312953.

[148] ATLAS Collaboration, *Jets, Missing Transverse Energy and Taus for Top Physics Analyses in Release 16 with the 2010 Dataset*, ATL-PHYS-INT-2011-079, https://cdsweb.cern.ch/record/1386329.

[149] J. Butterworth et al., *Single Boson and Diboson Production Cross Sections in pp Collisions at* $\sqrt{s} = 7$ *TeV*, ATL-COM-PHYS-2010-695, https://cdsweb.cern.ch/record/1287902.

[150] J. Barreiro Guimaraes da Costa et al., $W \to \mu\nu$ *and* $Z \to \mu\mu$ *cross-sections measurements in proton-proton collisions at* $\sqrt{s} = 7$ *TeV with the ATLAS Detector*, ATL-PHYS-INT-2011-019, https://cdsweb.cern.ch/record/1334831.

[151] ATLAS Collaboration, *Data-Quality Requirements and Event Cleaning for Jets and Missing Transverse Energy Reconstruction with the ATLAS Detector in Proton-Proton Collisions at a Center-of-Mass Energy of* $\sqrt{s} = 7$ *TeV*, ATLAS-CONF-2010-038, https://cdsweb.cern.ch/record/1277678.

[152] *MCTruthClassifier*, https://twiki.cern.ch/twiki/bin/view/AtlasProtected/MCTruthClassifier.

[153] ATLAS Collaboration, *Mis-identified lepton backgrounds to top quark pair production for Moriond 2011 analysis*, ATL-COM-PHYS-2011-144, https://cdsweb.cern.ch/record/1328921.

[154] ATLAS Collaboration, *The measurement of* $t\bar{t}$ *cross section in the dilepton decay channel with cut-and-count methods at* $\sqrt{s} = 7$ *TeV with 35* pb^{-1}, ATL-PHYS-INT-2011-046, https://cdsweb.cern.ch/record/1348786.

[155] ATLAS Collaboration, *Calibrating the b-Tag and Mistag Efficiencies of the SV0 b-Tagging Algorithm in 3 pb^{-1} of Data with the ATLAS Detector*, ATLAS-CONF-2010-099, https://cdsweb.cern.ch/record/1312145.

[156] ATLAS Collaboration, *Calibrating the b-Tag Efficiency and Mistag Rate in $\mathcal{L}$=35 pb^{-1} of Data with the ATLAS Detector*, ATLAS-CONF-2011-089, https://cdsweb.cern.ch/record/1356198.

[157] ATLAS Collaboration, *Study of the m_{T2} variable in the ttbar dilepton channel in pp collisions at $\sqrt{s} = 7$ TeV with 1.035 fb^{-1} ATLAS data*, ATL-COM-PHYS-2011-1006, https://cdsweb.cern.ch/record/1371545.

[158] P. Sinervo, *Definition and treatment of systematic uncertainties in high energy physics and astrophysics*, https://cdsweb.cern.ch/record/931829.

[159] *TopSystematicUncertainties2010Paper*, https://twiki.cern.ch/twiki/bin/view/AtlasProtected/TopSystematicUncertainties2010Paper.

[160] ATLAS Collaboration, *Updated Luminosity Determination in pp Collisions at $\sqrt{s} = 7$ TeV using the ATLAS Detector*, ATLAS-CONF-2011-011, http://cdsweb.cern.ch/record/1334563.

[161] J. Alwall et al., *Comparative study of various algorithms for the merging of parton showers and matrix elements in hadronic collisions*, Eur. Phys. J. **C53** (2008), arXiv:0706.2569 [hep-ph].

[162] J. M. Campbell, R. K. Ellis, and F. Tramontano, *Single top production and decay at next-to-leading order*, Phys. Rev. **D70** (2004), arXiv:hep-ph/0408158.

[163] N. Kidonakis, *Single top quark production cross section at hadron colliders*, PoS **DIS2010** (2010), arXiv:1005.3330 [hep-ph].

[164] J. M. Campbell and R. K. Ellis, *MCFM for the Tevatron and the LHC*, Nucl. Phys. Proc. Suppl. **205-206** (2010), arXiv:1007.3492 [hep-ph].

[165] G. Aad et al., *Measurement of inclusive jet and dijet cross sections in proton-proton collisions at 7 TeV centre-of-mass energy with the ATLAS detector*, Eur. Phys. J. **C71** (2011), arXiv:1009.5908 [hep-ex].

[166] *MultijetJESUncertaintyProvider for Top*, https://twiki.cern.ch/twiki/bin/view/AtlasProtected/MultijetJESUncertaintyProviderTop.

[167] *Propagation of Energy Scale and Resolution of Reconstructed Objects in the $E_{\mathrm{T}}^{\mathrm{miss}}$*, https://twiki.cern.ch/twiki/bin/view/AtlasProtected/TopETmissLiaison16-0-3-8-2#Recommendations_for_Calculating.

[168] *MissingETComposition*, https://twiki.cern.ch/twiki/bin/view/AtlasProtected/MissingETComposition.

[169] *JetEnergyResolutionProvider*, `https://twiki.cern.ch/twiki/bin/view/Main/JetEnergyResolutionProvider`.

[170] ATLAS Collaboration, *Reconstruction and Calibration of Missing Transverse Energy and Performance in Z and W events in ATLAS Proton-Proton Collisions at 7 TeV*, ATLAS-CONF-2011-080, `https://cdsweb.cern.ch/record/1355703`.

[171] B. P. Kersevan and E. Richter-Was, *The Monte Carlo event generator* AcerMC *version 2.0 with interfaces to* Pythia *6.2 and* Herwig *6.5*, `arXiv:hep-ph/0405247 [hep-ph]`.

[172] A. D. Martin et al., *Parton distributions for the LHC*, Eur. Phys. J. **C63** (2009), `arXiv:0901.0002 [hep-ph]`.

[173] R. D. Ball et al., *A first unbiased global NLO determination of parton distributions and their uncertainties*, Nucl. Phys. **B838** (2010), `arXiv:1002.4407 [hep-ph]`.

[174] ATLAS Collaboration, *Analysis of $t\bar{t}$ production in the dilepton decay channel at 7 TeV with 2.9 pb^{-1}*, ATL-PHYS-INT-2010-141, `https://cdsweb.cern.ch/record/1317592`.

[175] W. Verkerke and D. P. Kirkby, *The RooFit toolkit for data modeling*, `arXiv:physics/0306116`.

[176] M. Lorenzo et al., *The RooStats Project*, PoS **ACAT2010** (2010), `arXiv:1009.1003 [physics.data-an]`.

[177] ATLAS Collaboration, *A combined measurement of the top quark pair production cross-section using dilepton and single-lepton final states*, ATLAS-CONF-2011-040, `https://cdsweb.cern.ch/record/1338569`.

[178] G. Cowan, *Statistical data analysis*. 1998.

[179] ATLAS Collaboration, *Impact parameter-based b-tagging algorithms in the 7 TeV collision data with the ATLAS detector: the TrackCounting and JetProb algorithms*, ATLAS-CONF-2010-041, `https://cdsweb.cern.ch/record/1277681`.

[180] ATLAS Collaboration, *An Inclusive Analysis of $t\bar{t}$, WW, and $Z(\rightarrow \tau\tau)$ Production Using the Dilepton Final State at 7 TeV Using 35.3 pb^{-1}*, ATL-COM-PHYS-2011-127, `https://cdsweb.cern.ch/record/1328261`.

[181] ATLAS Collaboration, *Measurement of the top quark pair production cross-section with ATLAS in pp collisions at $\sqrt{s} = 7$ TeV in dilepton final states*, ATLAS-CONF-2011-034, `https://cdsweb.cern.ch/record/1337784`.

[182] S. Chatrchyan et al., *Measurement of the $t\bar{t}$ production cross section and the top quark mass in the dilepton channel in pp collisions at $\sqrt{s} = 7$ TeV*, JHEP **1107** (2011), `arXiv:1105.5661 [hep-ex]`.

[183] ATLAS Collaboration, *Measurement of the top quark pair production cross section in pp collisions at $\sqrt{s} = 7$ TeV in dilepton final states with ATLAS*, ATLAS-CONF-2011-100, `https://cdsweb.cern.ch/record/1369215`.

List of Figures

2.1 Leading-order Feynman diagrams for $t\bar{t}$-pair production via gluon fusion processes and the quark-antiquark annihilation process. 8
2.2 $t\bar{t}$ production cross sections as a function of top mass at NLO (blue band) and NNLO (red band) at the LHC [22]. 9
2.3 Production cross sections for several processes as a function of the center-of-mass energy. The expected cross sections are calculated for $p\bar{p}$ and pp collisions for the Tevatron and LHC energy ranges, respectively, therefore the lines are not continuous [23]. 10
2.4 PDFs of some of the quarks and gluons inside the proton, using CTEQ6.5 parameterization. 11
2.5 Top quark pair-production cross-section at hadron colliders as measured by CDF [26, 27] and D0 [28, 29] at Tevatron, CMS and ATLAS. The theoretical predictions for pp and $p\bar{p}$ collisions include the scale and PDF uncertainties, obtained using the HATHOR tool with the CTEQ6.6 PDFs and assume a top-quark mass of 172.5 GeV [24]. 12
2.6 Decay of top and anti-top quarks. 12
2.7 Examples of Feynman diagrams for single top production. 14
2.8 Virtual top quark loops contributing to the W- and Z-boson masses. . . 16
2.9 Virtual Higgs boson loops contributing to the W- and Z-boson masses. . 16
2.10 Summary of the input measurements and resulting Tevatron average mass of the top quark [40]. 17
2.11 Lines of constant Higgs mass on a plot of m_W vs. m_t. The dotted ellipse is the 68% C.L. direct measurement of m_W and m_t. The solid ellipse is the 68% C.L. indirect measurement from precision electroweak data [8]. . 17

3.1 CERN accelerator complex [52]. 22
3.2 A cut-away view of the ATLAS detector. 23
3.3 A cut-away view of the ATLAS inner detector. 24
3.4 A cut-away view of the ATLAS calorimeter. 26
3.5 A cut-away view of the ATLAS muon system. 27
3.6 The ATLAS toroid magnet system layout. 28
3.7 ATLAS trigger and data acquisition system. 29

4.1 Cumulative luminosity versus day delivered to (green), and recorded by (yellow) ATLAS during stable beams and for pp collisions at $\sqrt{s} = 7$TeV [66]. 32
4.2 Hard hadronic scattering event in the MC generation [72, 70]. 35

5.1 The `EtCone20`, `EtCone30` and `EtCone40` distribution mean values as a function of the electron E_T in MC simulation of electrons from W-bosons in $t\bar{t}$ decays [102]. 42

5.2 The transverse energy deposited in the calorimeters in a cone of $\Delta R = 0.3$ normalized to the transverse momentum of the muon as a function of the distance to the closest jet. No overlap removal between muons and jets is performed [111]. 47

6.1 $ee + \mu\mu$ channels (left) and $e\mu$ channel (right): top row $E_{\mathrm{T}}^{\mathrm{miss}}$, middle row dilepton invariant mass and bottom row H_{T} distributions. All object and event selection (listed in the Table 6.2) requirements are applied, relaxing cuts on $E_{\mathrm{T}}^{\mathrm{miss}}$, dilepton invariant mass and H_{T}. Contributions from diboson and single top events are summarized as "other EW". 59

6.2 ee channel (left) and $\mu\mu$ channel (right): top row significance as a function of $E_{\mathrm{T}}^{\mathrm{miss}}$ versus the Z mass window, middle row projection of significance versus $E_{\mathrm{T}}^{\mathrm{miss}}$ when the Z mass window cut is applied to its optimised value, bottom row projection of significance versus Z mass window when $E_{\mathrm{T}}^{\mathrm{miss}}$ cut is applied to its optimised value. 61

6.3 $e\mu$ channel: (a) significance as a function of H_{T} versus $E_{\mathrm{T}}^{\mathrm{miss}}$, (b) projection of significance versus H_{T} when no $E_{\mathrm{T}}^{\mathrm{miss}}$ cut is applied. 62

7.1 Examples of Feynman diagrams for Z-boson production and decay. . . . 70

7.2 Diagram of $E_{\mathrm{T}}^{\mathrm{miss}}$ versus dilepton invariant mass (m_{ll}) with labelled areas for Drell-Yan data-driven background estimates using the "ABCD" method. Regions A and C are the signal region, dominated by $t\bar{t}$ with ≥ 2 jets. 71

7.3 Diagram of $E_{\mathrm{T}}^{\mathrm{miss}}$ versus dilepton invariant mass (m_{ll}) for Drell-Yan data-driven background estimates using a simplified version of the "ABCD" method. Regions SR_1 and SR_2 are the signal regions, dominated by $t\bar{t}$ with ≥ 2 jets. 72

7.4 Reconstruction efficiency for loose electrons [153]. 77

7.5 Reconstruction efficiency for loose muons [153]. 77

7.6 Examples of Feynman diagrams for WW pair production. ZZ and WZ pairs can be produced similarly. 79

8.1 Top row $E_{\mathrm{T}}^{\mathrm{miss}}$ in events with a dilepton mass inside the Z mass window, middle row the number of jets in events with a dilepton mass inside the Z mass window and $E_{\mathrm{T}}^{\mathrm{miss}} < 40\mathrm{GeV}$, bottom row the invariant mass in events with $E_{\mathrm{T}}^{\mathrm{miss}} < 40\mathrm{GeV}$. Contributions from diboson and single top events are summarized as "other EW". The uncertainty on the data points are statistical uncertainties only, whereas the uncertainty bands include statistical and systematic uncertainties. 83

8.2 Invariant mass of same-sign $e\mu$ pairs and jet multiplicity distribution. Contributions from diboson and single top events are summarized as "other EW". The uncertainty on the data points are statistical uncertainties only, whereas the uncertainty bands include statistical and systematic uncertainties. 84

8.3 Invariant mass of same-sign ee and $\mu\mu$ pairs and jet multiplicity distribution. Contributions from diboson and single top events are summarized as "other EW". The uncertainty on the data points are statistical uncertainties only, whereas the uncertainty bands include statistical and systematic uncertainties. 84

8.4 Data and backgrounds in the $e\mu$ channel with exactly zero reconstructed jets, where $Z \to \tau\tau$ is the largest expected source. Contributions from diboson and single top events are summarized as "other EW". The uncertainty on the data points are statistical uncertainties only, whereas the uncertainty bands include statistical and systematic uncertainties. . . . 85

8.5 Jet multiplicities for the signal region omitting the $N_{\text{jets}} \geq 2$ requirement in (a) the ee channel, (b) the $\mu\mu$ channel and (c) the $e\mu$ channel. Contributions from diboson and single top events are summarized as "other EW". The uncertainty on the data points are statistical uncertainties only, whereas the uncertainty bands include statistical and systematic uncertainties. 87

8.6 b-tagged jet multiplicities for the signal region in (a) the ee channel, (b) the $\mu\mu$ channel and (c) the $e\mu$ channel. Contributions from diboson and single top events are summarized as "other EW". The uncertainty on the data points are statistical uncertainties only, whereas the uncertainty bands include statistical and systematic uncertainties. 87

8.7 (a) Jet multiplicity in the signal region without the $N_{\text{jets}} \geq 2$ requirement and (b) the b-tagged jet multiplicity in the signal region, both for the combined dilepton channels. Contributions from diboson and single top events are summarized as "other EW". The uncertainty on the data points are statistical uncertainties only, whereas the uncertainty bands include statistical and systematic uncertainties. 88

8.8 The $E_{\text{T}}^{\text{miss}}$ distribution in the signal region for (a) the ee channel and for (b) the $\mu\mu$ channel without the $E_{\text{T}}^{\text{miss}} > 40\text{GeV}$ requirement, and (c) the distribution of the H_{T}, defined as the scalar sum of the transverse energies of the two leptons and all selected jets, in the signal region without the $H_{\text{T}} > 130\text{GeV}$ requirement. Contributions from diboson and single top events are summarized as "other EW". The uncertainty on the data points are statistical uncertainties only, whereas the uncertainty bands include statistical and systematic uncertainties. 88

8.9 The m_{T2} distributions for events that pass the selection criteria for selected data events in the three dilepton channels overlayed over the expected distribution from MC simulation from signal and background events. Contributions from diboson and single top events are summarized as "other EW". The uncertainty on the data points are statistical uncertainties only, whereas the uncertainty bands include statistical and systematic uncertainties. 90

9.1 Number of reconstructed vertices with more than 4 tracks and selected as primary or pile-up vertices in the ee channel (left) and the $\mu\mu$ channel (right) in the Z-boson enhanced region [154]. 92
9.2 $E_{\mathrm{T}}^{\mathrm{miss}}$distribution for $Z \to ee$ enhanced events and 0-jets before (left) and after (right) reweighting [154]. 93
9.3 $E_{\mathrm{T}}^{\mathrm{miss}}$distribution for $Z \to ee$ enhanced events with 2 or more jets before (left) and after (right) reweighting in the ee channel [154]. 93

10.1 Plots of $-\log\lambda(\sigma_{t\bar{t}})$ vs. $\sigma_{t\bar{t}}/\sigma_{\mathrm{SM}}$ with (blue, solid) and without (red, dashed) systematics for the ee (top, left), $\mu\mu$ (top, right), $e\mu$ (bottom, left), and three-channel combined fit (bottom, right). The horizontal lines indicate likelihood values for the 68%, 90% and 95% confidence intervals, respectively. 109

11.1 The $\sigma_{t\bar{t}}$ cross section measurements from different methods. The yellow bar reflects the uncertainty on the theoretical prediction, which includes some of the NNLO corrections supplemented by soft gluon resummation at the next-to-next-to-leading-logarithm accuracy. 113

12.1 Top quark pair-production cross-section at hadron colliders as measured by CDF and D0 at Tevatron, CMS and ATLAS. The theoretical predictions for pp and $p\bar{p}$ collisions include the scale and PDF uncertainties, obtained using the HATHOR tool with the CTEQ6.6 PDFs and assume a top-quark mass of 172.5 GeV. 116

List of Tables

2.1 Overview of elementary particles in the SM with some of their properties and corresponding interactions to which they participate. Leptons and quarks are arranged in three generations. Bosons are the interaction mediating particles for three fundamental forces (gravitation is not included). In parentheses the years of discoveries are given. For gluon the theoretical value is given (a mass as large as a few MeV may not be precluded) [4]. . 4
2.2 W-boson decay modes. 13
2.3 Expected single top quark production cross sections in different channels at a center-of-mass energy of 7 TeV [32, 33, 34]. 15

3.1 Parameters of the four sub-systems of the muon detector. The quoted spatial resolution (columns 3, 4) does not include chamber-alignment uncertainties. 27

4.1 2010 data taking periods with corresponding run numbers and luminosities [67]. 33
4.2 Parameter variations in PYTHIA used for ISR and FSR samples. 36
4.3 $t\bar{t}$ samples which do not include all hadronic decays (No a.h.d.). The 105200 sample is used for the nominal analysis, the others are used for systematic evaluation. 37
4.4 Single top samples. 37
4.5 Z/γ^*+jets (Drell-Yan) samples with phase space cuts 10GeV $< m_{ll} <$ 40GeV(left) and $m_{ll} >$ 40GeV(right). 38
4.6 Diboson samples. 38

5.1 Definition of variables used for *loose*, *medium* and *tight* electron identification cuts for the central region of the detector with $|\eta| < 2.47$ [101]. . . 41
5.2 The measured constant term of the electron energy resolution. 43
5.3 Resolution parameterization as defined in Equation (5.3)-(5.5) in the MS and ID. The measurements are obtained by adding the correction parameters in quadrature to the uncorrected momentum resolution from simulation [119]. 48
5.4 Muon trigger scale factors from $Z \to \mu\mu$ data and MC events, using the tag-and-probe method. The results correspond to an integrated luminosity of 37 pb^{-1} [102]. 50

5.5 Offline scale factors, using the tag-and-probe method. The results correspond to an integrated luminosity of 37 pb^{-1}. The uncertainties are statistical and systematic [102]. 50

6.1 Trigger used for the different data periods and their luminosities, for MC EF_mu13_tight and EF_e15_medium were used. 60

6.2 List of cuts that is used for the Table 6.3, Table 6.4 and Table 6.4. e and μ overlap cut is not included in the tables, since its efficiency is 100% for most of the cases. 64

6.3 Cut flow table with number of selected events and relative efficiencies for ee channel selection for an integrated luminosity of 35 pb^{-1}. The relative efficiency ε, the ratio of the number of events passing a cut to the number of events before the cut, is also shown. The "MC truth" cut is applied only for the $t\bar{t}$ sample, it checks the existence of two truth leptons originating from t- and $\bar{t}$-quarks in the event. 65

6.4 Cut flow table with number of selected events and relative efficiencies for $\mu\mu$ channel selection for an integrated luminosity of 35 pb^{-1}. The relative efficiency ε, the ratio of the number of events passing a cut to the number of events before the cut, is also shown. The "MC truth" cut is applied only for the $t\bar{t}$ sample, it checks the existence of two truth leptons originating from t- and $\bar{t}$-quarks in the event. 66

6.5 Cut flow table with number of selected events and relative efficiencies for $e\mu$ channel selection for an integrated luminosity of 35 pb^{-1}. The relative efficiency ε, the ratio of the number of events passing a cut to the number of events before the cut, is also shown. The "MC truth" cut is applied only for the $t\bar{t}$ sample, it checks the existence of two truth leptons originating from t- and $\bar{t}$-quarks in the event. 67

7.1 Number of observed events in data in the control region (data(CR)), the number of MC events in the signal (MC(R)) and control (MC(CR)) regions and the number of events from other sources contaminating the control region. 73

7.2 Estimates of the contamination from Drell-Yan processes in the signal region of the $t\bar{t}$ analysis from both the data-driven (DD) method and from MC simulations. 73

7.3 Uncertainties on the predicted number of Drell-Yan events in the signal region. The uncertainties are compared between the data-driven (DD) determination and the determination from MC simulations. The uncertainty due to the method is evaluated from the variation of the prediction when the $E_{\mathrm{T}}^{\mathrm{miss}}$ cut in the control region is varied by $\pm$5GeV. The uncertainties of the prediction are presented as $+1\sigma/-1\sigma$ variation of the systematic source. 74

7.4 Overview of the estimated fake lepton background yields in the signal ($N_{\text{jets}} \geq 2$) and control regions using the matrix method for each sub-channel. Statistical and systematic uncertainties are shown as well. . . . 78

8.1 The full breakdown of the expected $t\bar{t}$-signal and background in the signal region compared to the observed event yields, for each of the dilepton channels (MC is simulation based, DD is data-driven). All systematic uncertainties are included and the correlation between the different background sources are taken into account. 86
8.2 The full breakdown of the expected $t\bar{t}$-signal and background in the signal region compared to the observed event yields, for each of the dilepton channels (MC is simulation based, DD is data-driven). All systematic uncertainties are included and the correlation between the different background sources are taken into account. 89

9.1 Uncertainties on the background estimation, acceptance and cross section in the ee channel. The uncertainties are presented as $+1\sigma/-1\sigma$ variation of the systematic source. 98
9.2 Uncertainties on the MC background contributions in the ee channel. The uncertainties are presented as $+1\sigma/-1\sigma$ variation of the systematic source. 99
9.3 Uncertainties on the background estimation, acceptance and cross section in the $\mu\mu$ channel. The uncertainties are presented as $+1\sigma/-1\sigma$ variation of the systematic source. 100
9.4 Uncertainties on the MC background contributions in the $\mu\mu$ channel. The uncertainties are presented as $+1\sigma/-1\sigma$ variation of the systematic source. 101
9.5 Uncertainties on the background estimation, acceptance and cross section in the $e\mu$ channel. The uncertainties are presented as $+1\sigma/-1\sigma$ variation of the systematic source. 102
9.6 Uncertainties on the MC background contributions in the $e\mu$ channel. The uncertainties are presented as $+1\sigma/-1\sigma$ variation of the systematic source. 103

10.1 Measured cross sections in each individual dilepton channel, and all three channels combined. The uncertainties are obtained from the likelihood minimization. 107
10.2 Overview of the $t\bar{t}$ cross section uncertainties for each channel and each systematic variation obtained from the combination. 108

A.1 The efficiency scale factors in different E_T and η_{clus} bins for electron identification $ElectronTight\_WithTrackMatch$. 117
A.2 Set of corrections to be applied to the p_T parameterization of the simulated resolution in the MS and ID to reproduce the one in data [119]. 118